Controlling molecular packing for charge transport in organic thin film devices

Simone Fabiano

Controlling molecular packing for charge transport in organic thin film devices

Simone Fabiano

PhD Thesis

Università degli studi di Palermo

UNIVERSITÀ DEGLI STUDI DI PALERMO
DIPARTIMENTO DI CHIMICA – S. CANNIZZARO
Dottorato in Scienze Chimiche

CONTROLLING MOLECULAR PACKING FOR CHARGE TRANSPORT IN ORGANIC THIN FILM DEVICES

Settore scientifico disciplinare CHIM/02

TESI DI
SIMONE FABIANO

TUTOR
PROF. BRUNO PIGNATARO

COORDINATORE DEL DOTTORATO
PROF. MICHELANGELO GRUTTADAURIA

XXIII CICLO – ANNI ACCADEMICI 2009/2011

Contents

1. Introduction **1**

1.1 Organic semiconductors 2

1.2 Charge transport in disordered organic systems 2

1.3 Device applications of organic materials 4

1.3.1 Organic field-effect transistors 4

1.3.2 Organic solar cells 8

1.4 Controlling the molecular packing at nanoscale 12

1.5 Outline of the thesis 14

References 15

2. Charge transport in 2D confined polymeric systems **19**

2.1 Introduction 20

2.2 Results and discussion 21

2.3 Conclusions 30

2.4 Experimental details 30

References 33

3. Effect of thermal stimuli on the supramolecular order **37**

3.1 Introduction 38

3.2 Results and discussion 39

3.3 Conclusions 50

3.4 Experimental details 51

References 53

4. Role of layer morphology in photoactive polymeric blends 57
4.1 Introduction 58
4.2 Results and discussion 59
4.3 Conclusions 67
4.4 Experimental details 67
References 70

5. Engineering 3D ordered polymeric films by composition optimization 73
5.1 Introduction 74
5.2 Results and discussion 75
5.3 Conclusions 81
5.4 Experimental details 82
References 84

Appendix A 87
Appendix B 97

Summary
Sommario

List of publications
Acknowledgements

Chapter 1
Introduction

In this chapter we present a brief overview regarding the field of organic semiconductors and we describe the operation principles of two (opto)electronic devices comprising semiconducting (macro) molecule films as the active component, namely field-effect transistors and solar cells. The effect of molecular and supramolecular order on the charge transport properties of organic thin films in the two and three dimensions is highlighted. Finally, a short outline of the thesis is given.

1.1 Organic semiconductors

Electrical conduction in organic materials has been reported for the first time in the 1950's and early 1960's, when photoconductivity and electroluminescence were detected in organic crystals, such as naphtalene and anthracene.[1] The discovery of conducting polymers and the work done to increase their conductivity in the late 1970's, however, offered the possibility to revolutionize electronics as these materials could be processed from solution.[2] This led to the Nobel Prize in Chemistry in 2000 for Heeger, MacDiarmid and Shirakawa. Since then, new perspectives have been opened on the applicability of organic semiconductors into solution-processed (opto)electronic devices, being able to provide large-scale and flexible applications at low cost and energy consumption, for which conventional inorganic semiconductors are too expensive or brittle.

Beside research in the field of polymer light-emitting diodes (LEDs),[3] several other research fields based on organic semiconductors have been developed in the past decades, such as field-effect transistors (FETs)[4,5] and solar cells (SCs).[6] In this respect, studies performed on organic systems have focused on explaining the charge transport within these materials, and much work has been done toward improving device performance. Since the organic materials are inherently different form their inorganic counterparts, it is not appropriate to simply transfer general understanding from the well-established field of inorganic semiconductors to the field of organic semiconductors. These differences lead to unique properties and the potential for novel applications.

1.2 Charge transport in disordered organic systems

Organic semiconductors are carbon-based materials having a framework of alternating single and double carbon-carbon bonds. The conjugated nature of the system leads to the semiconducting properties of these materials. Single bonds are referred to as σ-bonds and are associated with a highly localized electron density in the plane of the molecule, and double bonds contain a σ-bond and a π-bond, where the π-bond is the overlap between p_z orbitals of neighboring atoms along the conjugation path (Figure 1.1). The conjugation of single and double bonds establishes a delocalization of the electrons situated above and below the plane of the molecule.[7]

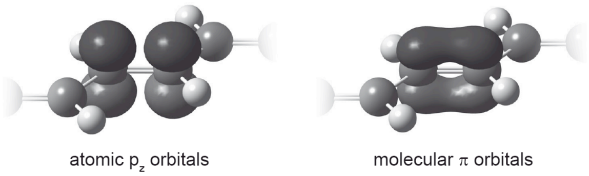

Figure 1.1. Schematic representation of the formation of molecular π-orbitals in polyacetylene from parallel-aligned atomic p_z-orbitals.

The system may be expected to behave as a one-dimensional metal, however, symmetry breaking reduces the energy of the system (Peierls instability), resulting in two delocalized energy bands, the bonding and anti-bonding π and π* orbitals, respectively. The bonding π-orbital is of lower energy and is called the highest occupied molecular orbital (HOMO) and the anti-bonding π*-orbital is called the lowest unoccupied molecular orbital (LUMO). The band gap of these materials determined from optical measurements is within the range of 1–4 eV, which covers the whole range from infrared to ultraviolet region. The value of the energy gap depends on the structure of the material, and decreases for an increasing number of repeat units comprising the molecules.[8] The rather large energy gap makes organic materials insulator by nature, consequently the intrinsic carrier concentration is very low. A single charge on a molecule causes a structural relaxation by electron-phonon coupling, and is then called polaron. This relaxation leads to two additional localized energy levels within the gap. In order to increase the carrier density, as required for many device applications, different mechanisms such as carrier injection or field effect, photocurrent generation, or doping can be applied.

Typically, conjugated segments along a polymer backbone are limited to a length of a few of nanometers (around 5 nm), separated by chemical or structural defects such as nonconjugated sp^3-hybridized carbon atoms on the polymer backbone, or chain kinks or twists out of coplanarity.[9] These conjugated segments vary in size and, consequently, each conjugated part of the molecule has a different local HOMO and LUMO energy. The variations in these energies create localized states on the polymer backbone. Structural disorder therefore leads to energetic disorder. The energy levels of the organic semiconductor cannot be described by two delocalized energy bands separated by an energy gap. The charge carriers are strongly localized on molecules or molecular segments, and the energy bands are broadened.[10] Due to the corresponding lack of extended (delocalized) states in amorphous organic materials, charge transport is governed by carrier hopping in a density of localized states (DOS).[11] The shape of the DOS is usually approximated by a Gaussian[12] or an exponential distribution.[13] The hopping transport results in rather low charge carrier mobilities that are electric field dependent and

thermally activated. The solution processing of organic semiconductors can lead to higher disorder in the thin film and therefore to lower mobilities compared with other deposition technique such as vacuum deposition. The DOS of these disordered systems is often asymmetrical and presents a significantly larger barrier to the formation of one or another type of carrier. Many amorphous or polycrystalline organic semiconductors sustain either positive or negative charge carriers, but not both. In conventional, inorganic semiconductor technologies, *n*-type and *p*-type refer to the type of dopant, and therefore majority carrier present in the semiconductor. In crystalline materials both holes and electrons can usually be transported reasonably well. Disordered electronic systems, on the other hand, often only support or strongly favor one type of charge carrier and are more properly referred to as hole or electron transporting. It is, nevertheless, common in the literature to refer to hole transporting disordered semiconductor materials as *p*-type and electron transporting materials as *n*-type because this describes their majority carriers and semiconducting behavior.

1.3 Device applications of organic materials

In this thesis we describe the effects of molecular and supramolecular order on the charge transport properties of semiconducting (macro)molecule films, both in-plane (e.g. FETs) and out-of-plane (e.g. SCs).

1.3.1 Organic field-effect transistors

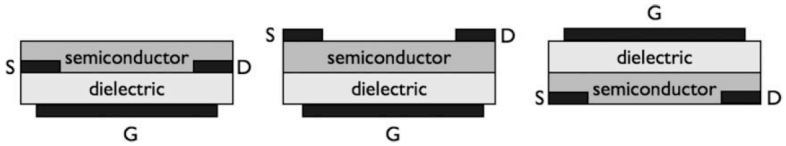

Figure 1.2. Three typical organic-transistor geometries. From left to right: bottom gate, bottom contacts (BG-BC); bottom gate, top contacts (BG-TC); top gate, bottom contacts (TG-BC). S: source; D: drain; G: gate.[14]

Organic field-effect transistors offer a straighforward method to investigate the charge transport properties of organic semiconductors.[14,15] A FET is a three-terminal device, containing a source, a drain and a gate electrode. The gate electrode is electrically separated from the source and drain electrode by the gate dielectric. In between the source and drain electrode an organic semiconductor is placed. A bias applied to the gate causes charge accumulation in the semiconductor. The accumulated charge decreases the resistance of the semiconductor.[16] Three variations, the bottom-gate/bottom-contacts (BG-BC), the bottom-gate/

top-contatcs (BG-TC) and top-gate/bottom-contatcs (TG-BC) structures are presented in Figure 1.2. For material characterization, the bottom-gate/bottom-contact architecture is more pratical from the point of view of device processing than the bottom-gate/top-contact structure, as the contacts can be deposited or patterned directly onto the substrate, and the semiconducting layer is placed as the final step. The risk of damaging the sensitive material during contact deposition is reduced. However, for integrated circuits the bottom-gate structure is unsuitable and, additionally, it results in higher electrical losses. On the other hand, the top-gate configuration overcome the main issues of organic FETs such as contact resistance and air stability. In this thesis organic transistors are discussed operating in *n*-type accumulation mode. When a positive bias is applied to the gate electrode, V_g, electrons accumulate in between the source and drain electrode at the semiconductor-dielectric interface. The accumulation layer creates a conducting path between the source and drain electrodes and a current can flow. For a negative gate bias the semiconductor is depleted of unintentionally doped carriers and the transistor is switched off. A typical transfer curve, where the source-drain current is monitored while the gate bias is swept, is presented in Figure 1.3. The source-drain bias, V_{ds}, is fixed. The transfer curve clearly shows the transition from the on- to the off-state.

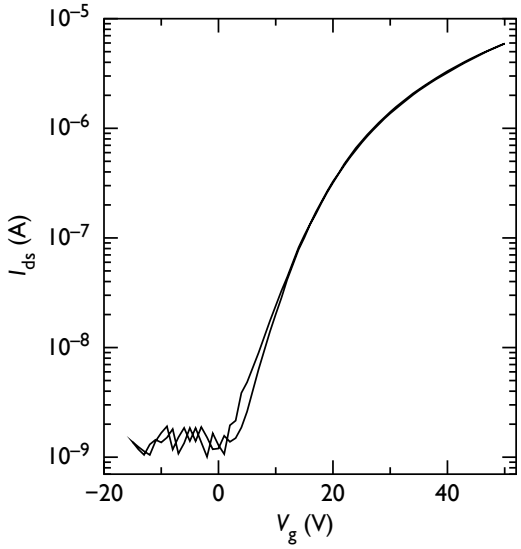

Figure 1.3. Typical transfer curve of a transistor comprising n-type semiconductor. At positive gate bias current flows, at negative gate bias the current is nearly zero.

When the bias on the drain is much smaller than the bias on the gate, the transistor is operated in the linear regime. When the drain bias is much larger than

the bias on the gate, the transistor is driven in saturation. In both regimes, an expression can be derived for the absolute value of the current analogous to classical inorganic metal-oxide-semiconductor modeling.[17] In the linear regime ($|V_{ds}| \ll |V_g - V_T|$) the source-drain current, I_{ds}, can be described by:

$$I_{ds} = -\mu_{lin} \frac{C_i W}{L} \left(V_g - V_T\right) V_{ds} \tag{1.1}$$

where W and L are the width and length of the transistor, respectively. C_i the oxide capacitance, μ_{lin} the mobility of the charge carriers in the linear regime and V_T the threshold voltage. In this way, a mobility of the charge carriers can be extracted from the current-voltage characteristics. It has to be noted that the mobility is not a material parameter but a device parameter.[18] The exact value is in general influenced by for instance the gate bias (charge density), trap states on the gate dielectric, the permittivity of the gate dielectric, chemical impurities, the type of contacts used and the device architecture. The usual way to deduce the mobility is to take the first derivative of the source-drain current to the gate bias, divide by the drain bias and correct for the geometrical parameters of the transistor:

$$\mu_{lin} = \frac{L}{V_{ds} C_i W} \frac{\partial I_{ds}}{\partial V_g} \tag{1.2}$$

In saturation, when $|V_{ds}| \geq |V_g - V_T|$, it can be derived that the source-drain current equals:

$$I_{ds} = -\mu_{sat} \frac{C_i W}{2L} \left(V_g - V_T\right)^2 \tag{1.3}$$

A value for the field effect mobility can then be obtained by taking the second derivative of the source-drain current to the gate bias and correct for the geometrical parameters of the transistor:

$$\mu_{sat} = \frac{L}{C_i W} \frac{\partial^2 I_{ds}}{\partial V_g^2} \tag{1.4}$$

The previous descriptions are suitable to extract key device parameters such as threshold voltage and mobility to compare different transistors. In addition, FET measurements have been found to be useful in gaining information about charge injection into organic semiconductors via analysis of the parasitic contact effects in these devices. The total device resistance R_{tot} is a sum of the resistance between the source and drain electrodes and the semiconductors R_{con} and the resistance of the semiconducting film across the channel R_{ch}, and is given by

$$R_{tot} = R_{ch} + R_{con} \tag{1.5}$$

In case the FET is contact limited ($R_{con} > R_{ch}$), the contact resistance has an impact on the device output. In fact the contact resistance manifests itself as a voltage drop in the drain and source contact regions. This results in an effective drop across the channel, leading to a lower current.

Much more work has been done on *p*-type than on *n*-type FETs. This is due to several factors: the lack of *n*-type behavior was attributed to traps in the material[19] or at the semiconductor-dielectric interface by the hydroxyl groups present in the commonly used gate oxides,[20] that hinder the electron transport. The few *n*-type materials available were found to be unsuitable for many applications due to instability, so that reports of ambipolar transport were absent from the literature till about ten years ago and most organic semiconductors were observed to behave as *p*-type materials. There are a few factors influencing the performance of FETs. The field effect mobility and conductivity of the materials influence the on/off behavior of the device: a high mobility and low conductivity result in higher on/off ratios.[21] Unintentional doping due to impurities leads to an increase in the conductivity, and a reduction in the on/off behavior. The field-effect mobilities in thin film are also limited by morphological factors. Impurities and grain bounda-ries behave as traps, and lead to reduced effective mobilities. For thin film FETs, the highest mobilities reported to date are for pentacene, one of the more widely studied organic semiconductors. Mobility in the order of 3 $cm^2 V^{-1}s^{-1}$ and on/off ratios of 10^5 have been reported for pentacene FETs using a polymer gate dielectric.[22] However, pentacene has a poor solubility and is therefore typically vacuum deposited. Recent efforts have focused on soluble precursor forms of pentacene which are applied directly to the substrate as a solution; the resulting film is then thermally treated or irradiated by UV light in order to convert the precursor to pentacene. The mobility values reported for the solution-prepared pentacene FETs are lower than those reported for vacuum-deposited pentacene, and of the order of 0.1-0.2 $cm^2 V^{-1}s^{-1}$.[23]

Furthermore, as already discussed, the conductive channel forms in the vicinity of the semiconductor-dielectric interface, thus the insulating material used influences the performances of the devices. The preparation and deposition techniques for the semiconductors and a surface treatment for the insulator can be decisive for reducing trapping effects. Traditionally, SiO_2 is used as gate dielectric for samples prepared on silicon substrates. However, the effort toward all-organic devices, has led to the use of appropriate hydroxyl-free insulating polymers for the gate insulator materials. These materials typically have lower dielectric constants when compared with inorganic materials resulting in high operating voltages, and thicker insulating layers are hence needed to avoid leakage currents which occur at the higher fields.

1.3.2 Organic solar cells

Although organic semiconductors have relatively low charge carrier mobilities, they have fairly strong absorption coefficients, exceeding 10^5 cm^{-1}, which leads to high absorption even for layers as thin as a hundred of nanometers.[24] This makes organic materials good candidates for replacing typical inorganic semiconductors in solar cells.

Power conversion efficiencies reported for organic solar cells have been steadly increased, as new suitable semiconducting materials are synthesized and investigated and device architectures improved. The first organic solar cell consisted of a single layer of evaporated organic molecules sandwiched between contacts, and the efficiencies reached 0.7%.[25] In polymer-based diodes the photovoltaic response was even smaller.[26] The problem here is that excitation of a polymer, for example by illumination, does not directly result in free charge carriers. Rather, a strongly bound exciton is created, with a binding energy of around 0.4 eV. Originating from a low dielectric constant, this energy is too large to permit dissociation of the exciton at typical electric field strengths in these devices. Therefore, excitons in single layers of a conjugated polymer tend to decay rather than dissociate at room temperature.[24] It has been demonstrated that the dissociation probability of photo-generated excitons can be enhanced considerably when an organic solar cell is divided in two layers of donor and acceptor materials that provide a suitable energetic offset at their interface.[27] Ultrafast charge transfer from the excited state across the heterojunction results in a spatially separated electron–hole (e–h) pair. Once the exciton is dissociated, the back-transfer process from the charge-separated state is much less efficient. A picosecond photoinduced electron transfer from a conjugated polymer onto buckminsterfullerene (C_{60}) has been reported.[28] Although the bilayer donor–acceptor (D–A) approach meant a major step forward for SCs, its success is limi-

ted by the ability of excitons to reach the interface before recombining. As conjugated polymers exhibit low exciton diffusion lengths on the order of 5–10 nm,[29] the photocurrent of a bilayer cell is fully determined by exciton generation close to the donor–acceptor interface. A breaktrough came with the discovery that, by combining donor and acceptor in a bulk heterojunction (BHJ) structure so as to maximize the interface between the two components results in much higher efficiencies.[30] In this approach, which forms the basis of solution-processed photovoltaics today, the photogenerated excitons thus have a much higher probability of reaching a donor–acceptor interface before recombining. Sufficient percolation yields an interpenetrating network of donor and acceptor, which is required for transport of charges to the electrodes. This implies that the performance of a BHJ solar cell depends heavily on the morphology of the donor–acceptor system.

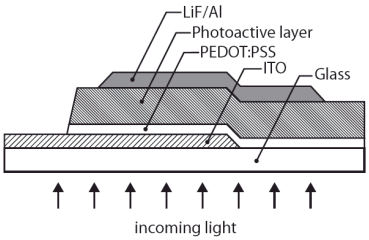

Figure 1.4. Cross-section of a polymer solar cell. The light is incident through the substrate.

The typical basic structure of a BHJ solar cell consists of a thin donor–acceptor blend layer between two electrodes with asymmetric work functions, as depicted in Figure 1.4. For practical reasons a glass substrate is often used in lab-scale devices, whereas for commercial applications plastic supports or metal sheets can be used to create flexible devices. The electrode between the substrate and the photoactive layer is made from a transparent conductive oxide, usually indium tin oxide (ITO), covered with a thin layer of poly(3,4-ethylenedioxythiophene): poly(styrenesulfonate) (PEDOT:PSS), a conductive polymer. With a work function of 5.2 eV, this electrode acts as a hole-extracting contact and is therefore denoted as anode. On the other side of the device, a low work function electrode composed of an ultrathin lithium fluoride layer capped with aluminum serves at least two purposes: it provides an electron-extracting contact (cathode) and it acts as a mirror to reflect the light back into the device. To improve the efficiencies of organic solar cells, more knowledge about the physics of these complex devices is needed. The efficiency of a solar cell is dipendent on the open-circuit voltage and the short-circuit current, which in turn are dependent on the energetics of the materials, the absorption and the morphology of the active layer, respectively.

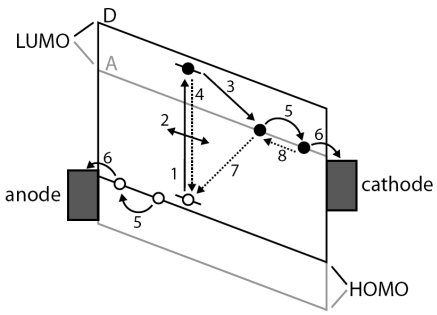

Figure 1.5. Schematic representation of photocurrent generation in a bulk heterojunction solar cell, operating close to short-circuit conditions. The indicated processes are (1) exciton generation, (2) exciton diffusion, (3) charge transfer, (4) exciton decay, (5) charge transport, (6) charge extraction, (7) (geminate) recombination of bound pairs, and (8) bimolecular recombination of free charges, which results in a bound e–h pair.

The transport properties of organic semiconductors are much different under illumination than in the dark.[31] A schematic representation of the photocurrent generation in a BHJ solar cell is depicted in Figure 1.5. As already discussed, the photoexcitation of organic materials (1) results in Coulombically bound electron-hole pairs with a rather high binding energy (excitons). This neutral and mobile excitons can be dissociated into charge carries only by strong fields, defect sites, or diffusing to the donor–acceptor interface (2). Here, they are separated by an ultrafast charge transfer of electrons to the acceptor (3). Alternatively, excitons decay to the ground state (4) losing the excitation energy, and no contribution to the photocurrent is made. When charge transfer does occur, the separated carriers are then transported to the electrodes (5) and extracted by an applied field before they recombine (6). However, bound pairs at the interface have a finite lifetime and can decay to the ground state via geminate recombination (7), in which case the carriers are lost. Bimolecular recombination of free carriers (8) gives a bound pair again, which can either redissociate or decay to the ground state. Ideally, the hole and electron mobilities within a polymer solar cell should be balanced. Different mobilities result in different mean free paths of the individual charge carriers, which can lead to an imbalanced distribution of charges within the semiconductor layer, whereby the slowest charges will determine the device performance.

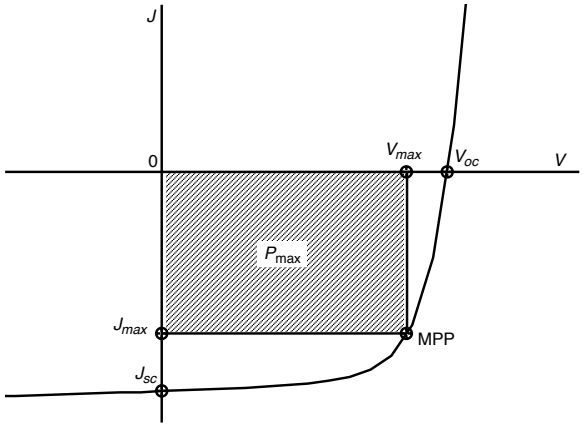

Figure 1.6. Typical *J-V* curve of an organic solar cell under illumination. The parameters determining the device efficiency are indicated in the figure and explained in the text.

The power conversion efficiency η of a solar cell is defined as the ratio of the maximum electrical power it can deliver (P_{max}) to the optical power of the incident light (P_{in}).[32] Although it allows a quantitative comparison of the performance of various solar cells, the maximum output power alone does not provide information on the underlying physical processes that govern cell performance. Instead, a current density–voltage (*J-V*) measurement must be conducted. A typical *J-V* curve is reported in Figure 1.6. The curve is characterized by several parameters: (1) the short-circuit current density J_{sc} defined as the current density at zero applied voltage, (2) the open-circuit voltage V_{oc} that is the applied voltage at which the current in the external circuit equals zero, (3) the maximum power point MPP defined as the point on the curve with maximum electrical power density, and (4) the fill factor *FF*, that is the ratio of P_{max} to $J_{sc} \cdot V_{oc}$. External work can only be done when the cell operates in the fourth quadrant, i.e. when $0 < V < V_{oc}$. The power conversion efficiency can now be expressed in terms of J_{sc}, V_{oc} and FF:

$$\eta = \frac{P_{max}}{P_{in}} = \frac{J_{sc} V_{oc} FF}{P_{in}} \qquad (1.6)$$

Thus, in order to improve the efficiency, the device parameters such as the open-circuit voltage, the short-circuit current and the fill factor have to be enhanced. More specifically, the understanding of the electrical losses at the metal contacts and semiconductor interface due to recombination or large extraction barrier, or within the bulk of the active layer, resulting in charge carrier trapping or recombination, are necessary to improve device efficiencies. The current is

determined by the width of the absorption spectrum of the organic absorber material, and by the morphology of the active layer. Poor morphology limits the charge carrier transport through the film due to increased recombination.

Insight in the spectral dependence of photocurrent generation can be obtained by determining the external quantum efficiency (*EQE*), which measures the amount of electrons extracted to the external circuit per incident photon. The *EQE* or incident-photon-to-current conversion efficiency (*IPCE*) is related to the spectral responsivity $S(\lambda)$ according to

$$EQE(\lambda) = \frac{hc}{q\lambda} S(\lambda) \tag{1.7}$$

where h is Planck's constant, c is the speed of light and q is the elementary charge.

1.4 Controlling molecular packing at nanoscale

The (opto)electronic properties of organic semiconductors are greatly dependent on the packing modes of these materials, that is the molecular arrangement and morphology in organic thin films. Understanding and controlling the growth of organic semiconductor thin films to obtain a proper micro- and nanostructure is significant for optimizing the device performance. Due to their different operation principles, organic devices have different requirements for the packing modes of organic semiconductor films. For example, in organic FETs charges travel within the first few nanometers of the organic semiconductor in contact with the dielectric layer, thus charge transport is extraordinarily sensitive to the bi-dimensional molecular organization at such an interface. Crystalline and continuous films with a preferential edge-on molecular orientation have been demonstrated to form optimal 2D conductive channels with respect to the substrate.[5] On the other hand, a precise control of the molecular organization in the three dimensions is of fundamental interest for diode architectures where charge transport is perpendicular to the electrodes. In case of organic SCs based on a donor/acceptor bulk heterojunction, it is highly desired to have a fine phase separation between the donor and the acceptor material, which increases the heterojunction interface and forms optimal vertical conductive channels with respect to the substrate, in order to obtain an appropriate charge-transport mobility and a high energy-conversion efficiency.[30] In addition, charge generation depends not only on the donor and acceptor material state energies, but also on the specific molecular environment at the donor/acceptor interface. Indeed, it has been demonstrated that by increasing the steric

bulk at such an interface likely decreases the Coulomb binding strength exerted on the geminate pair and facilitates photocurrent generation.[33] In this context, engineering solid supported 2D and 3D supramolecular and molecular superstructures is of particular interest.

One of the greatest challenges in designing new materials is the dependence of the charge transport properties on the processing conditions. For instance, carrier mobility can vary by several orders of magnitude in films of nominally the same materials by controlling the surface energy of the substrate or by thermal or solvent annealing.[34] Different strategies can lead to well-ordered nanopatterning. On this respect, two bottom-up approaches, i.e. self-assembly (thermodynamically-driven process) and self-organization (kinetically-driven process), are very attractive for controlling the molecular packing in such large scale and low-cost devices. The former is in fact governed by the spontaneous association of molecules under energy minimization conditions into stable, structurally well-defined supramolecular architectures joined by non-covalent bonds.[35] Therefore, such engineering processes of molecular nanostructures at the surfaces should take account of critical parameters like the lateral interactions of molecules and their coupling to the surface in order to guide the assembly towards the desired structure.[36]

On the other hand, self-organization exploits spatio-temporal dynamic conditions to get ordered super-structures on the nanoscale. This has been explained as a result of the action of competitive forces.[37] To get order in an out-of-equilibrium condition is of course of great stimulus since, due to the wide number of possible pathways, it may allow for the generation of a much larger spectrum of ordered systems with respect to those obtainable by free energy minima. Indeed, contrary to self-assembly, the structural features of these patterns are induced by instability effects that may vary significantly with kinetic factors (dissipative structures) like evaporation rate, transfer speed and importantly by the sequence of operations of the experimental protocol. Furthermore, spatio-temporal dynamics of the out-of-equilibrium structures deal of course with deposition techniques that are routinely used for applications, like spin-coating. There, the rapid solvent evaporation may produce local fluctuations of composition. Such fluctuations may in turn determine a film instability and their wavelength would guide the final morphology of the segregated structures (vertical and/or lateral).[38] Developing a complete understanding of the processes occurring during the spin coating of multiphase polymeric materials from a common solvent is crucial for the realization of functional morphologies for polymer-based devices.

1.5 Outline of the thesis

Based on these concepts, here we focus on controlling the molecular packing of solution-processed organic thin films at nanoscale, for systems ordered on the two and three dimensions. In *Chapter 2*, the charge transport properties of confined polymeric systems in a 2D space is discussed. Monolayer field-effect transistors based on a high-mobility *n*-type polymer are demonstrated by an accurate control of the long-range molecular and supramolecular order, which yields dense polymer packing. Layer-by-layer film transistors of increasing thickness are fabricated and their performance compared to those of spin-coated films, revealing new insights into the charge transport properties of organic semiconductors.

The effects of external stimuli, such as thermal annealing, on the supramolecular order of solution-processed semiconducting molecules are reported in *Chapter 3*. The exceptional molecular orientation regardless of the substrate chemistry is rationalized in terms of strong intermolecular interactions. The remarkable 2D charge carrier mobility measured in field effect transistors underlines the importance of strong intermolecular interactions for the realization of high performing devices.

Chapter 4 describes the effect of layer morphology on the photoactive properties of a polymeric blend. The all-polymer thin films are engineered by nanoscale control, from a vertical phase segregation (2D order) to a lateral phase separation (3D order). The results suggest high dissociation efficiency for the bounded electron-hole pairs and balanced electron and hole mobility along the thin films, revealing new insights into the main factors limiting the efficiency of all-polymer solar cells. Finally, the morphology of a photoactive polymeric blend is modulated by polymer composition ratio optimization to give a high percentage of domains comparable with the exciton diffusion length, and the results discussed in *Chapter 5*.

References

[1] H. Mette, *Z. Physik* **1953**, *134*, 566; R. G. Kepler, *Phys. Rev.* **1960**, *119*, 1226; O. H. L. Blanc, *J. Chem. Phys.* **1960**, *33*, 626; M. Pope, H. P. Kallmann, P. Magnante, *J. Chem. Phys.* **1963**, *38*, 2042.

[2] C. K. Chiang, C. R. F. Jr., Y. W. Park, A. J. Heeger, H. Shirakawa, E. J. Louis, S. C. Gau, A. G. MacDiarmid, *Phys. Rev. Lett.* **1977**, *39*, 1098.

[3] J. H. Burroughes, D. D. C. Bradley, A. R. Brown, R. N. Marks, K. Mackay, R. H. Friend, P. L. Burns, A. B. Holmes, *Nature* **1990**, *347*, 539.

[4] H. Koezuka, A. Tsumura, Y. Ando, *Synth. Met.* **1987**, *18*, 699; A. R. Brown, A. Pomp, C. M. Hart, D. M. d. Leeuw, *Science* **1995**, *270*, 972.

[5] H. Sirringhaus, P. J. Brown, R. H. Friend, M. M. Nielsen, K. Bechgaard, B. M. W. Langeveld-Voss, A. J. H. Spiering, R. A. J. Janssen, E. W. Meijer, P. Herwig, D. M. d. Leeuw, *Nature* **1999**, *401*, 685.

[6] G. Yu, K. Pakbaz, A. J. Heeger, *Appl. Phys. Lett.* **1994**, *64*, 3422; S. E. Shaheen, C. J. Brabec, N. S. Sariciftci, *Appl. Phys. Lett.* **2001**, *78*, 841; P. Schilinsky, C. Waldauf, C. J. Brabec, *Appl. Phys. Lett.* **2002**, *81*, 3885.

[7] M. Pope, C. E. Swenberg, *Electronic Processes in Organic Crystals and Polymers*, 2nd ed., Oxford University Press, **1999**.

[8] C. W. Scherr, *J. Chem. Phys.* **1953**, *21*, 1582.

[9] F. Schindler, J. Jacob, A. Grimsdale, U. Scherf, K. Mullen, J. M. Lupton, J. Feldmann, *Angew. Chem. Int. Ed.* **2005**, *44*, 1520.

[10] E. Meijer, PhD Thesis, Delft University **2003**.

[11] B. Shklovskii, A. Efros, *Electronic properties of doped semiconductors*, Springer-Verlag, Berlin, **1984**.

[12] W. F. Pasveer, J. Cottaar, C. Tanase, R. Coehoorn, P. A. Bobbert, P. W. M. Blom, D. M. de Leeuw, M. A. J. Michels, *Phys. Rev. Lett.* **2005**, *94*, 4.

[13] C. Tanase, E. J. Meijer, P. W. M. Blom, D. M. de Leeuw, *Phys. Rev. Lett.* **2003**, *91*, 4.

[14] D. Braga, G. Horowitz, *Adv. Mater.* **2009**, *21*, 1473.

[15] G. Horowitz, *Adv. Mater.* **1998**, *10*, 365.

[16] P. Stallinga, V. A. L. Roy, Z.-X. Xu, H.-F. Xiang, C.-M. Che, *Adv. Mater.* **2008**, *20*, 2120.

[17] S. Sze, *Physics of Semiconductor Devices*, 2nd ed. ed., Wiley, New York, **2002**.

[18] C. Reese, Z. Bao, *Adv. Funct. Mater.* **2009**, *19*, 763.

[19] H. Antoniadis, M. A. Abkowitz, B. R. Hsieh, *Appl. Phys. Lett.* **1994**, *65*, 2030.
[20] L. L. Chua, J. Zaumseil, J. F. Chang, E. C. W. Ou, P. K. H. Ho, H. Sirringhaus, R. H. Friend, *Nature* **2005**, *434*, 194.
[21] T. D. Anthopoulos, C. Tanase, S. Setayesh, E. J. Meijer, J. C. Hummelen, P. W. M. Blom, D. M. de Leeuw, *Adv. Mater.* **2004**, *16*, 2174.
[22] H. Klauk, M. Halik, U. Zschieschang, G. Schmid, W. Radlik, W. Weber, *J. Appl. Phys.* **2002**, *92*, 5259.
[23] P. T. Herwig, K. Mullen, *Adv. Mater.* **1999**, *11*, 480; A. Afzali, C. D. Dimitrakopoulos, T. L. Breen, *J. Am. Chem. Soc.* **2002**, *124*, 8812.
[24] K. M. Coakley, M. D. McGehee, *Chem. Mater.* **2004**, *16*, 4533.
[25] D. L. Morel, A. K. Ghosh, T. Feng, E. L. Stogryn, P. E. Purwin, R. F. Shaw, C. Fishman, *Appl. Phys. Lett.* **1978**, *32*, 495.
[26] G. Horowitz, *Adv. Mater.* **1990**, *2*, 287.
[27] C. W. Tang, *Appl. Phys. Lett.* **1986**, *48*, 183.
[28] N. S. Sariciftci, L. Smilowitz, A. J. Heeger, F. Wudl, *Science* **1992**, *258*, 1474.
[29] D. E. Markov, E. Amsterdam, P. W. M. Blom, A. B. Sieval, J. C. Hummelen, *J. Phys. Chem. A* **2005**, *109*, 5266; O. V. Mikhnenko, F. Cordella, A. B. Sieval, J. C. Hummelen, P. W. M. Blom, M. A. Loi, *J. Phys. Chem. B* **2008**, *112*, 11601.
[30] G. Yu, J. Gao, J. C. Hummelen, F. Wudl, A. J. Heeger, *Science* **1995**, *270*, 1789.
[31] P. W. M. Blom, V. D. Mihailetchi, L. J. A. Koster, D. E. Markov, *Adv. Mater.* **2007**, *19*, 1551.
[32] D. J. D. Moet, PhD Thesis, University of Groningen **2011**.
[33] T. W. Holcombe, J. E. Norton, J. Rivnay, C. H. Woo, L. Goris, C. Piliego, G. Griffini, A. Sellinger, J. L. Bredas, A. Salleo, J. M. J. Frechet, *J. Am. Chem. Soc.* **2011**, *133*, 12106.
[34] I. McCulloch, M. Heeney, C. Bailey, K. Genevicius, I. MacDonald, M. Shkunov, D. Sparrowe, S. Tierney, R. Wagner, W. Zhang, M. L. Chabinyc, R. J. Kline, M. D. McGehee, M. F. Toney, *Nature Mater.* **2006**, *5*, 328; M. L. Chabinyc, L. H. Jimison, J. Rivnay, A. Salleo, *Mrs Bulletin* **2008**, *33*, 683; R. J. Kline, M. D. McGehee, E. N. Kadnikova, J. S. Liu, J. M. J. Frechet, *Adv. Mater.* **2003**, *15*, 1519; I. McCulloch, M. Heeney, M. L. Chabinyc, D. DeLongchamp, R. J. Kline, M. Coelle, W. Duffy, D. Fischer, D. Gundlach, B. Hamadani, R. Hamilton, L. Richter, A. Salleo, M. Shkunov, D. Sporrowe, S. Tierney, W. Zhong, *Adv. Mater.* **2009**, *21*, 1091.
[35] G. M. Whitesides, J. P. Mathias, C. T. Seto, *Science* **1991**, *254*, 1312.
[36] J. V. Barth, G. Costantini, K. Kern, *Nature* **2005**, *437*, 671.

[37] S. Fabiano, B. Pignataro, *Phys. Chem. Chem. Phys.* **2010**, *12*, 14848.
[38] R. A. L. Jones, L. J. Norton, E. J. Kramer, F. S. Bates, P. Wiltzius, *Phys. Rev. Lett.* **1991**, *66*, 1326.

Chapter 2

Charge transport in 2D confined polymeric systems

In this chapter, we study the charge transport properties of confined polymeric systems in a two-dimensional space. Monolayer field-effect transistors based on a high-mobility n-type polymer are demonstrated by an accurate control of the long-range molecular and supramolecular order, which yields dense polymer packing. Layer-by-layer film transistors of increasing thickness are fabricated and their performance compared to those of spin-coated films, revealing new insights into the charge transport properties of organic semiconductors.

Published as:
S. Fabiano, C. Musumeci, Z. Chen, A. Scandurra, H. Wang, Y-L. Loo, A. Facchetti and B. Pignataro, *Adv. Mater.* 2012, **24**, 951.

2.1 Introduction

Semiconducting polymers are intensively investigated for applications in large-area electronics, including displays and printable complementary circuits.[1] Recent developments in materials design,[2] thin-film/crystal microstructure,[3] and device engineering have led to dramatic performance advances for both *p*- and *n*-channel polymeric field-effect transistors (FETs).[4] The integration of polymeric semiconductor films approaching a single molecular layer would be of technological interest for the realization of bottom-up electronic devices as well as for new fundamental studies. Nevertheless, unlike small molecules,[5] conjugated polymers have not been successfully downscaled into monolayer semiconductor channels, and this is a well recognized task.[6] Ultrathin regioregular poly(3-hexylthiophene) (P3HT) films with ordered lamellar structures have been integrated into FETs by the pioneering work of Sirringhaus et al..[7] Hole mobilities as high as 0.02 $cm^2\ V^{-1}\ s^{-1}$ have been measured for devices based on ten molecular layers, but only negligible in-plane mobility (10^{-5}–10^{-4} $cm^2\ V^{-1}\ s^{-1}$) was reported for monolayer P3HT FETs.[7,8] Polydiacetylenes have also been used to fabricate monolayer FETs, again, with performance being far from ideal.[9] Although, charge transport behaviors of small-molecule-based *n*-channel FETs as a function of active layer thickness were shown previously,[10] no examples have been reported to date for polymer-based *n*-channel monolayer semiconductors. Recent studies have shown that *n*-type semiconducting polymers exhibit very attractive charge transport properties,[11] with electron mobilities of ~0.2 $cm^2\ V^{-1}\ s^{-1}$ reported for the polymer poly{[*N*,*N*'-bis(2-octyldodecyl)-naphthalene-1,4,5,8-bis(di-carboximide)-2,6-diyl]-*alt*-5,5'-(2,2'-bithiophene)} (P(NDI2OD-T2)) in a top-gate FET architecture and using PMMA as gate dielectric.[4d] Owing to its large electron mobility, environmental stability and solution processability, P(NDI2OD-T2) has been extensively investigated revealing the unconventional face-on texture and exceptional in-plane order of this material pristine films.[12] This packing motif suggests a more likely three-dimensional charge transport which disagrees with the traditional two-dimensional character of charge carriers in high performance thin film transistors.[13] Furthermore, recent studies addressed detail of P(NDI2OD-T2) film microstructure, how it can be varied with thermal annealing, and how this affects FET performance.[14] However, fundamental questions remain about the nature of P(NDI2OD-T2) film microstructure in the very first few layers of the transistor channel.

Here we show monolayer field-effect transistors with unprecedented performance by employing P(NDI2OD-T2) with an edge-on orientation with respect to the dielectric surface. The accurate control of the long-range order by Langmuir-

Schäfer (LS) deposition yields dense polymer packing exhibiting good injection properties and saturation, relevant current on/off ratio and carrier mobility in a staggered FET configuration. Seemingly, layer-by-layer ordered LS thin film transistors of increasing film thickness were fabricated and their performance compared to those of the spin-coated films. The ability to control the orientations of the polymer backbone allows us to establish a direct correlation between the direction of the π-π stacking and the in-plane FET mobility, revealing new insights into the charge transport properties of this semiconductor.

2.2 Results and discussion

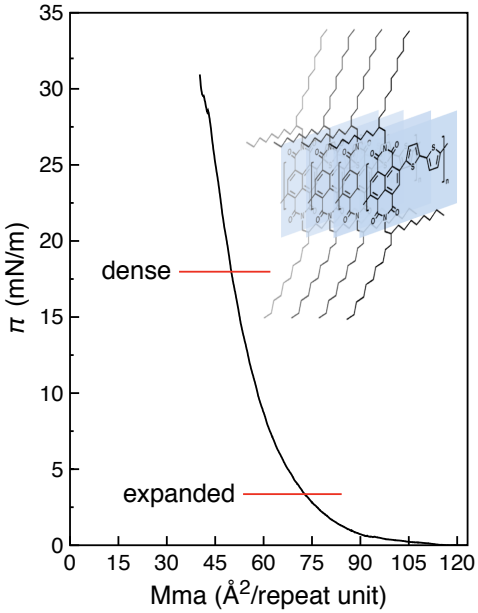

Figure 2.1. Surface pressure (π) vs. mean monomeric area isotherm of P(NDI2OD-T2) spread from 0.2 mg mL^{-1} $CHCl_3$ solution. The inset shows the chemical structure of P(NDI2OD-T2) and a schematic of the edge-on molecular packing inferred from the isotherm measurements for the individual monomeric units.

Ordered thin films were fabricated using the LS technique and details are reported in the Experimental Section. Langmuir deposition methods are known to enable the realization of monolayers at the air/liquid interface with precision control over the molecule lateral packing density.[15] The surface pressure (π) for P(NDI2OD-T2) spread from a dilute solution (0.2 mg mL^{-1}) onto the water subphase is presented in Figure 2.1 as a function of the mean monomeric area (Mma). The isotherm shows a gradual transition from an expanded state to a condensed state with abrupt slope. In

the condensed phase, the strong π-π interactions between the aromatic backbones and the van der Waals interactions between the branched octyl-decyl side chains promote the self-assembly in ordered close-packed films at the air/water interface upon compression, as schematized in the inset to Figure 2.1. The monolayer compressibility (0.02 m/mN), defined as $C_m = -1/A_0(\partial A/\partial \pi)$ with A_0 the limiting molecular area, is one order of magnitude smaller than that of regioregular P3HT (0.38 m/mN, Ref. [8]). Compression/expansion studies of the monolayer films disclose a plastic behavior of the P(NDI2OD-T2) monolayer. In Figure 2.2a the isotherm curve marked as (i) has been performed by compressing the P(NDI2OD-T2) monolayer up to the collapse point. After the barriers have been retracted to their zero position, a new isotherm (curve ii) was recorded by monitoring again the surface-pressure under the barrier compression in a second cycle. The hysteresis between curves (i) and (ii) together with the low compressibility of the film are ascribed to the high molecular sticking due to strong π-π interaction between the large aromatic moieties of the polymer chains along with the van der Waals interactions between the branched octyl-decyl side moieties. Accordingly, upon the first barrier expansion to their zero point, the film showed a plastic behavior and a squared self-standing close-packed film is observed in the central region of the LS trough. Under the second compression (curve ii), a higher compressibility along with a more drastic transition from the expanded to the condensed state is observed due to the presence of the already packed system. Moreover, note that a molecular loss occurs at about 42 mN/m (collapse point) in agreement with the multilayered structure observed by SFM images in LS films transferred at about 20 mN/m during the second compression (curve ii). As far as the compression/expansion cycle is performed by preventing the achievement of film collapse (target pressure 20 mN/m, Fig. 2.2b), the above film plastic behavior is still observed (large hysteresis, compact squared structure at the trough centre). Once we avoid molecular losses, the limiting molecular area evaluated by considering the compact layer of curve (ii) in Fig. 2.2b results of about 60 Å^2. This is in excellent agreement with the area per repeat unit (~55 Å^2) calculated by considering for P(NDI2OD-T2) a chain backbone repeat distance of 13.9 Å and a π-stacking separation of 3.93 Å, as observed from X-ray diffraction.[12] These findings reveal a Langmuir close-packed monolayer with out-of-plane molecular order.

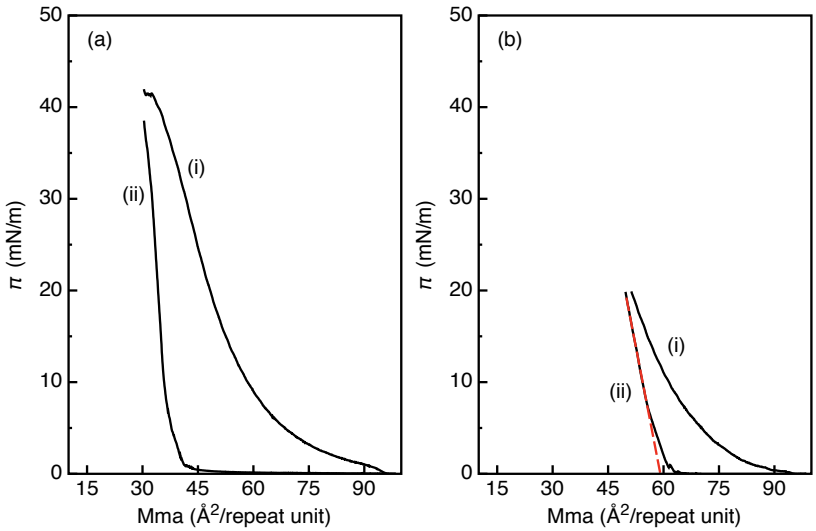

Figure 2.2. Repeated π-Mma curves of P(NDI2OD-T2) performed by compressing the monolayer to the following target pressures: (a) about 40 mN/m (collapse point); (b) 20 mN/m. Only the first (i) and the second (ii) compression isotherms are plotted. The limiting molecular area is extrapolated at zero pressure by the dashed red line of curve ii in (b).

Monolayer and multilayers of P(NDI2OD-T2) were successfully transferred on HMDS-treated silicon and glass substrates as well as Au. Unless indicated otherwise, all of the thin-film characterizations reported below were performed on the LS films after thermal annealing in a vacuum oven overnight to fully remove the water. In particular, the deposition was carried out at a surface pressure of about 20 mN m^{-1}, by approaching the substrate horizontally to the air/water interface. This surface pressure allows for the self-assembly of aligned films with predominantly edge-on molecular packing over large areas, as revealed by scanning force microscopy (SFM) measurements of P(NDI2OD-T2) films transferred to substrates. The SFM morphological analysis of P(NDI2OD-T2) monolayers on HMDS-modified silicon oxide is presented in Figure 2.3. For efficient charge transport within the semiconducting monolayer, long-range order is required. Remarkably, SFM measurements reveal a smooth continuous layer with a root mean square roughness (RMS) of about 0.5 nm and a thickness of 3.1 nm, as determined by the cross section analysis in defective regions of the film (Figure 2.3b). Such a molecular step closely resembles the calculated 3.2 nm long molecular axis size and it is consistent with an out-of-plane structural organization of both the naphthalene diimide cores and the branched alkyl side chains supposed to be roughly parallel to the substrate normal. Interestingly, the edge-on conformation is maintained in the successive LS transfers (see Figure 2.3d the step height of a second layer of about 3.0 nm and Appendix A Figure S3b), allowing for the development of multilayered thin films of P(NDI2OD-T2) with precise edge-on

conformation. Note that SFM measurements have been performed on defective regions of the thin films that we discovered occasionally outside of the channel. SFM images indicate that thermal annealing has minimal effects on the film morphology and surface roughness including the persistence of the squared holes (see Appendix A, Figure S1-S4), indicating that the edge-on order represents a minimum-energy conformation for this substrate/thin-film system. This is also corroborated by recent observations on the texture of P(NDI2OD-T2) thin films after melt annealing, revealing an increased crystallinity along with edge-on lamellar conformation upon energy minimization.[14] In general, the molecular orientation with respect to the substrate in the mono-/multilayer films critically depends on the relative strengths of the molecule-substrate versus intermolecular interactions. In the present case, the out-of-plane molecular order is reached at the air/water interface during compression and thereby transferred to the substrate. Note that here we show images on silicon oxide due to its very smooth surface (RMS ≈ 0.2 nm) allowing for precisely measuring the monolayer step, nevertheless a similar effect has been observed on other substrate surfaces, such as gold and glass, which are of interest for the fabrication of top-gate field-effect transistors (see Appendix A, Figure S3-S5).

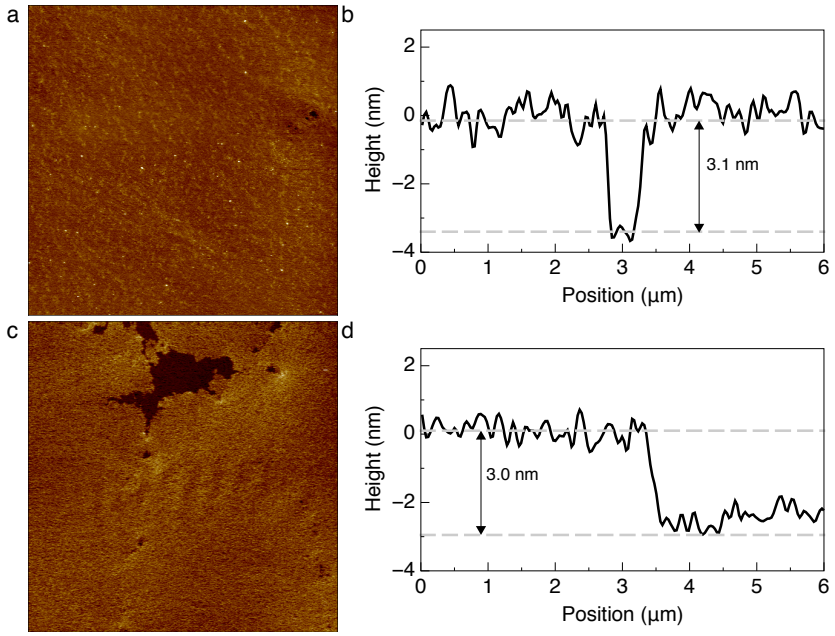

Figure 2.3. (a) Typical topography image (30 × 30 µm²) of the Langmuir-Schäfer monolayer measured by SFM. On the top right of the image a void defect is present. (b) A cross-section along the defect is depicted. The thickness of the single-layer is 3.1 nm. (c) Typical topography image (30 × 30 µm²) of the LS P(NDI2OD-T2) bilayer measured by SFM. (d) The long-range order is maintained in the second layer along with the edge-on order as indicated by a step height of 3.0 nm.

Near-edge X-ray absorption fine structure spectroscopy (NEXAFS) conducted on LS monolayers deposited and thermally annealed on HMDS-modified glass further corroborates this edge-on preferential orientation (see Figure 2.4a). The pre- and post-edge normalized spectra obtained at the carbon edge reveal intensity anisotropy with incident angles; quantitative analysis of this intensity anisotropy reveals a dichroic ratio (DR) of 0.23. The DR measures the extent of preferential orientation (see Appendix A for further discussion). By definition, DR = 1 indicates that the π-planes in the area of illumination (1 × 1 mm^2) are all preferentially oriented upright. In contrast, DR = -1 indicates that the π-planes are all preferentially oriented face-on and DR = 0 indicates no preferential orientation. For reference, while our measured DR of 0.23 is lower than those of small molecules[16] and self-assembled monolayers,[17] this extent of orientation is comparable to that observed in edge-on oriented polythiophenes thin films.[18]

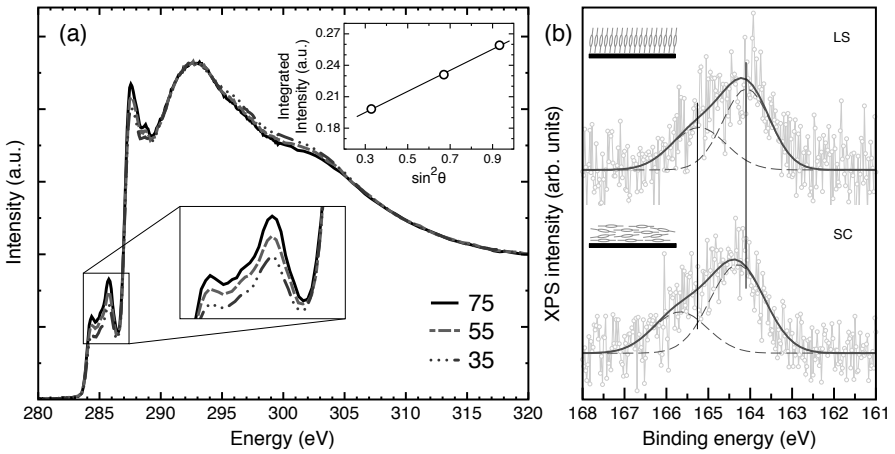

Figure 2.4. (a) Pre- and post-edge normalized NEXAFS spectra at the carbon edge at different X-ray incident angles of 75°, 55° and 35° for LS monolayers deposited and thermally annealed on HMDS-modified glass; the inset shows the integrated intensities of the first 1s to π* transition as a function of X-ray incident angle and the linear fit. (b) Experimental XPS spectra for the sulphur 2*p* region for largely edge-on monolayer (Langmuir-Schäfer, LS) and face-on thin film (spin-coated, SC) of P(NDI2OD-T2) on Au. The solid lines are guides to the eyes. Insets: schematics of the NDI2OD-T2 monomer arrangement on surface.

It is well established that the different molecular orientation affects the electronic energy levels and the relative alignment at the organic/(in)organic interfaces.[19] To probe such effect, we performed X-ray photoelectron spectroscopy (XPS). XPS spectra of the sulphur 2*p* core levels of P(NDI2OD-T2) on Au were performed for both LS monolayer (edge-on rich) and spin-coated thin films (face-on rich, Ref. [12]) as reported in Figure 2.4b. Two Gaussian components ($2p_{3/2}$ at 164.30 eV and $2p_{1/2}$ at

165.67 eV) are observed in the face-on regime, which are shifted by an average 0.35 eV towards higher binding energy with respect to the edge-on texture. This shift is also observed for C1s, O1s and N1s core levels and summarized in Table S1 of the Appendix A. It should be noted that the observed binding energy shift represents further support for the predominant edge-on orientation of the polymer backbones in the LS monolayers.[19a] Indeed in analogy to the small-molecule case, the physical origin of this shift is attributed to the intrinsic surface dipole exhibited by the π-conjugated polymer backbone whose magnitude critically depends on the orientation of molecules with respect to the substrate. Thus, in our case quantification of this orientational effect may be underestimated if one considers that spin-coated P(NDI-2OD-T2) films exhibit a prevalent face-on orientation but maintain some out-of-plane/edge-on molecular order.[12] In particular according to Duhm,[19a] our results indicate that the chemical interaction between the ordered polymer chains and the surface produces a slight shift on the binding energy of all the core levels with respect to the randomly oriented polymer chains. As observed for oligothiophenes, the valence levels are affected in the same way as the core levels, which directly translates into a variation of the ionization energy. As a reference for P3HT, a decrease of ionization energy by 0.4 eV from the face-on to the edge-on configurations has been calculated,[20] that is in nice agreement with our findings experiencing such effect for the first time on a polymeric system.

Once we established control on the P(NDI2OD-T2) film morphology and microstructure, we characterized the field-effect transport properties for edge-on monolayers in a staggered top-gate geometry, using PMMA as the gate dielectric (see the inset to Figure 2.5a). Note that PMMA can be deposited by spin coating without significantly affecting the transport layer (see Appendix A, Figure S6). A typical transfer characteristic for a transistor with a channel length of 50 μm and a channel width of 500 μm is shown in Figure 2.5a. The *n*-type monolayer FET shows a relatively small hysteresis with a saturated mobility of 3×10^{-3} cm^2 V^{-1} s^{-1} at gate voltage V_g = 60 V and current on/off ratio > 10^3. Inspection of the output characteristics at low source-drain voltages (Figure 2.5b) reveals excellent electron injection from Au electrodes, in spite of the relatively high mismatch between the gold work function and the LUMO level of the P(NDI2OD-T2). On this respect, it should be noted that the adsorption of a molecular monolayer significantly lowers the vacuum level above the metal surface due to the formation of additional interface dipoles at the metal/organic interfaces.[21] This strong interface dipole layer is expected to affect the injection barrier as already observed for Au/fullerene interfaces.[22] Note that although ambipolar transport characterized by a very weak hole current was reported for spin-coated films of P(NDI2OD-T2)[4d] and confirmed here by us (see Appendix A, Figure

S8), no evidence of hole accumulation is present in the monolayer and multilayered (vide infra) P(NDI2OD-T2) field-effect transistors within the gate bias window we investigated. Remarkably, the electron mobility remains high (2×10^{-3} cm^2 V^{-1} s^{-1}) after 5-weeks storage in air, along with unchanged threshold voltage and current on/off ratio (see Appendix A, Figure S9).

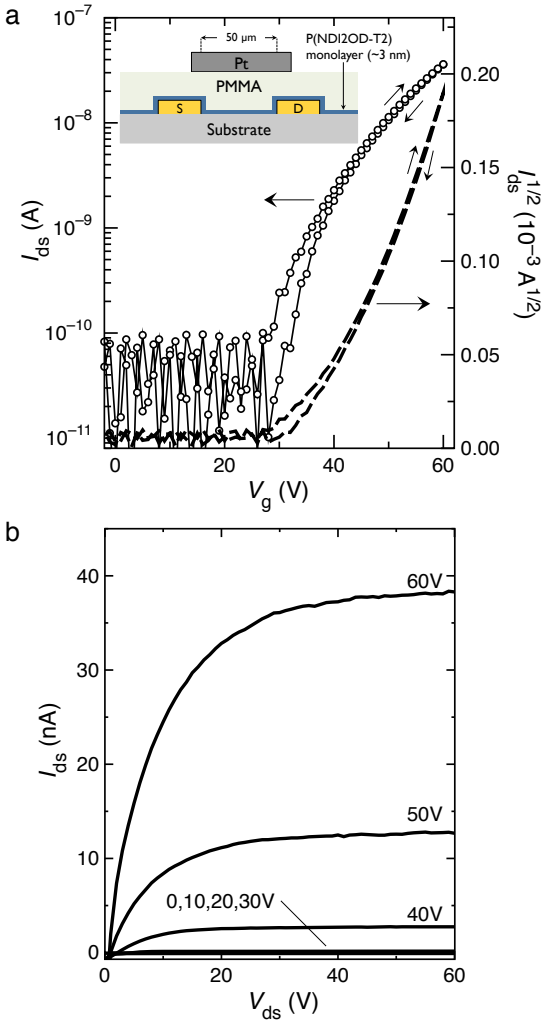

Figure 2.5. (a) Saturated transfer characteristics of a single-layer P(NDI2OD-T2) FET with channel length of 50 μm and channel width of 500 μm, using a drain bias of 60 V. (b) Output characteristics for the corresponding FET. The inset shows the sketch of the bottom-contact/top-gate device with ~600 nm thick PMMA as the gate dielectric (capacitance C_i = 5.4 nF cm^{-2}).

To gain insights into the relationship between polymer organization and charge transport properties, we investigated the evolution of the field-effect transistor perfor-

mances with the number of LS layers from the bare monolayer to multilayer thin films of increasing thickness (see Appendix A, Figure S10-13). Figure 2.6a plots the average field-effect electron mobility as a function of the number of layers (*n*). Interestingly, the mobility increases with the number of layers and saturates at a plateau with a mean value of 0.018 $cm^2 V^{-1} s^{-1}$ upon completion of the third layer. While the hole mobility of multilayered P3HT FETs was found to be insensitive to the film thickness,[8] our results suggest that the field-effect performance of LS P(NDI2OD-T2) is dominated by the inherent transport properties of the polymer in edge-on conformation rather than by the defects within the film. SFM image analysis of the thin films shows an average surface coverage of greater than 99% for the monolayer and 97% for the bilayer and this is in agreement with the relatively small spread of the field-effect mobility values (Figure 2.6a). Thus, we infer that the field-effect current of these devices is sustained by the first three layers, which is a direct evidence of the physical size of the transport layer in P(NDI2OD-T2)-based FETs with edge-on order. Note that such a transport layer may not necessarily coincide with the accumulation layer.[23] In addition, the threshold voltage (V_T) decreases from +40 to +30 V whereas a modulation of the current on/off ratio by more than one order of magnitude is observed, disclosing a non-trivial dependence on the number of layers (Figure 2.6b,c). Note that spin-coating likely affects the structural order of the alkyl side chains at the gate insulator/semiconductor interface. This is expected to introduce traps for charges and influence the resulting V_T. On this respect, the addition of further layers would provide alternative pathways to charge transport. This fact is in agreement with the saturation of V_T and current on/off ratio upon completion of the third layer. Furthermore, the switch-on voltage (V_{so}) of the field-effect, defined as the gate voltage that needs to be applied to reach the flatband condition,[24] varies from +28 V (monolayer FET) to +16 V (15-layers FET) approaching that of spin-coated transistors. The largest charge mobility (0.021 $cm^2 V^{-1} s^{-1}$) is one order of magnitude lower than that commonly observed for spin-coated face-on P(NDI2OD-T2) thin film transistors (~0.1-0.2 $cm^2 V^{-1} s^{-1}$ when using PMMA as gate dielectric, see Ref. [4d] and Figure S14). However, these values are in complete agreement with those reported for top-gated PMMA-based devices after melt annealing of the spun P(NDI2OD-T2) films and this has been correlated by the authors with an increased contact resistance.[14a] Annealing the polymer film above its melting point (i.e. 310 °C) leads in fact to a shift from largely face-on packing to pronounced edge-on texture.[14b] Furthermore, the raising of the LUMO levels due to the edge-on conformation may also negatively affect charge injection from Au. Indeed, although our XPS data provide direct information on the core levels, these could be directly correlated with the valence levels[19a] so that a raising of the LUMO level for the P(NDI2OD-T2) LS films is expected when compared with the spin-coated samples.

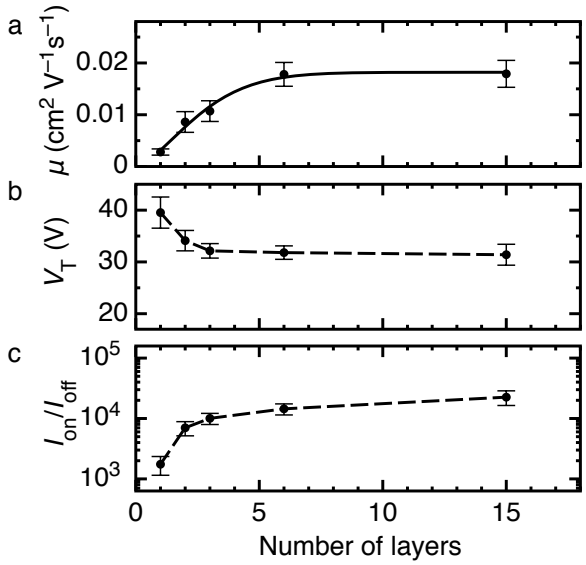

Figure 2.6. Plots of the average electron mobility (a), threshold voltage (b) and on/off ratio (c) versus number of layers (n). The solid line in (a) is the fitting function $\mu \cong \mu_{sat}\{1-\exp[-(n/n_c)^{\alpha}]\}$ yielding a plateau at μ_{sat} = 0.018 cm^2 V^{-1} s^{-1}, crossover number of layers n_c = 3.0 n and exponent α = 1.5. The dotted lines in (b, c) are guides to the eyes.

Although the edge-on molecular packing was found to be beneficial for several high performance polymer FETs due to the fast two-dimensional charge transport along the chain backbone and the π-stacking direction, our findings now clearly demonstrate for the first time that such ordering for P(NDI2OD-T2) is detrimental for transport. Since the field-effect allows charges to populate a few molecular layers of the organic semiconductor in contact with the gate dielectric, a face-on rich packing arrangement (spin-coated films) would lead to a three-dimensional charge transport through subsequent layers coupled by the out-of-plane π-stacking.[12] This directly translates in enhanced electron mobility both in plane and out of plane, as revealed by bulk electron transport measurement.[25] On the other hand, the anisotropy of LS P(NDI-2OD-T2) thin films limits the charge transport to the in-plane direction with inefficient out-of-plane transport between backbones separated by the insulating long octyl-decyl side chains.[3e] Thus, the low electron mobility for LS multilayer FETs is consistent with a reduced interchain vertical transport that may affect the charge accumulation and lower the number of efficient percolation paths. This observation is strengthened by a reduced diode mobility of the edge-on rich (melt-annealed) P(NDI-2OD-T2) films, which was indeed recently reported.[14b]

2.3 Conclusions

In conclusion, developing conjugated polymers that are air-stable, soluble and with excellent transport properties is the key requisite for a next generation of electronic devices. This is because polymers exhibit large chemical versatility allowing the incorporation of both self-assembly and electronic active functions. We demonstrate that P(NDI2OD-T2) allows for the first time to fabricate highly reproducible monolayer polymeric FETs with good structural order and substantial transistor performance. Here we state that, the minimum thickness of this polymeric semiconductor to act as the channel of a field effect transistor is just one layer and that a change in the conformational order (from edge-on to face-on) may be crucial to improve up to one order the mobility of thin film transistors. The realization of a monolayer polymer FET overcomes numerous attempts by different conjugated polymers suggesting that carrier mobility in the first few polymer layers is too low for substantial transistor action. This result opens exciting perspectives for the bottom-up fabrication of nanometer-scale electronic circuit elements as well as for the down-scaling in plastic electronics.

2.4 Experimental details

Materials

Poly{[*N*,*N*'-bis(2-octyldodecyl)-naphthalene-1,4,5,8-bis(dicarboximide)-2,6-diyl]-*alt*-5,5'-(2,2'-bithiophene)} (P(NDI2OD-T2), ActivInk N2200) was used as received (Polyera Corp, Skokie, Illinois). Synthesis and purification are described elsewhere.[4d] All solvents and poly(methyl methacrylate) (PMMA, M_w = 120 kDa) dielectric were purchased from Aldrich and used without further purification.

Film fabrication and characterization

Ordered thin films were prepared by Langmuir-Schäfer (LS) technique on a variety of substrates depending on the particular characterization technique applied. Ultrapure Millipore water with resistivity greater than 18.2 MΩ cm was used as subphase. The experiments were performed at a subphase temperature of 25 °C. All substrates were sonicated for 10 min each in acetone, ethanol and isopropyl alcohol, and dried with nitrogen just before film growth. Prior to deposit, silicon with native oxide substrates were exposed overnight to hexamethyldisilazane (HMDS) vapors after 10 min oxygen-plasma treatment. Films were grown from ~0.2 mg mL^{-1} P(NDI2OD-T2) in

chloroform. Approximately 100 μl of solution was randomly spread onto the aqueous subphase (KSV minitrough apparatus). After solvent evaporation, the film floating at the air/water interface was compressed continuously at a rate of 5 mm min^{-1}. The surface pressure (π) was monitored by a Wilhelmy balance. Deposition was carried out at a surface pressure of 20 mN m^{-1}, by approaching the substrate horizontally to the air/water interface. The LS polymeric films were then left drying in vacuum oven at 150 °C overnight.

Isotropic films were spin-coated from chlorobenzene solution (3-10 mg mL^{-1}) at 1,000 rpm and annealed at 150 °C overnight. All organic film preparation was carried out at room atmosphere.

X-ray photoelectron spectroscopy (XPS) was performed by using a Kratos AXIS-HS Spectrometer. Radiation Al K_α of 1,486.6 eV was used at the conditions of 10 mA and 15 keV. For the XPS analyses the films were deposited onto Au substrate. Areas of 2 × 2 mm^2 were analyzed. Pass energy of 40 eV was used both for survey and core level spectra. The binding energy scale was referred to the Au $4f_{7/2}$ peak centred at 84 eV. During the analysis the base pressure in the chamber was of the order of 10^{-7} Pa. The fitting of XPS spectra was carried out after linear background subtraction with VISION Software (Version 1.4.0) by Kratos Analytical.

Dynamic scanning force microscopy (SFM) was carried out in air using a Multimode Nanoscope IIIa, Digital Instruments, equipped with a phase extender apparatus and a Q-box module in non-destructive dynamic attractive regime. Etched-silicon probes (pyramidal-shape tip, nominal curvature 10 nm, nominal internal angle 35°) were used. During the scanning, the 125-μm-long cantilever, with a nominal spring constant in the range of 20–100 N m^{-1}, oscillated at its resonance frequency (~330 kHz). Height and phase images were collected by capturing 512 × 512 points in each scan and the scan rate was maintained below 1 line per second. During the imaging, temperature and humidity were about 25 °C and 40 %, respectively.

Transistor fabrication and testing

Ordered LS films for device characterization were prepared as described above on HMDS-modified glass substrates with 30 nm Au bottom contacts and 3 nm Cr adhesion layer (channel dimension of W = 500 μm and L = 50 μm, W/L = 10). The substrates were cleaned before film formation. After depositing the LS active layers, samples were annealed in vacuum oven at 150 °C overnight. Top PMMA gate dielectric was spin coated from 70 mg mL^{-1} EtOAc solution at 1,000 rpm (600 nm, k = 3.6) and annealed at 150 °C for 2h. Deposition of the top Pt gate electrode completed the staggered field-effect transistors. The *I/V* characteristics were measured reproducibly in air at room temperature on at least 10 devices per

different film thickness using a Keithley 4200-SCS semiconductor parameter analyzer. Mobility was evaluated in the saturation regime, at a drain voltage V_d = 60 V.

References

[1] a) G. H. Gelinck, H. E. A. Huitema, E. v. Veenendaal, E. Cantatore, L. Schrijnemakers, J. B. P. H. v. d. Putten, T. C. T. Geuns, M. Beenhakkers, J. B. Giesbers, B.-H. Huisman, E. J. Meijer, E. M. Benito, F. J. Touwslager, A. W. Marsman, B. J. E. v. Rens, D. M. d. Leeuw, *Nature Mater.* **2004**, *3*, 106; b) M. Berggren, D. Nilsson, N. D. Robinson, *Nature Mater.* **2007**, *6*, 3; c) A. C. Arias, J. D. MacKenzie, I. McCulloch, J. Rivnay, A. Salleo, *Chem. Rev.* **2010**, *110*, 3; d) H. Sirringhaus, N. Tessler, R. H. Friend, *Science* **1998**, *280*, 1741; e) L. Torsi, G. M. Farinola, F. Marinelli, M. C. Tanese, O. H. Omar, L. Valli, F. Babudri, F. Palmisano, P. G. Zambonin, F. Naso, *Nature Mater.* **2008**, *7*, 412.

[2] a) J.-K. Lee, M. C. Gwinner, R. Berger, C. Newby, R. Zentel, R. H. Friend, H. Sirringhaus, C. K. Ober, *J. Am. Chem. Soc.* **2011**, *133*, 9949; b) H. Bronstein, Z. Chen, R. S. Ashraf, W. Zhang, J. Du, J. R. Durrant, P. S. Tuladhar, K. Song, S. E. Watkins, Y. Geerts, M. M. Wienk, R. A. J. Janssen, T. Anthopoulos, H. Sirringhaus, M. Heeney, I. McCulloch, *J. Am. Chem. Soc.* **2011**, *133*, 3272.

[3] a) A. S. Molinari, H. Alves, Z. Chen, A. Facchetti, A. F. Morpurgo, *J. Am. Chem. Soc.* **2009**, *131*, 2462; b) S. C. B. Mannsfeld, M. L. Tang, Z. Bao, *Adv. Mater.* **2010**, *23*, 127; c) M. A. Loi, E. d. Como, F. Dinelli, M. Murgia, R. Zamboni, F. Biscarini, M. Muccini, *Nature Mater.* **2005**, *4*, 81; d) J. Rivnay, L. H. Jimison, J. E. Northrup, M. F. Toney, R. Noriega, S. Lu, T. J. Marks, A. Facchetti, A. Salleo, *Nature Mater.* **2009**, *8*, 952; e) A. Salleo, R. J. Kline, D. M. DeLongchamp, M. L. Chabinyc, *Adv. Mater.* **2010**, *22*, 3812.

[4] a) G. Horowitz, *J. Mater. Res.* **2004**, *19*, 1946; b) I. McCulloch, M. Heeney, C. Bailey, K. Genevicius, I. MacDonald, M. Shkunov, D. Sparrowe, S. Tierney, R. Wagner, W. Zhang, M. L. Chabinyc, R. J. Kline, M. D. McGehee, M. F. Toney, *Nature Mater.* **2006**, *5*, 328; c) H. Pan, Y. Li, Y. Wu, P. Liu, B. S. Ong, S. Zhu, G. Xu, *J. Am. Chem. Soc.* **2007**, *129*, 4112; d) H. Yan, Z. Chen, Y. Zheng, C. Newman, J. R. Quinn, F. Dötz, M. Kastler, A. Facchetti, *Nature* **2009**, *457*, 679; e) T. Sakanoue, H. Sirringhaus, *Nature Mater.* **2010**, *9*, 736; f) C. J. Bettinger, H. A. Becerril, D. H. Kim, B.-L. Lee, S. Lee, Z. Bao, *Adv. Mater.* **2011**, *23*, 1257.

[5] a) K. Asadi, Y. Wu, F. Gholamrezaie, P. Rudolf, P. W. M. Blom, *Adv. Mater.* **2009**, *21*, 4109; b) L. Li, P. Gao, K. C. Schuermann, S. Ostendorp, W. Wang, C. Du, Y. Lei, H. Fuchs, L. D. Cola, K. Mullen, L. Chi, *J. Am. Chem. Soc.* **2010**, *132*, 8807; c) E. C. P. Smits, S. G. J. Mathijssen, P. A. v. Hal, S. Setayesh, T. C. T. Geuns, K. A. H. A. Mutsaers, E. Cantatore, H. J. Wondergem, O. Werzer, R. Resel, M. Kemerink, S. Kirchmeyer, A. M. Muzafarov, S. A. Ponomarenko, B. d. Boer, P. W. M. Blom, D. M.

d. Leeuw, *Nature* **2008**, *455*, 956; d) S. G. J. Mathijssen, E. C. P. Smits, P. A. v. Hal, H. J. Wondergem, S. A. Ponomarenko, A. Moser, R. Resel, P. A. Bobbert, M. Kemerink, R. A. J. Janssen, D. M. d. Leeuw, *Nature Nanotech.* **2009**, *4*, 674; e) M. Novak, A. Ebel, T. Meyer-Friedrichsen, A. Jedaa, B. F. Vieweg, G. Yang, K. Voitchovsky, F. Stellacci, E. Spiecker, A. Hirsch, M. Halik, *Nano Lett.* **2011**, *11*, 156.

[6] a) J. A. Lipton-Duffin, J. A. Miwa, M. Kondratenko, F. Cicoira, B. G. Sumpter, V. Meunier, D. F. Perepichka, F. Rosei, *Proc. Nat. Acad. Sci. USA* **2010**, *107*, 11200; b) R. Stadler, in *Properties of single organic molecules on crystal surfaces, Vol. 363-387*, Imperial College Press, London and Singapore, **2006**.

[7] H. G. O. Sandberg, G. L. Frey, M. N. Shkunov, H. Sirringhaus, R. H. Friend, M. M. Nielsen, C. Kumpf, *Langmuir* **2002**, *18*, 10176.

[8] G. Xu, Z. Bao, J. T. Groves, *Langmuir* **2000**, *16*, 1834.

[9] J. C. Scott, J. D. J. Samuel, J. H. Hou, C. T. Rettner, R. D. Miller, *Nano Lett.* **2006**, *6*, 2916.

[10] J. H. Oh, Y.-S. Sun, R. Schmidt, M. F. Toney, D. Nordlund, M. Konemann, F. Wurthner, Z. Bao, *Chem. Mater.* **2009**, *21*, 5508.

[11] A. Facchetti, *Chem. Mater.* **2011**, *23*, 733.

[12] J. Rivnay, M. F. Toney, Y. Zheng, I. V. Kauvar, Z. Chen, V. Wagner, A. Facchetti, A. Salleo, *Adv. Mater.* **2010**, *22*, 4359.

[13] H. Sirringhaus, P. J. Brown, R. H. Friend, M. M. Nielsen, K. Bechgaard, B. M. W. Langeveld-Voss, A. J. H. Spiering, R. A. J. Janssen, E. W. Meijer, P. Herwig, D. M. d. Leeuw, *Nature* **1999**, *401*, 685.

[14] a) T. Schuettfort, S. Huettner, S. Lilliu, J. E. Macdonald, L. Thomsen, C. R. McNeill, *Macromolecules* **2011**, *44*, 1530; b) J. Rivnay, R. Steyrleuthner, L. H. Jimison, A. Casadei, Z. Chen, M. F. Toney, A. Facchetti, D. Neher, A. Salleo, *Macromolecules* **2011**, *44*, 5246.

[15] a) M. Gleiche, L. F. Chi, H. Fuchs, *Nature* **2000**, *403*, 173; b) B. Pignataro, *J. Mater. Chem.* **2009**, *19*, 3338.

[16] a) K. S. Lee, T. J. Smith, K. C. Dickey, J. E. Yoo, K. J. Stevenson, Y.-L. Loo, *Adv. Funct. Mater.* **2006**, *16*, 2409; b) S. Fabiano, H. Wang, C. Piliego, C. Jaye, D. A. Fischer, Z. Chen, B. Pignataro, A. Facchetti, Y.-L. Loo, M. A. Loi, *Adv. Funct. Mater.* **2011**, *21*, 4479.

[17] F. W. DelRio, C. Jaye, D. A. Fischer, R. F. Cook, *Appl. Phys. Lett.* **2009**, *94*, 131909.

[18] a) C. K. Chan, L. J. Richter, B. Dinardo, C. Jaye, B. R. Conrad, H. W. Ro, D. S. Germack, D. A. Fischer, D. M. DeLongchamp, D. J. Gundlach, *Appl. Phys. Lett.* **2010**, *96*, 133304; b) H. Wang, E. D. Gomez, J. Kim, Z. Guan, C. Jaye, D. A. Fischer, A. Kahn, Y.-L. Loo, *Chem. Mater.* **2011**, *23*, 2020; c) D. M. DeLongchamp, R. J. Kline, E.

K. Lin, D. A. Fischer, L. J. Richter, L. A. Lucas, M. Heeney, I. McCulloch, J. E. Northrup, *Adv. Mater.* **2007**, *19*, 833.
[19] a) S. Duhm, G. Heimel, I. Salzmann, H. Glowatzki, R. L. Johnson, A. Vollmer, J. P. Rabe, N. Koch, *Nature Mater.* **2008**, *7*, 326; b) W. Chen, D.-C. Qi, H. Huang, X. Gao, A. T. S. Wee, *Adv. Funct. Mater.* **2011**, *21*, 410.
[20] G. Heimel, I. Salzmann, S. Duhm, J. P. Rabe, N. Koch, *Adv. Funct. Mater.* **2009**, *19*, 3874.
[21] H. Ishii, K. Sugiyama, E. Ito, K. Seki, *Adv. Mater.* **1999**, *11*, 605.
[22] S. C. Veenstra, A. Heeres, G. Hadziioannou, G. A. Sawatzky, H. T. Jonkman, *Appl. Phys. A* **2002**, *75*, 661.
[23] F. Dinelli, M. Murgia, P. Levy, M. Cavallini, F. Biscarini, D. M. d. Leeuw, *Phys. Rev. Lett.* **2004**, *92*, 116802.
[24] E. J. Meijer, C. Tanase, P. W. M. Blom, E. v. Veenendaal, B.-H. Huisman, D. M. d. Leeuw, T. M. Klapwijk, *Appl. Phys. Lett.* **2002**, *80*, 3838.
[25] R. Steyrleuthner, M. Schubert, F. Jaiser, J. C. Blakesley, Z. Chen, A. Facchetti, D. Neher, *Adv. Mater.* **2010**, *22*, 2799.

Chapter 3

Effect of thermal stimuli on the supramolecular order

In this chapter we describe the effects of external stimuli such as thermal annealing on the supramolecular order of solution-processed semiconducting molecules. The exceptional molecular orientation regardless of the substrate chemistry is rationalized in terms of strong intermolecular interactions. The remarkable 2D charge carrier mobility measured in field effect transistors underlines the importance of strong intermolecular interactions for the realization of high performing devices.

Published as:
S. Fabiano, H. Wang, C. Piliego, C. Jaye, D. A. Fischer, Z. Chen, B. Pignataro, A. Facchetti, Y-L. Loo and M. A. Loi, *Adv. Funct. Mater.* 2011, **21**, 4479.

3.1 Introduction

The rapid progress in organic material design and device engineering/processing has led to great advances in performance for solution-processed FETs, representing a tremendous opportunity to develop large-area electronics.[1-6] Although the potential of vapour-deposited organic semiconductors is well established, the processing of these materials into high performance transistors from solution remains challenging. Since the electronic properties of the organic semiconductors are closely related to their morphology and supramolecular packing,[7] a specific understanding of the molecular organization dynamics is crucial.[8-10]

Due to their strong intermolecular interactions, small-molecule organic semiconductors have the tendency to self-organize into well-ordered nanostructures with a high degree of crystallinity. This generally leads to high charge-carrier mobility but often the same molecules show limited solution processability.[11] It is well know that surface modifications and post-deposition treatments can control thin-film growth and morphology at a molecular level, influencing the OFET performance, however unless of unique treatments,[12,13] these parameters are rarely able to affect the film morphology on length scales greater than the micron size.[14-16]

Several synthetic strategies has allowed the preparation of solution-processable organic semiconductors, such as high-mobility precursors of pentacene and derived acenes.[12,13,17] Core cyanated arylenediimide semiconductors based on the perylene core (PDIs) have received great attention because of the unique combination of high electron mobility, solution-processability, large reorganization capabilities and environmental stability.[18] Recently, we have reported large electron mobilities up to 0.15 $cm^2\ V^{-1}\ s^{-1}$ with *N,N'*-1*H*,1*H*-perfluorobutyl dicyanoperylenecarboxydiimide (PDIF-CN_2, Polyera ActivInk N1100) in a bottom-gate/bottom-contact geometry, after thermal treatment of the spin-coated films.[19] These transistors showed the unique features of mobility values similar to those reported for vapor-deposited films.[20] Confocal microscopy fluorescence analysis showed an edge-on orientation of the PDIF-CN_2 molecules with respect to the substrate after the annealing treatment, which is presumed to be the reason of the enhanced FETs performance.[19,21]

Based on these results, in this chapter we focus on the understanding of the self-assembling nature of PDIF-CN_2 films upon thermal post-deposition treatment on different surfaces present in the FET structure: the HDMS treated silicon oxide dielectric and the bare and thiol treated gold electrodes. Evidences of a multi-length scale control of the supramolecular order with an exceptional edge-on orientation of the molecules independent of the surface chemistry are found.

The correlation of the supramolecular order with the electrical performance of PDIF-CN_2 in different FET configurations has provided further insight into the relationships between device performances, morphological as well as interfacial features of the active layer.

3.2 Results and discussion

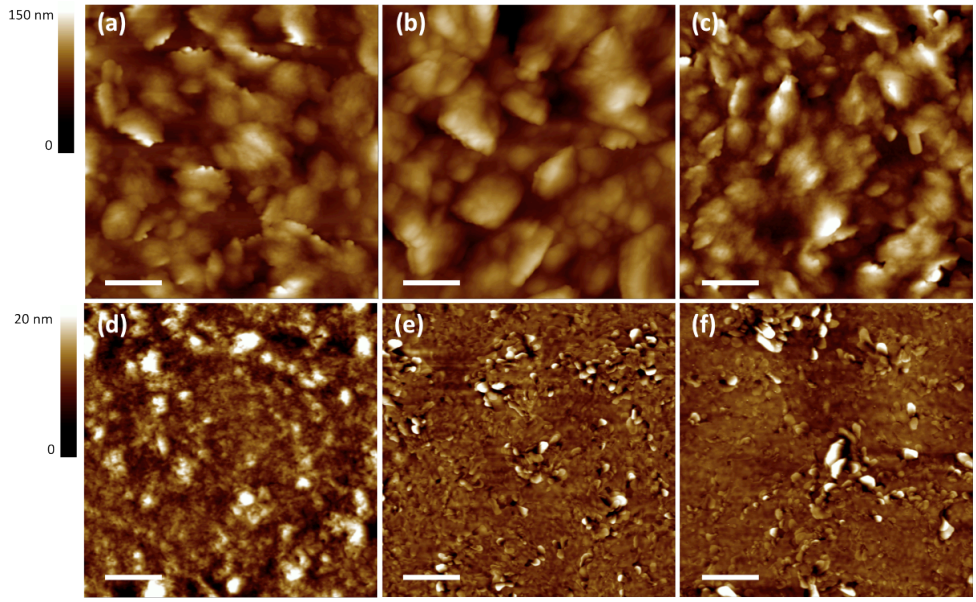

Figure 3.1. Topographic SFM images of spin-coated PDIF-CN_2 thin films as-cast (a-c) and after thermal annealing (d-e) on HMDS modified-silicon oxide (*left*), bare gold (*middle*) and thiol-modified gold (*right*) surfaces. The scale bars are 1 μm.

Figure 3.1 shows the dynamic scanning force microscopy (SFM) analysis for PDIF-CN_2 thin films spin-coated on HMDS-modified silicon oxide (a, d), bare (b, e) and thiol-modified gold (c, f) surfaces. Independent of the substrate type, poor structural order is obtained in the thin films immediately after film deposition (a-c) as the result of a fast self-organization process upon rapid solvent evaporation. The pristine thin film morphology is characterized by segregated nanostructures with an average root mean square roughness of ~15 nm over a 5 × 5 μm^2 area. As reported in a previous work,[19] thermal treatment at 110 °C in vacuum for 1 h promotes an efficient structural reorganization of the thin films (d-f), characterized by smooth and uniform surfaces with an average rms roughness of ~2 nm over a 5 × 5 μm^2 area.

The evolution from large-grained features to a layered morphology is also indicated by the height fluctuation analysis from the power spectral density (PSD) as a function of the spatial frequency *f*,[22] with the SFM images scan size fixed at 5 μm (see Appendix B for further discussion). The PSDs exhibit self-affine scaling, as observed for vapor-deposited thin films of oligothiophenes (Figure 3.2).[23] Interestingly, the roughness scaling exponent α varies from an average of 1.1 to 0.6–0.7 after thermal treatment, indicating that the growth mechanisms of the annealed films are dominated by lamellar reorganization similar to that observed during molecular-beam epitaxy growth.[22]

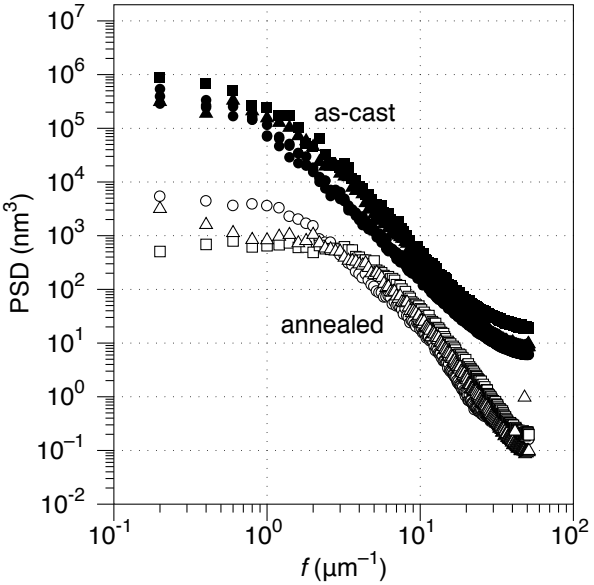

Figure 3.2. Power spectral density (PSD) as a function of the spatial frequency for as-cast and annealed PDIF-CN_2 thin films on HMDS-modified (*circle*), bare (*square*) and thiol-modified (*triangle*) substrates.

Such a molecular and supramolecular ordering is well displayed at higher magnification in non-contact dynamic SFM images of annealed PDIF-CN_2 thin films on HMDS-treated substrates, demonstrating a layer-by-layer growth with closed molecular planes separated from each other by a monomolecular step of 21.2 Å (Figure 3.3a). The molecular step measured experimentally is in good agreement with the 22.8 Å long axis determined from the crystal structure[20] (Figure 3.3b) and is consistent with an out-of-plane structural reorganization of the perylene diimide core. This slip-stacked face-to-face molecular packing, resulting from the van der Waals interactions between the fluoroalkyl chains attached to the perylene cores and the π-π orbital

overlap between the cores, has been also observed for other vapor-deposited perylene derivatives.[20,24]

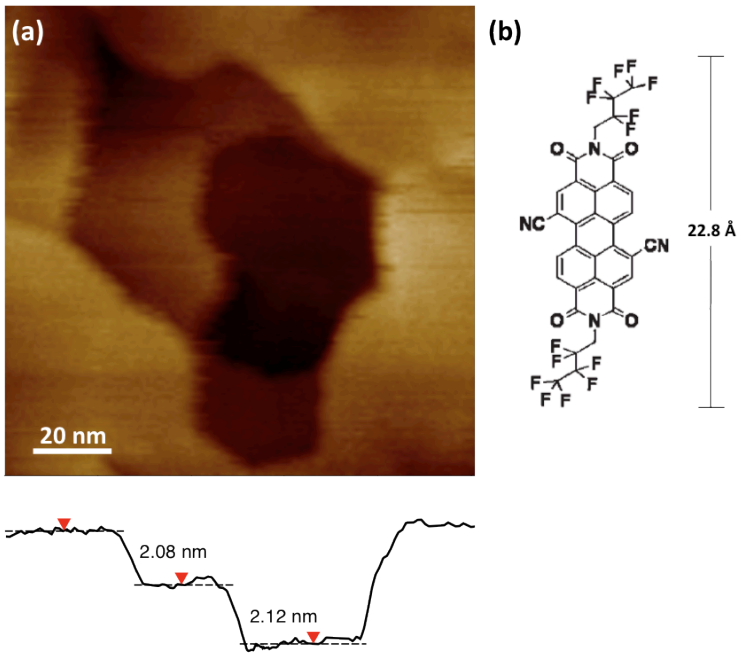

Figure 3.3. (a) High-magnification non-contact dynamic SFM image (*top*) and section analysis (*bottom*) of annealed PDIF-CN_2 thin films on HMDS modified-silicon oxide surface. The step height is consistent with the 22.8 Å long axis distance (b).

To have a quantitative experimental understanding of the PDIF-CN_2 order we performed NEXAFS spectra of the thin film deposited on different surfaces. The NEXAFS spectra are acquired at the carbon edge at different X-ray incident angles for PDIF-CN_2 thin films. Variations in incident angle have allowed us to determine the ensemble-average orientation of the molecules in the different thin films. The pre- and post-edge normalized NEXAFS spectra of PDIF-CN_2 deposited on HMDS modified-silicon oxide substrates before and after thermal annealing at 110°C are shown in Figures 3.4a and 3.4b, respectively. To identify the resonances associated with PDIF-CN_2, we first generated a difference spectrum by subtracting the NEXAFS spectrum at one incident angle from that at another.[25-28] Inspection of the different spectra indicates peaks – both positive and negative in intensities – that can be assign to specific resonances of PDIF-CN_2. Specifically, we have identified the peaks at 284.0, 284.7, 285.6, 287.4, 288.0, 288.8, and 290.4 eV as π^* resonances associated with C=C, C≡N and C=O bonds of PDIF-CN_2. The positions of the σ^* resonances of

PDIF-CN_2 that are associated with C-C, C-F, C-H, C-N bonds can be found at 286.8, 293.2, 295.3, 297.4, 301.9 eV.

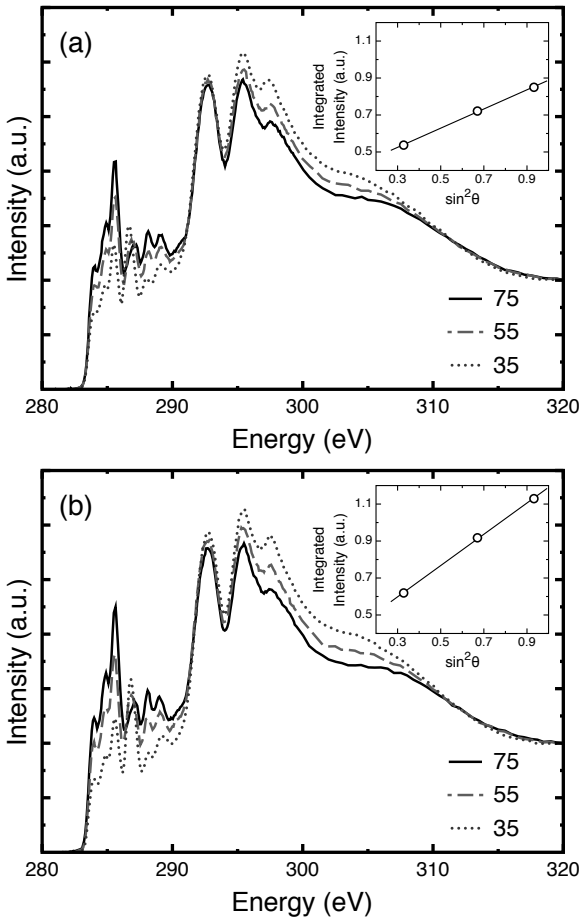

Figure 3.4. Pre- and post-edge normalized NEXAFS spectra acquired at the carbon edge at three different X-ray incident angles, 75°, 55° and 35° for as-cast (a) and thermally annealed (b) PDIF-CN_2 on HMDS modified-silicon oxide. Insets: the integrated intensities of the first 1s to π^* transition as a function of X-ray incident angle and the linear fits for as-cast (a) and thermally annealed (b) PDIF-CN_2 on HMDS modified-silicon oxide.

As evinced in the inset of Figures 3.4a and b where the integrated intensity of the first C1s to π^* transition is plotted against the X-ray incident angle, the NEXAFS spectra acquired on PDIF-CN_2 before thermal annealing shows far less dependence on the X-ray incident angle compared to the NEXAFS spectra acquired after thermal annealing. Since variations in intensities with incident angles indicate changes in the interactions between the molecular orbitals[25] of PDIF-CN_2 with the electric field of

the incident X-rays, quantification of these variations should provide information about the ensemble-average molecular orientation of this system. Returning to Figure 3.4a, we observe that the π* resonances are more intense when the X-ray incident angle is 75° compared to when the incident angle is 35°. This observation suggests that the π* orbitals of PDIF-CN_2 are more oriented in the direction of the electric field when the X-ray incident angle is 75°, as opposed to 35°. Given that the intensity variations of the σ* resonances is opposite those of the π* resonances, the σ* planes must be more aligned with the electric field when the X-ray incident angle is 35°. Taken together, the phenomenon in which the π* resonances grow at the expense of the σ* resonances with increasing X-ray incident angles indicates that PDIF-CN_2 in the as-cast film is already oriented with their ring planes perpendicular to the substrate before thermal annealing. The NEXAFS spectra in Figure 3.4b shows the same intensity variations, in which the π* resonances grow at the expense of the σ* resonances, albeit to a larger extent. This increase in intensity variations of the NEXAFS spectra in Figure 3.4b compared to those in Figure 3.4a suggests that the extent of orientation of PDIF-CN_2 is further increased after annealing. We also conducted similar NEXAFS experiments on PDIF-CN_2 cast on other substrates, including bare gold and thiol-modified gold, before and after thermal annealing. The pre- and post-edge normalized NEXAFS spectra as a function of X-ray incident angles are shown in Figure S1 of the Appendix B. Our NEXAFS experiments indicate that as-cast PDIF-CN_2 films are least oriented on bare gold; thermal annealing induces the molecules to further orient upright.

We can further quantify the extent of preferential orientation of PDIF-CN_2 by examining the integrated intensity of its 1s to π* transition as a function of incident angle. The insets of Figures 3.4a and 3.4b display the integrated intensity of the first 1s to π* transition as a function of X-ray incident angles for PDIF-CN_2 films cast on HMDS modified-silicon oxide before and after thermal annealing, respectively. The slopes of the integrated intensities as a function of incident angles thus indicate the extent of PDIF-CN_2 molecular orientation[25] before and after thermal annealing. This extent of orientation can be quantified by examining the dichroic ratio (*DR*)[25] extracted from the integrated intensities of the first 1s to π* transition, attributed to the C=C resonance:

$$DR = \frac{I(90°) - I(0°)}{I(90°) + I(0°)} \tag{3.1}$$

In equation (3.1), $I(90°)$ and $I(0°)$ represents the integrated intensities of the 1s to π^* transition of interest at X-ray incident angles of 90° and 0°, respectively, which are extrapolated from a linear fit of the integrated intensities, such as that demonstrated in the insets of Figures 3.4a and 3.4b. An extracted *DR* that is > 0 indicates the molecules are preferentially oriented with its ring plane upright; a *DR* that is < 0 indicates the molecules are preferentially oriented with its ring plane parallel to the substrate; and a *DR* that is near 0 implies the absence of preferential orientation in the molecular assembly.[27,28] The extracted *DR* values for all the PDIF-CN_2 films examined are summarized in Table 3.1. For all the PDIF-CN_2 films studied, we observe uniformly high *DR* values after thermal annealing. In fact, *DR* values for these films range from 0.55 to 0.58, which are among the highest values ever reported for solution-processed organic semiconductor thin films. This observation suggests that thermally annealed PDIF-CN_2 film exhibit highly oriented molecules with the ring planes preferentially upright regardless of the nature of the substrate. We observe, however, significant variations in the *DR*'s for the as-cast PDIF-CN_2 films on different substrates. As-cast films on gold have molecules less oriented with a *DR* = 0.28 whereas on HMDS modified-silicon oxide and on thiol-modified gold they are more oriented, with *DR*'s of 0.4-0.5. We conclude that PDIF-CN_2 films undergo significant structural rearrangement upon thermal annealing resulting in an increase in the extent of preferential orientation over a large range, which is about 1 mm^2 if one considers the spot size of the NEXAFS experiment.

Table 3.1. Dichroic ratios (*DR*s) for PDIF-CN_2 on different substrates.

	DR
On gold; as-cast	0.28
On gold; annealed	0.57
On HMDS modified-silicon oxide; as-cast	0.41
On HMDS modified-silicon oxide; annealed	0.55
On thiol-modified gold; as-cast	0.44
On thiol-modified gold; annealed	0.58

The strong tendency of PDIF-CN_2 films to reorganize upon thermal treatment on all surfaces investigated here is also demonstrated by the decrease of surface energy from an average value of 18.5 mJ m^{-2} to 14.5 mJ m^{-2} before and after annealing, respectively, as determined by contact angle measurements (see Appendix B, Table S1). The increased hydrophobicity is presumably consistent with the self-assembly of the closely-packed fluoroalkyl side chains at the organic/air interface. Moreover it is inter-

esting to note that these chains provide also a kinetic barrier to air penetration.[29] This reflects the good air stability observed for PDIF-CN_2-based FETs over more than 3 weeks together with the almost total recovery of the initial mobility under vacuum.[19]

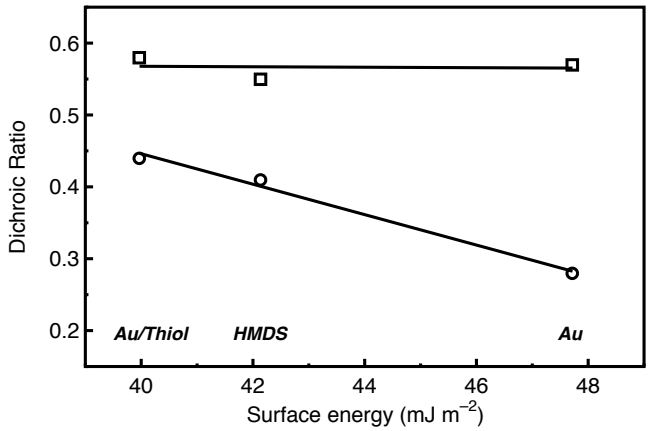

Figure 3.5. Dichroic ratio as a function of the surface energy for as-cast (circle) and annealed (square) thin films on HMDS, bare and thiol-modified gold substrates. The solid lines are guides to the eye.

Figure 3.5 shows the NEXAFS dichroic ratio as a function of the surface energy of the substrate (see also Appendix B, Table S2). As expected, an increase in the surface tension markedly reduces the molecular and supramolecular order for the as-cast thin films. Interestingly the molecular reorganization after thermal annealing is independent of the surface energy of the substrates, suggesting that, at least on these surfaces, the molecule-molecule interactions play a major role with respect to the molecule-substrate interactions. Such a remarkable self-assembling behaviour is likely due to the PDIF-CN_2 low surface energy and it is also corroborated by previous results for vapor-deposited PDIF-CN_2 films. In the films obtained by evaporation, PDIF-CN_2 forms planes on silicon oxide, polystyrene and HMDS-treated silicon oxide similarly to those we observed here. A different morphology is reported for PDIF-CN_2 film evaporated on octadecyltrichlorosilane (OTS)-modified silicon oxide having a surface free energy (~20 mJ m^{-2}) very close to that of PDIF-CN_2.[30] In fact, the small molecules growth modes are determined by a competition between molecule-molecule and molecule-substrate interactions. For substrates with surface energies higher than those of the organic molecules (see for instance pentacene[31,32]), a layer-by-layer growth mode is expected in the formation of the thin films.[33] This is the case of PDIF-CN_2 thin film: since its surface energy is always lower than that of all the studied substrates, a lamellar reorganization is obtained at the equilibrium.

In order to explore the influence of the exceptional degree of edge-on orientation of PDIF-CN_2 on the transport properties, we tested the performance of PDIF-CN_2

based FETs with different architectures. With the aim of supporting our observations on the supramolecular organization of the compound regardless of the surface energy of the substrates, we compared the performances of bottom-contact (bottom-gate) devices with and without the thiol treatment of the gold contacts. Moreover, in order to clarify if the presence of gold has an influence on the reorganization process upon annealing, we also tested the performance of PDIF-CN_2 deposited on HDMS-functionalized silicon dioxide substrates in a top-contact (bottom-gate) configuration. The gate insulator and contacts surfaces were modified by self-assembling HMDS and thiol monolayers (as described in the experimental part), following the procedure previously reported.[19]

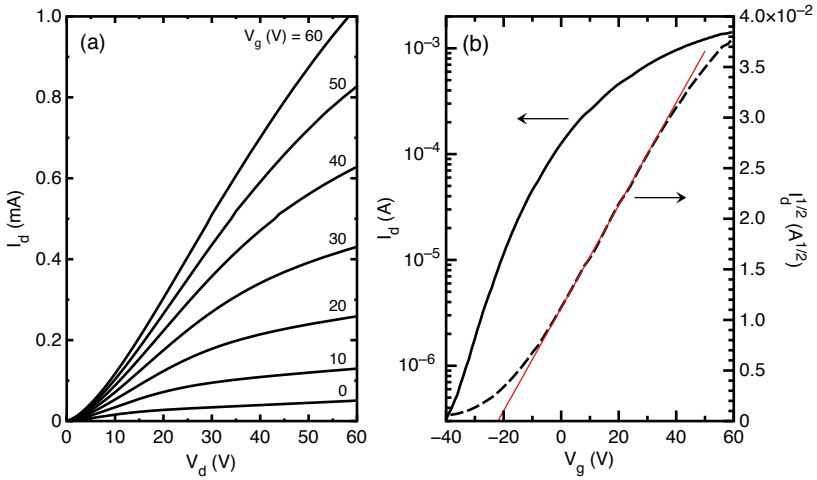

Figure 3.6. Output (a) and transfer (b) characteristics for an as-cast 3 μm channel length PDIF-CN_2 FET with thiol-modified source/drain bottom contacts.

Figure 3.6a shows typical output characteristics for a FET of as-cast PDIF-CN_2 with thiol-modified electrodes. The device has a channel length (L) of 3 μm and a channel width (W) of 10.000 μm. At low drain voltages (V_d), the device operation shows a non-ideal behaviour with clear *s*-shaped drain current (I_d), indicating an injection barrier. In addition, no saturation occurs at high drain voltages, originating from the large contact resistance at the perylene/electrodes interface. Figure 3.6b shows the transfer characteristics for the same device biased in the saturation regime at a drain voltage of 50 V. The deviation from ideal behaviour for large gate voltages (V_g) gives further evidence that charge transport is limited by injection over/trough a potential barrier. The on/off ratio is larger than 10^3, whereas the calculated field-effect mobility (μ) and the extracted threshold voltage are 7×10^{-3} cm^2 V^{-1} s^{-1} and –22 V, respectively.

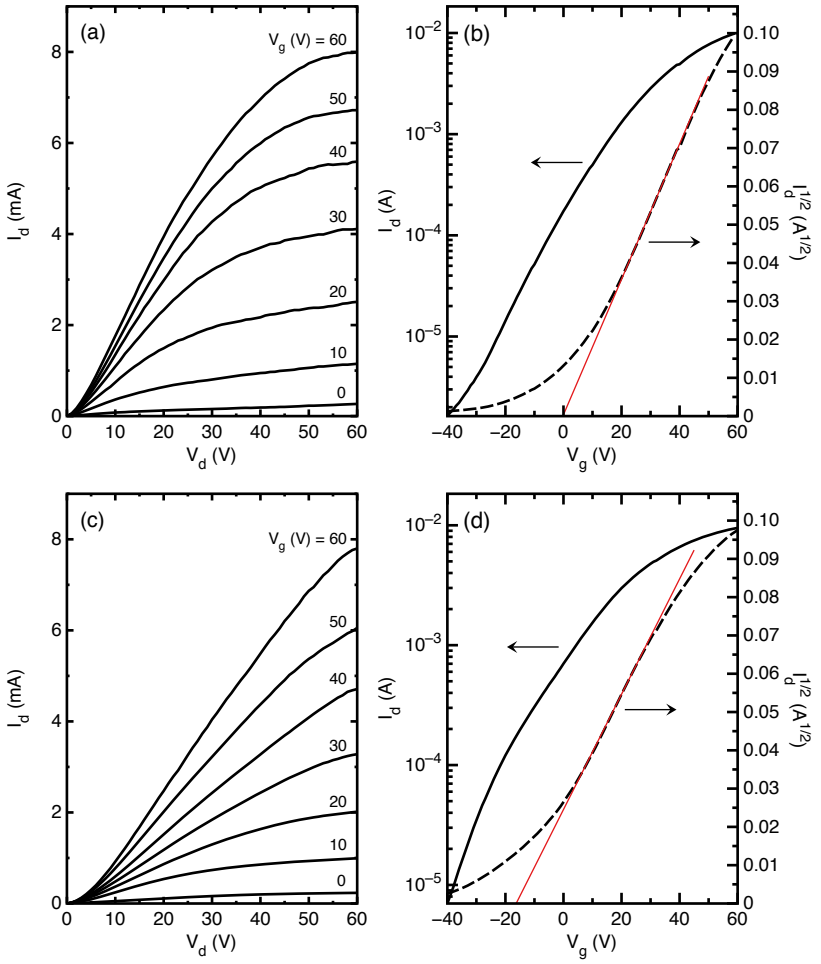

Figure 3.7. Output and transfer characteristics of 3 μm channel length PDIF-CN_2 FETs with thiol-modified (a, b) and bare (c, d) bottom electrodes after annealing at 110 °C in vacuum for 1 h.

Figure 3.7a shows the typical drain current versus drain voltage characteristics recorded at different gate biases for a representative PDIF-CN_2 FET with thiol-modified electrodes after annealing. With respect to the as-cast film (see Figure 3.6), after the thermal treatment at 110 °C in vacuum for 1 h, the PDIF-CN_2-based FETs exhibit a reduced injection barrier, although a slight contact effect is still visible. Furthermore, mobility values as high as 0.14 $cm^2\ V^{-1}\ s^{-1}$, threshold voltages near zero, and on/off current ratios close to 10^4 are measured (Figure 3.7b). The marked enhancement of the on/off ratios with respect to the pristine devices and the increased mobility promoted by thermal post-deposition treatment are in agreement with the high perfor-

mance mobility previously reported.[19] These results correlate to the higher levels of molecular order and minimization of the film-surface irregularities observed by NEXAFS and SFM. Additionally, the striking difference in the threshold voltage for the as-cast (V_T = –22 V) and annealed (V_T ~ 0V) devices might be ascribed to variations in the trapped charges density at the gate insulator/semiconductor interface, as reported for PDIF-CN_2 single crystal transistors.[34]

Although thiol treatment of the electrical contact increases the mismatch between the electrode work function (at ~5.6 eV from Kelvin Probe measurements) and the lowest unoccupied molecular orbital level of the semiconductor (at ~4.5 eV from cyclic voltammetry[20]), it is found to play an important role in improving some of the device characteristics. In fact, thiols have not only the role of tuning the electrode electronic energy levels but they also dramatically reduce the surface free energy preventing the dewetting at the metal contacts. In this respect, a larger injection barrier is clearly prominent in the linear regime as well as in the saturation regime of the annealed PDIF-CN_2-based FETs with untreated Au when compared with thiol-modified electrodes (Figure 3.7c), demonstrating remarkably that the interfacial morphology dominates the FET performances rather than semiconductor-electrical contact energetics. As recently stated for OFETs with printed PEDOT:PSS electrodes compared to gold electrodes,[35] the difference in morphology at the electrode/semiconducting channel boundary severely affects the contact resistances. Consequently, the unmodified transistor displays a threshold voltage of ~ –16 V, on/off ratio close to 10^3 and field-effect mobility of 0.10 $cm^2\ V^{-1}\ s^{-1}$ (Figure 4.8d). Since the electron mobility is still well within the high mobility range previously reported for devices with treated contacts, we can conclude that the molecular organization inside the channel is not affected by the thiol treatment.

In order to verify this conclusion we realized top-contact FET to test the behavior of the material on HMDS-modified silicon oxide surface without the influence of the gold electrodes. In a top-contact configuration indeed, the molecular ordering of the spin-coated films upon annealing is not affected by any electrodes pre-patterned on the substrate. Devices fabricated from annealed PDIF-CN_2 thin films, with channel length of 100 μm and channel width of 1300 μm (Figure 3.8), show charge-carrier mobility of 0.18 $cm^2\ V^{-1}\ s^{-1}$, along with threshold voltage and on/off ratio of 5 V and 10^2, respectively. The low on/off ratio value is probably due to the large area of the evaporated gold contacts that induces high parasitic currents, so that using different contact geometry could enhance both values of mobility and on/off ratio. However, a slight residual doping of the semiconductor may also play a role as corroborated by a careful observation of the output curves in Figure 3.7a. These results, even if not optimised, confirm that the ability of PDIF-CN_2 to self-organize upon annealing is

independent of the nature of the surface. Moreover, this indicates that in the bottom-contact configuration, the electrodes contact edge do not affect the molecular packing but only the morphology at the interface and the propagation of grains into the channel.

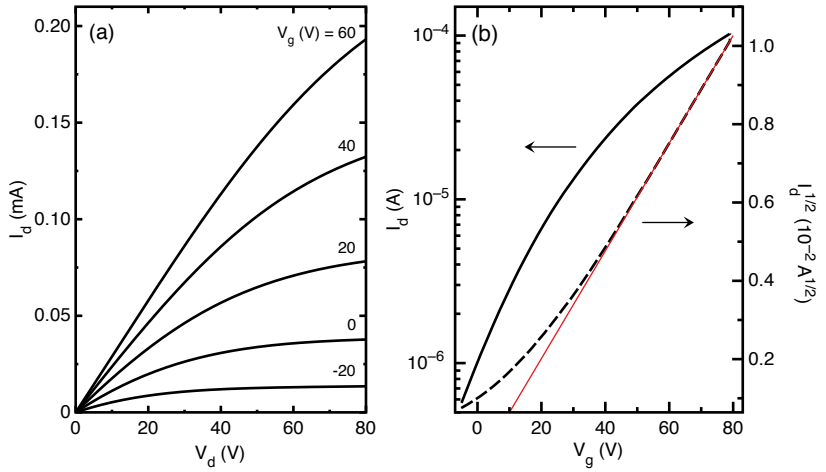

Figure 3.8. Output (a) and transfer (b) characteristics for an annealed top-contact PDIF-CN_2 FET with channel length of 100 μm and channel width of 1300 μm.

This result is also corroborated by the remarkable dependence of the electron mobility on the device channel length (L). Figure 3.9 shows μ versus L for a representative batch of PDIF-CN_2 FETs, fabricated with thiol-treated contacts. Interestingly, unlike what typically stated for OFETs[36], the field-effect mobility in saturation (V_d = 50 V) decreases with increasing L. Although short channel effects can artificially increase the apparent mobility for sub-10 micrometers channel lengths[37], this is not our case since no significative differences have been observed by measuring the mobility in saturation at different drain biases. A similar qualitative trend has been observed for solution-processed acene-based transistors, for which a contact-induced crystallinity has been reported.[38] Due to the polycrystalline nature of the PDIF-CN_2 film, the growth/propagation of grain boundaries into the transistor channel affects the charge transport, so that channel resistances (R_{ch}) cannot be neglected. However, the probability for the existence of effective percolating paths between source and drain depends indeed on the channel length, and increases with decreasing L. In general, increased grain connectivity at the gate insulator interface enhances charge transport.[39-41] Therefore the mobility reduction with L is due to a decreased I_{on} that probably accompanies the reduced percolating paths. However, it is noteworthy that no significant variation in the on/off ratio occurs over the whole channel lengths

range, indicating a similar limiting effect of the grain boundaries on the off currents with depletion of the charge carriers.

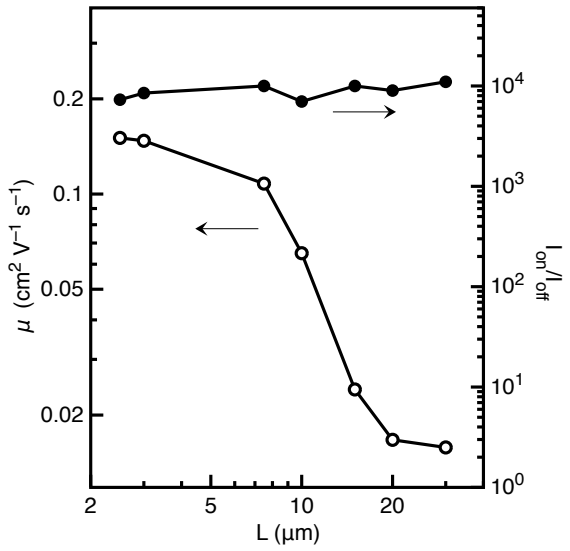

Figure 4.9. Saturation mobility and on/off ratio as functions of the channel length (*L*) for PDIF-CN_2-based FETs with thiol-modified bottom electrodes after annealing at 110 °C in vacuum for 1 h.

3.3 Conclusions

In conclusion, we have demonstrated the exceptional supramolecular packing and molecular orientation for solution-processed films upon annealing on several substrates by combining dynamic near-edge X-ray absorption fine structure spectroscopy (NEXAFS), scanning force microscopy (SFM) and surface energy measurements. Remarkably, such a long-range supramolecular order, induced by the strong intermolecular π-π stacking interactions, is comparable to that observed for highly oriented vapor-deposited acenes.[16] The ability of this material to show high values of mobility regardless of the surface is an indication that the molecule-molecule interactions are predominant respect to the molecule-substrate interactions. These findings underline some fundamental characteristics that a solution processable small molecule should have in order to perform well in a FET, pointing out that PDIs can be used as model systems for fundamental studies on charge injection and transport in OFETs.

3.4 Experimental details

Materials

N,N'-1H,1H-perfluorobutyl dicyanoperylenecarboxydiimide (PDIF-CN_2, Polyera ActivInk N1100) was used as received from Polyera Corp, Skokie, IL, US.

Film fabrication

A solution of PDIF-CN_2 in chloroform was employed with a concentration of 5-6 mg mL^{-1} and filtered with syringe filters of polytetrafluoroethylene (0.2 μm) before use. PDIF-CN_2 thin films were fabricated in a nitrogen-filled glovebox (< 0.1 ppm O_2 and H_2O) by spin-coating the semiconductor solution on several surfaces: self-assembled monolayer modified-silicon oxide; bare gold and thiol-modified gold surfaces. Substrates with native oxide were at first cleaned in acetone, isopropanol under ultrasonication and subsequently treated by UV-ozone plasma for 20 min to remove any traces of organic contaminants. Substrates were then modified with a hexamethyldisilazane (HMDS) self-assembled monolayer, whereas 30 nm of Au on 1 nm of Cr as adhesion layer were thermally evaporated onto the untreated ones. The gold surface were subsequently immersed in a 10 mM solution of 3,5-bis(trifluoromethyl)benzenethiol in ethanol for 1 h. PDIF-CN_2 thin films were spin-coated at 1500 rpm and annealed in vacuum oven at 110 °C for 1 h.

SFM, NEXAFS and contact angle characterization

The morphology of the PDIF-CN_2 thin films has been inspected by dynamic scanning force microscopy (SFM) under ambient conditions using a Multimode Nanoscope IV (Digital Instruments, Santa Barbara, CA). Non-contact dynamic SFM was performed by using a phase extender apparatus and Q-box module. Etched-silicon probes with a pyramidal-shape tip having a nominal curvature of 10 nm and a nominal internal angle of 35° were used. The AFM image were recorded with a resolution of 512 × 512 at a tip resonance frequency of 330 kHz.

Near edge X-ray absorption fine structure (NEXAFS) experiments were carried out at the NIST/DOW soft X-ray materials characterization facility located at beamline U7A at the National Synchrotron Light Source at Brookhaven National Laboratories. Partial electron yield (PEY) NEXAFS spectra were acquired at the carbon K-edge at X-ray incident angles of 35° (grazing), 55° (magic angle) and 75° (near-normal), normalized by the corresponding incident beam intensity, and the spectra were subsequently pre- and post-normalized. The polarization factor of the soft X-ray is 85%.[25-28] Given the applied bias, the PEY detector is only sensitive to auger

electrons emitting from the top 2 nm of the active layer.[25,42,43] The ensemble-average preferential orientation of PDIF-CN_2 in the top 2 nm of the active layer can be quantitatively assessed by examining the variations in the integrated intensity associated with the 1s to π^* transitions of the double bonds as function of X-ray incident angle.[25] We scanned in increments of 0.1 eV in the region of interests (280-300 eV) and in increments of 2 eV at the 250-270 eV, 0.5 eV at the 270-280 eV, 0.5 eV at the 300-330 eV and 2 eV at the 330-400 eV regions.

Static contact angle measurements were carried out at room temperature by using a Device Dataphysics equipped with SCA 20 (3.60.2 software). 2 μL drops of deionized water and diiodomethane were used as test liquids and deposited on tested surfaces (sessile drop method). Their profiles were then fitted with the Young-Laplace equation. Values are averages of at least six measurements recorded at different positions of each substrate. Surface energy was calculated by fitting the measured values of the contact angles with the Young-Dupre equation.

Transistor fabrication and testing

PDIF-CN_2-based FETs with a bottom-gate/bottom-contact geometry were fabricated by spin-coating the semiconductor solution (6 mg mL^{-1}) on heavily doped *p*-type Si substrates with a 200 nm thick thermally grown SiO_2 layer as the gate dielectric (C_d = 17 nF cm^{-2}). Interdigitated source and drain electrodes were defined lithographically and consist of 10 nm of Ti and 30 nm of Au. All the substrate were first dipped in a Piranha solution (demi water 100 mL + ammonia (30%) 25 mL + H_2O_2 25 mL) for 90 s at 60 °C to remove all the organic contaminants from the metal surface as well as from the oxide. The substrates were then cleaned stepwise in acetone and isopropanol in an ultrasonic bath and treated by UV-Ozone plasma for 20 min. Before the deposition of PDIF-CN_2, both HMDS and thiol treatments were performed following the procedure reported above. The active layer was then spin-coated at 1500 rpm and annealed in vacuum oven at 110 °C for 1 h. Both the SAM treatment and the PDIF-CN_2 deposition were carried out in a controlled atmosphere glovebox filled with N_2. For the top-contact device, after the application of HDMS on the cleaned substrates and the spin-coating of the active layer as described above, 100 nm of gold were evaporated. The transistors were measured in vacuum at room temperature using a Keithley 4200-SCS semiconductor parameter analyzer. Mobility was evaluated in the saturation regime, at a drain voltage V_d = 50 V for the bottom-contact and V_d = 80 V for the top-contact.

References

[1] a) J. Zaumseil, H. Sirringhaus, *Chem. Rev.* **2007**, *107*, 1296. b) H. Klauk, *Chem. Soc. Rev.* **2010**, *39*, 2643. c) A. Facchetti, *Chem. Mater.* **2011**, *23*, 733.
[2] a) S. S. Lee, Y.-L. Loo, *Annu. Rev. Chem. Biomol. Eng.* **2010**, *1*, 59. b) A. Salleo, R. J. Kline, D. M. DeLongchamp, M. L. Chabinyc, *Adv. Mater.* **2010**, *22*, 3812. c) A. C. Arias, J. D. MacKenzie, I. McCulloch, J. Rivnay, A. Salleo, *Chem. Rev.* **2010**, *110*, 3.
[3] a) K.-J. Baeg, D. Khim, J.-H. Kim, M. Kang, I.-K. You, D.-Y. Kim, Y.-Y. Noh, *Org. Electron.* **2011**, *12*, 634. b) D. Braga, G. Horowitz, *Adv. Mater.* **2009**, *21*, 1473.
[4] J. H. Cho, J. Lee, Y. Xia, B. Kim, Y. He, M. J. Renn, T. P. Lodge, C. D. Frisbie, *Nat. Mater.* **2008**, *7*, 900.
[5] S. R. Forrest, *Nature* **2004**, *428*, 911.
[6] A. Facchetti, *Mater. Today* **2007**, *10*, 28.
[7] H. Sirringhaus, P. J. Brown, R. H. Friend, M. M. Nielsen, K. Bechgaard, B. M. W. Langeveld-Voss, A. J. H. Spiering, R. A. J. Janssen, E. W. Meijer, P. Herwig, D. M. d. Leeuw, *Nature* **1999**, *401*, 685.
[8] M. A. Loi, E. d. Como, F. Dinelli, M. Murgia, R. Zamboni, F. Biscarini, M. Muccini, *Nat. Mater.* **2005**, *4*, 81.
[9] B. Pignataro, *J. Mater. Chem.* **2009**, *19*, 3338.
[10] S. Fabiano, B. Pignataro, *Phys. Chem. Chem. Phys.* **2010**, *12*, 14848.
[11] S. Allard, M. Forster, B. Souharce, H. Thiem, U. Scherf, *Angew. Chem. Int. Ed.* **2008**, *47*, 4070.
[12] K. C. Dickey, J. E. Anthony, Y.-L. Loo, *Adv. Mater.* **2006**, *18*, 1721.
[13] S. S. Lee, C. S. Kim, E. D. Gomez, B. Purushothaman, M. F. Toney, C. Wang, A. Hexemer, J. E. Anthony, Y.-L. Loo, *Adv. Mater.* **2009**, *21*, 3605.
[14] S. Y. Yang, K. Shin, C. E. Park, *Adv. Funct. Mater.* **2005**, *15*, 1806.
[15] A. A. Virkar, S. Mannsfeld, Z. Bao, N. Stingelin, *Adv. Mater.* **2010**, *22*, 3857.
[16] K. S. Lee, T. J. Smith, K. C. Dickey, J. E. Yoo, K. J. Stevenson, Y.-L. Loo, *Adv. Funct. Mater.* **2006**, *16*, 2409.
[17] J. E. Anthony, *Angew. Chem. Int. Ed.* **2008**, *47*, 452.
[18] X. Zhan, A. Facchetti, S. Barlow, T. J. Marks, M. A. Ratner, M. R. Wasielewski, S. R. Marder, *Adv. Mater.* **2011**, *23*, 268.
[19] C. Piliego, D. Jarzab, G. Gigli, Z. Chen, A. Facchetti, M. A. Loi, *Adv. Mater.* **2009**, *21*, 1573.
[20] B. A. Jones, M. J. Ahrens, M.-H. Yoon, A. Facchetti, T. J. Marks, M. R. Wasielewski, *Angew. Chem. Int. Ed.* **2004**, *43*, 6363.
[21] C. Piliego, F. Cordella, D. Jarzab, S. Lu, Z. Chen, A. Facchetti, M. A. Loi, *Appl Phys A* **2009**, *95*, 303.

[22] F. Biscarini, P. Samorì, O. Greco, R. Zamboni, *Phys. Rev. Lett.* **1997**, *78*, 2389.
[23] M. Melucci, M. Gazzano, G. Barbarella, M. Cavallini, F. Biscarini, P. Maccagnani, P. Ostoja, *J. Am. Chem. Soc.* **2003**, *125*, 10266.
[24] W. Wang, C. Du, D. Zhong, M. Hirtz, Y. Wang, N. Lu, L. Wu, D. Ebeling, L. Li, H. Fuchs, L. Chi, *Adv. Mater.* **2009**, *21*, 4721.
[25] J. Stohr, *NEXAFS Spectroscopy*, Springer: Berlin, **1992**.
[26] D. A. Outka, J. Stohr, J. P. Rabe, J. D. Swalen, *J. Chem. Phys.* **1988**, *88*, 4076.
[27] D. A. Krapchetov, H. Ma, A. K. Y. Jen, D. A. Fischer, Y.-L. Loo, *Langmuir* **2005**, *21*, 5887.
[28] D. A. Krapchetov, H. Ma, A. K. Y. Jen, D. A. Fischer, Y.-L. Loo, *Langmuir* **2008**, *24*, 851.
[29] R. T. Weitz, K. Amsharov, U. Zschieschang, E. B. Villas, D. K. Goswami, M. Burghard, H. Dosch, M. Jansen, K. Kern, H. Klauk, *J. Am. Chem. Soc.* **2008**, *130*, 4637.
[30] B. A. Jones, A. Facchetti, M. R. Wasielewski, T. J. Marks, *Adv. Funct. Mater.* **2008**, *18*, 1329.
[31] R. Ruiz, D. Choudhary, B. Nickel, T. Toccoli, K.-C. Chang, A. C. Mayer, P. Clancy, J. M. Blakely, R. L. Headrick, S. Iannotta, G. G. Malliaras, *Chem. Mater.* **2004**, *16*, 4497.
[32] C. Musumeci, C. Cascio, A. Scandurra, G. F. Indelli, C. Bongiorno, S. Ravesi, B. Pignataro, *Surf. Sci.* **2008**, *602*, 993.
[33] M. Ohring, *Material science of thin film*, Academic Press, San Diego, CA, **2002**.
[34] A. S. Molinari, H. Alves, Z. Chen, A. Facchetti, A. F. Morpurgo, *J. Am. Chem. Soc.* **2009**, *131*, 2462.
[35] A. Luzio, C. Musumeci, C. R. Newman, A. Facchetti, T. J. Marks, B. Pignataro, *Chem. Mater.* **2011**, *23*, 1061.
[36] E. J. Meijer, G. H. Gelinck, E. v. Veenendaal, B.-H. Huisman, D. M. d. Leeuw, T. M. Klapwijk, *Appl. Phys. Lett.* **2003**, *82*, 4576.
[37] M. L. Chabinyc, J.-P. Lu, R. A. Street, Y. Wu, P. Liu and B. S. Ong, *J. Appl. Phys.* **2004**, 96, 2063.
[38] D. J. Gundlach, J. E. Royer, S. K. Park, S. Subramanian, O. D. Jurchescu, B. H. Hamadani, A. J. Moad, R. J. Kline, L. C. Teague, O. Kirillov, C. A. Richter, J. G. Kushmerick, L. J. Richter, S. R. Parkin, T. N. Jackson, J. E. Anthony, *Nat. Mater.* **2008**, *7*, 216.
[39] F. Dinelli, M. Murgia, P. Levy, M. Cavallini, F. Biscarini, D. M. d. Leeuw, *Phys. Rev. Lett.* **2004**, *92*, 116802.
[40] F. Cicoira, C. Santato, F. Dinelli, M. Murgia, M. A. Loi, F. Biscarini, R. Zamboni, P. Heremans, M. Muccini, *Adv. Funct. Mater.* **2005**, *15*, 375.
[41] J. Rivnay, L. H. Jimison, J. E. Northrup, M. F. Toney, R. Noriega, S. Lu, T. J. Marks, A. Facchetti, A. Salleo, *Nat. Mater.* **2009**, *8*, 952.

[42] K. E. Sohn, M. D. Dimitriou, J. Genzer, D. A. Fischer, C. J. Hawker, E. J. Kramer, *Langmuir* **2009**, *25*, 6341.
[43] H. Wang, E. D. Gomez, J. Kim, Z. Guan, C. Jaye, D. A. Fischer, A. Kahn, Y.-L. Loo, *Chem. Mater.* **2011**, *23*, 2020.

Chapter 4

Role of layer morphology in photoactive polymeric blends

In this chapter we describe the effect of layer morphology on the photoactive properties of a polymeric blend. The all-polymer thin films are engineered by nanoscale control, from a vertical phase segregation (2D order) to a lateral phase separation (3D order). The results suggest high dissociation efficiency for the bounded electron-hole pairs and balanced electron and hole mobility along the thin films revealing new insights into the main factors limiting the efficiency of all-polymer solar cells.

Published as:
S. Fabiano, Z. Chen, S. Vahedi, A. Facchetti, B. Pignataro and M. A. Loi, *J. Mater. Chem.*, 2011, **21**, 5891

4.1 Introduction

Solution-processed polymer solar cells (SCs) have attracted great interest during the last few years as a promising low-cost alternative to the conventional silicon-based photovoltaic devices.[1] The fabrication of these devices by solution-processing the photoactive layer offers an important advantage to enable flexible, roll-to-roll and large-area photovoltaic technologies.[2] A breakthrough in this field originated in the engineering of ordered thin film bulk heterojunction (BHJ) solar cells composed of electron donor (D) and electron acceptor (A) semiconductors as the photoactive layer.[3] To date, the most efficient SCs are based on polymer/fullerene derivative blends[4] and the design/synthesis of new *p*-type polymers has dramatically improved the power conversion efficiencies (*PCEs*), now surpassing 7%.[5] However, due to the low extinction coefficient of the fullerene derivatives, only a limited part of the solar spectrum is generally harvested.[6] In this respect, polymer (donor)/polymer (acceptor) blends may offer several advantages compared to the polymer/fullerene ones. By tuning the absorption profile of each component, all-polymer blends may allow for covering complementary parts of the solar spectrum thus improving the final power conversion efficiency.[7] On the other hand, blending of two polymers generally results into microscopic phase separation which dramatically reduces donor-acceptor interfacial area thus reducing exciton dissociation probability. Such morphological donor and/or acceptor domains must be reduced to the size of the exciton diffusion length (ca. 5-10 nm) by nanoscale control, in order to enhance the *PCE*.[8,9]

Promising results have been reported so far for all-polymer solar cells and efficiencies approaching 2% have been demonstrated.[9-11] Unfortunately, such performances are relatively poor as compared to those of fullerene-based devices. One of the main reasons limiting the efficiency of the all-polymer SCs is the low fill factor (*FF*), typically less than 30%. Although the origin of the reduced *FF* in all-polymer SCs has not been fully clarified, it is largely attributed to a low dissociation efficiency of the bound electron-hole pairs. The low dielectric constant of polymer respect to the fullerenes, the unfavorable mixing properties of the macromolecules, as well as the low bulk carrier mobility are some of the loss mechanisms contributing to limit the *FF*. The employment of low-performing *n*-type polymers, for example, results in unbalanced bulk carrier transports where the electron mobility is far lower than the hole mobility, leading to space-charge effects.[12] Kim *et al.* have shown that the low electron mobility of poly(9,9-dioctylfluorene-*co*-benzothiadiazole) (F8BT) is mainly responsible for the reduced *FF* (ca.

36%) of the all-polymer SCs of this polymer in blend with regioregular poly(3-hexylthiophene-2,5-diyl) (P3HT), demonstrating *PCE* of 0.13%.[13] Thus, new high-mobility *n*-type polymers are needed to improve the efficiency of all-polymer SCs.

Herein, we report the realization of all-polymer solar cells based on the blend of poly{[N,N'-bis(2-octyldodecyl)-naphthalene-1,4,5,8-bis(dicarboximide)-2,6-diyl]-alt-5,5'-(2,2'-bithiophene)} (P(NDI2OD-T2))[14] as electron acceptor and P3HT as electron donor. The use of P(NDI2OD-T2) enables to reach high fill factor close to 70%, indicating large balanced electron and hole mobility. A solvent dependence of the *PCE* was observed, suggesting that the optimization of the final active layer morphology could be one of the factors limiting the efficiency.

4.2 Results and discussion

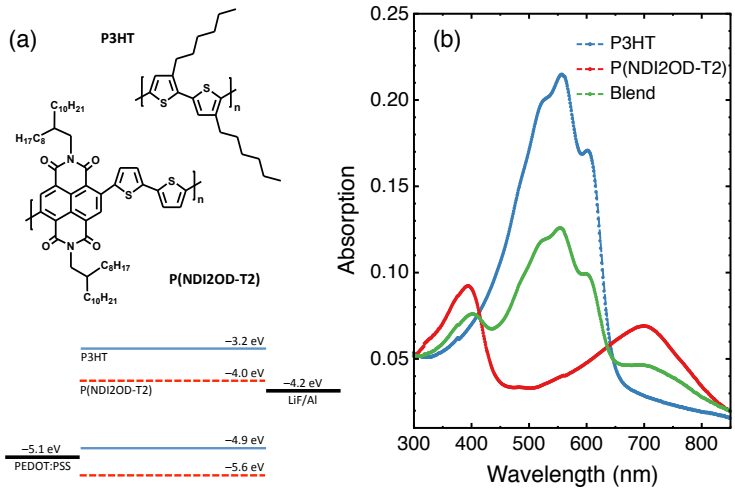

Figure 4.1 (a) Chemical structures and energy level diagram of P(NDI2OD-T2) and P3HT. (b) Absorption spectra of P3HT (blue), P(NDI2OD-T2) (red) and blend (green) thin films.

The chemical structures of regioregular P3HT and P(NDI2OD-T2), along with the relative energy level diagram and absorption spectra are shown in Figure 4.1. The HOMO and LUMO level offset of the two polymers aids in an efficient charge transfer, as was recently demonstrated by time-resolved photoluminescence measurements.[15] The LUMO levels of P3HT and P(NDI2OD-T2) are ~3.2 and 4.0 eV, respectively. A theoretical open circuit voltage (V_{oc}) of about 0.9 V is

expected, as generally expressed by the energy difference between HOMO of the donor and LUMO of the acceptor minus a loss of 0.3 eV.[16] In addition, the low band gaps of both polymers (ca. 1.7 eV for P3HT and ca. 1.6 eV for P(NDI2OD-T2)) allow to extend the light absorption of the blend up to 850 nm, covering complementary regions of the entire visible range (see Figure 4.1b). The absorption spectrum of the P3HT/P(NDI2OD-T2) blend is simply the superposition of the two polymers absorption spectra, indicating that no charge transfer occurs in the ground state.

In order to test the photovoltaic properties of the polymer-blend thin films, all devices were fabricated on PEDOT:PSS-coated indium tin oxide substrates with a conventional SCs architecture. Figure 4.2 shows the *J-V* characteristics of the P3HT/P(NDI2OD-T2) solar cells with 1:1 and 1:2 weight ratio (w/w) both from CB and *o*-DCB. An enhancement on the device photovoltaic performances is observed when the P(NDI2OD-T2) concentration in the polymer-blend is increased. However, no significant improvements were observed when the P(NDI-2OD-T2) content in the blend is increased further. The effect of the D/A weight ratio along with the influence of the solvent on the photovoltaic behaviour of the SC are summarized in Table 4.1. The observed open circuit voltage is consistent with the $HOMO_D$-$LUMO_A$ difference expected from the energy level offset of P3HT and P(NDI2OD-T2). Indeed, according to the typical energy loss in P3HT-based cells (ca. 0.35 eV),[17] the maximum predictable open circuit voltage for our devices should be ~0.55 V, which is in agreement with the experimental results.

Table 4.1 Summary of device performance parameters for the ITO/PEDOT:PSS/P3HT:P(NDI2OD-T2)/LiF/Al solar cells shown in Figure 5.2.

	J_{sc} [mA cm^{-2}]	V_{oc} [V]	FF [%]	PCE [%]
1:1 CB	0.34	0.49	54	0.09
1:2 CB	0.49	0.51	66	0.16
1:1 *o*-DCB	0.35	0.48	54	0.09
1:2 *o*-DCB	0.48	0.50	67	0.16

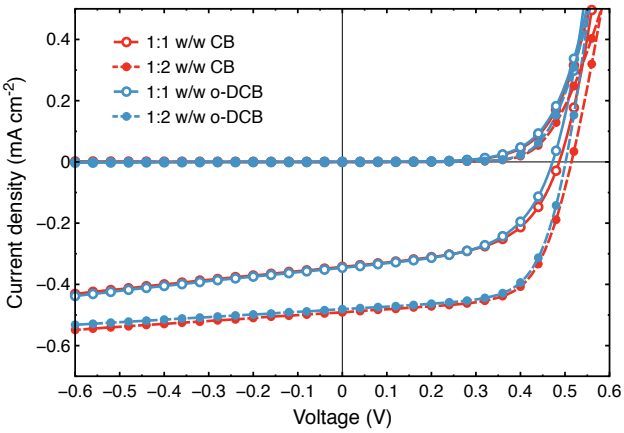

Figure 4.2 Current density-voltage (J-V) characteristics for 1:1 and 1:2 w/w P3HT/P(NDI2OD-T2) solar cells spin-coated from CB and o-DCB.

Interestingly, the fill factor values of these devices are the highest reported so far for all-polymer solar cells, suggesting high charge separation efficiency and balanced carrier mobility for P3HT/P(NDI2OD-T2) blends. In this respect, the P3HT/P(NDI2OD-T2) interface has been shown to be highly efficient for charge transfer[15] and free carrier generation in bilayer field-effect transistors (FETs).[18] Furthermore, a recent study shows that P(NDI2OD-T2) films exhibit large bulk electron mobility in a diode architecture (~5 × 10^{-3} cm^2 V^{-1} s^{-1}),[19] which is comparable to the typical bulk hole mobility for P3HT films (~2 × 10^{-3} cm^2 V^{-1} s^{-1}).[13] It has been shown also that P3HT/P(NDI2OD-T2) blends yield high balanced ambipolar mobilities (~3 ×10^{-3} cm^2 V^{-1} s^{-1}) in FET configuration.[15] Despite these favourable charge transport conditions, our devices exhibit modest short-circuit current densities (J_{sc} = 0.34 ÷ 0.49 mA cm^{-2}), resulting in low power conversion efficiencies (*PCE* = 0.09 ÷ 0.16%).

Contact-limited currents have been observed for P(NDI2OD-T2), even when low work function metals are employed.[19] We performed *J-V* measurements on devices with samarium (Sm) contacts, which has been reported being the best injecting electrode for this *n*-type polymer. No significant differences in the extracted currents were observed when Sm is employed, with *FF* values comparable to those achieved with LiF/Al.

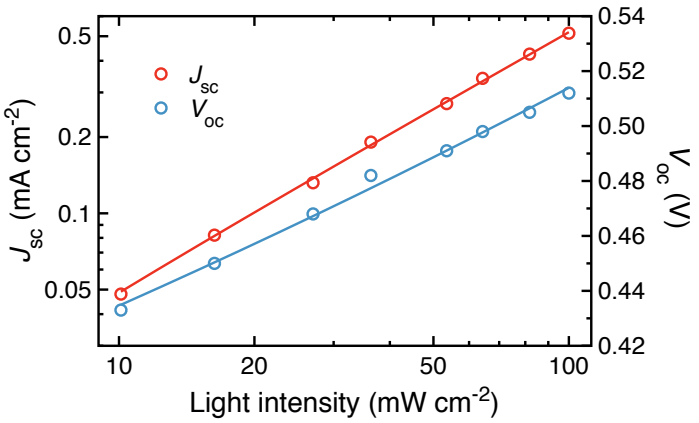

Figure 4.3 Light intensity dependence of short-circuit current density (open circle) and open circuit voltage (open triangle) for a 1:2 w/w P3HT/P(NDI2OD-T2) solar cell from CB. The relationship between J_{sc} and the light intensity is expressed as $J_{sc} \propto I^{\alpha}$.

In order to evaluate if recombination processes are limiting the device performance, light intensity dependent measurements were carried out on the most efficient devices. Since no significant photovoltaic performance differences are observed for the devices spin-coated from CB and *o*-DCB, this study was carried out on 1:2 w/w P3HT/P(NDI2OD-T2) cells spin-coated from CB. The relationship between J_{sc} and the light intensity is expressed as $J_{sc} \propto I^{\alpha}$, with α generally ranging from 0.85 to 1.[20] As shown in Figure 4.3, a linear dependence of the short-circuit current density on the light intensity (law fit to $\alpha = 1.01$) was observed. This data suggests that major charge carrier losses are due to monomolecular (exciton or geminate pair) recombination processes and not bimolecular recombination, since in the latter case a sub-linear dependence of the J_{sc} is expected.[21] Furthermore, as observed for Langevin recombination in polymer/fullerene devices, the open circuit voltage depends on the light intensity with a kT/q slope.[22] Stronger dependence has been observed for the all-polymer solar cells and explained by electron trap-assisted recombination mechanisms.[23] In our case, a dependence with a slope of 1.3 kT/q unit was observed (Figure 4.3). A similar dependence of the open circuit voltage has been reported for a graded bilayer structure of M3EH-PPV (donor polymer) and CN-ether-PPV (acceptor polymer) solar cells, for which a vertical composition gradient with the CN-ether-PPV rich phase on the top of the polymer-blend films has been proposed.[11]

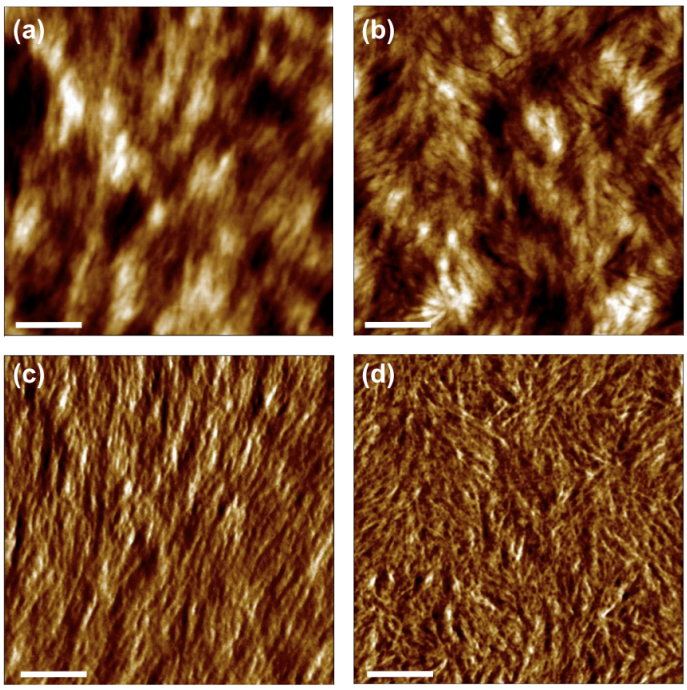

Figure 4.4 SFM topography (a, b) and phase-lag (c, d) images of 1:2 w/w P3HT/P(NDI2OD-T2) thin films from CB (a, c) and o-DCB (b, d). All scale bars are 200 nm.

To evaluate the role of the blend morphology, the topography of the thin films was investigated by scanning force microscopy (SFM). The tendency of the polymer-polymer blends to phase-separate is generally ascribed to a low entropy of mixing and governed by a spinodal decomposition of the blend.[24] Figure 4.4 refers to 1:2 w/w P3HT/P(NDI2OD-T2) polymer-blend films spin-coated from CB (a, c) and *o*-DCB (b, d). In particular, a fiber-like structure of the surfaces is visible both in topography (a, b) and in phase-lag (c, d) images. The rms roughness at 1 × 1 μm is equal to 1.73 nm for the thin films from CB and 1.65 nm for those from *o*-DCB with a features size of the order of 10-35 nm. Such a morphology has been already observed for the pristine P(NDI2OD-T2)[14] and justified by a face-on molecular packing with a high in-plane order.[25]

Vertically phase-separated structures have been observed for several spin-coated polymer blends caused by a solvent-concentration gradient through the films.[11,13] Regarding surface energy, it is widely known that interfacial energy differences may affect preferential segregation. Accordingly, from the measured contatc angles of P3HT and P(NDI2OD-T2), surface energies were estimated as 27.8 and 23.7

mJ m^{-2}, respectively. Such a difference may thermodynamically drive the polymer-blend phase separation, as generally observed for polymer-fullerene systems as well.[26] By a modulation of the interfacial tensions at the polymer-polymer interface, it is possible to modify the final morphology of such thin films, from self-stratified to laterally phase-separated nanostructures.[27] Indeed, since the typical exciton diffusion length for the organic semiconductors is of the order of ca. 5-7 nm,[28] in a bilayer structure only a narrow layer near to the planar heterojunction is involved in the photovoltaic process, strongly limiting the devices performance.[29] Recently, inverted bilayer solar cells of P3HT and P(NDI2OD-T2) have been realized by soft-contact lamination of the two polymers, showing $FF > 55\%$ but only very moderate J_{sc} (0.069 ÷ 0.082 mA cm^{-2}).[30] Moreover, the balanced electron and hole mobility described above for field-effect transistors measurements on P3HT/P(NDI2OD-T2) blends may be justified by the formation of horizontally phase separated pathways for both polymers between the TFT electrods.[15,31]

Accordingly, in order to improve the lateral phase separation of the P3HT/P(NDI2OD-T2) blend, xylene was used as solvent. It is well-know that the P3HT self-organizes in crystalline aggregates with enhanced hole mobility when spin-coated from poor solvents such as xylene.[32] In this solvent, the self-assembly of the P3HT occurs readily in solution, leading to whisker-like nanostructures that increase the bulk D/A interface along the thin films with the formation of percolation pathways useful for the charge transport.[33,34] An improvement for example in the short-circuit current by a factor of 10 has been observed when P3HT nanofibers are incorporated into the blends with polyfluorene copolymers (*i.e.* F8BT), as compared to the as-cast blends without fibers.[33] The SFM topography (a, c) along with the phase-lag (b, d) images relative to the 1:1 (a, b) and the 1:2 (c, d) w/w P3HT/P(NDI2OD-T2) polymer-blend films are shown in Figure 4.5. Laterally phase-separated nanostructures are visible in both topography and phase-lag images. In particular, the 1:1 w/w ratio shows domains of the order of 180-230 nm as well as a finer phase separation (less than 20 nm). Fibers wide 50-90 nm are evident instead for the 1:2 w/w blend. The rms roughness at 1 × 1 μm is about 2.80 and 2.11 nm for the 1:1 and 1:2 w/w P3HT/P(NDI2OD-T2), respectively.

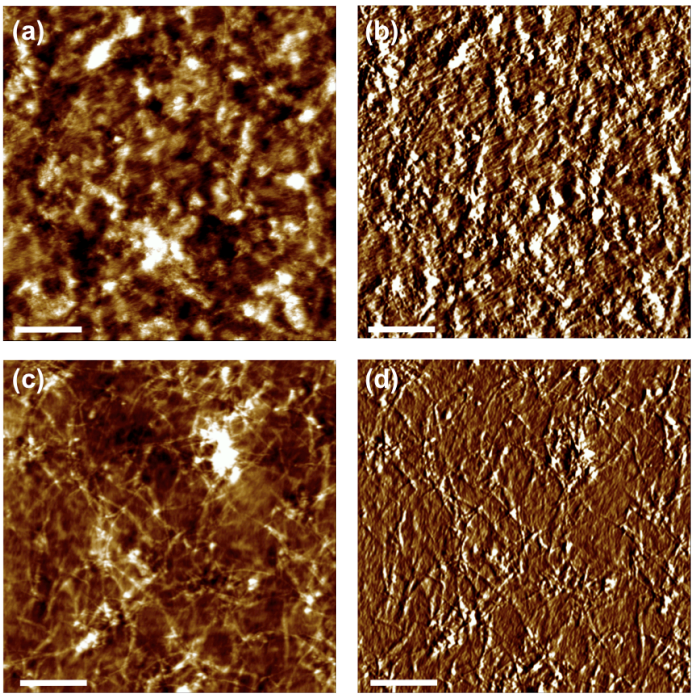

Figure 4.5 SFM topography (a, c) and phase-lag (b, d) images of 1:1 (a, b) and 1:2 (c, d) w/w P3HT/P(NDI2OD-T2) thin films spin-coated from xylene. All scale bars are 1 μm.

The resulting *J-V* characteristic of the xylene-processed solar cell is shown in Figure 4.6. A short-circuit current density of 1.02 mA cm^{-2} was observed for the 1:1 w/w devices. Such a J_{sc} is at least two 2-3x higher than the best results obtained from CB and *o*-DCB for the same weight ratio (ca. 0.35 mA cm^{-2}) and for the 1:2 w/w (ca. 0.49 mA/cm^2). This result is consistent with a more efficient lateral phase separation with respect to a self-stratified one as shown by the AFM analysis. Moreover, the current density increases to 2.39 mA/cm^2 for the devices with D/A weigh ratio of 1:2. However, a reduction of the current was observed with a further increase of the P(NDI2OD-T2) content. The V_{oc} values did not differ from those observed for CB and *o*-DCB were 0.49 V and 0.48 V for 1:1 and 1:2 w/w, respectively. The *FF* decreases from 60 to 54% with the increase of the acceptor content in the blend. Although these *FF* are higher when compared to those of other all-polymer SCs, the lowest values are consistent with an increased series resistance deriving from the formation of isolated laterally phase-separated domains.[35] The resulting *PCE* increases from 0.28% for the 1:1 w/w to 0.62% for the 1:2 w/w D/A blends.

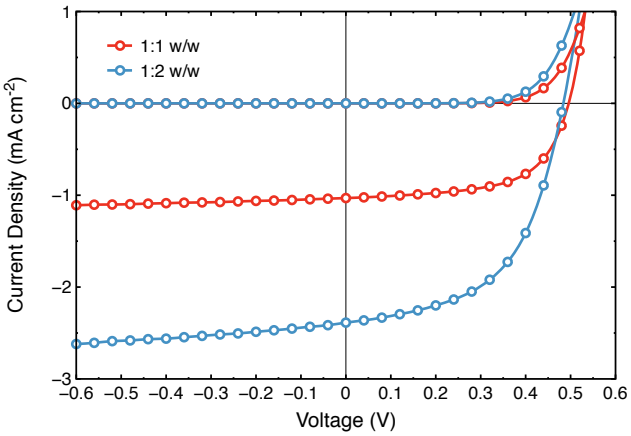

Figure 4.6 J-V characteristics for 1:1 and 1:2 w/w P3HT/P(NDI2OD-T2) solar cells from xylene.

Figure 4.7 shows the incident-photon-to-converted-electron efficiency (*IPCE*) relative to the devices reported in figure 4.6. The maximum *IPCE* was found to be ca. 8.5% and 15.8% at 520 nm for 1:1 and 1:2 w/w cells, respectively. This wavelength is close to the maximum absorption of P3HT (~550 nm). In addition, a shoulder at ca. 600 nm is visible in both the *IPCE* spectra, consisting with the self-assembling in the solid state of the P3HT polymer chains.[36] For wavelengths larger than 650 nm, the *IPCE* spectra are dominated by the absorption of P(NDI-2OD-T2) having a maximum at ca. 700 nm and indicating that a non-negligible portion of the excitons is generated in the acceptor domains. The *IPCE* analysis shows that it is possible therefore to extend the photon absorption and the relative electron conversion up to 850 nm, by using P(NDI2OD-T2) as acceptor.

It should be noted that the optimal blend ratio is different from that commonly used in polymer-fullerene systems.[37] The dependence of the photovoltaic performance on the weight ratio of P3HT/P(NDI2OD-T2) could be explained in terms of absorption and phase separation in the polymer-blend films. The increase in J_{sc} and *PCE* with the P(NDI2OD-T2) content in the blend indeed can be mainly ascribed to the extended photon absorption. Further increasing the P(NDI2OD-T2) concentration may lead to large demixing in the polymer blend, which negatively affects the electron transport.

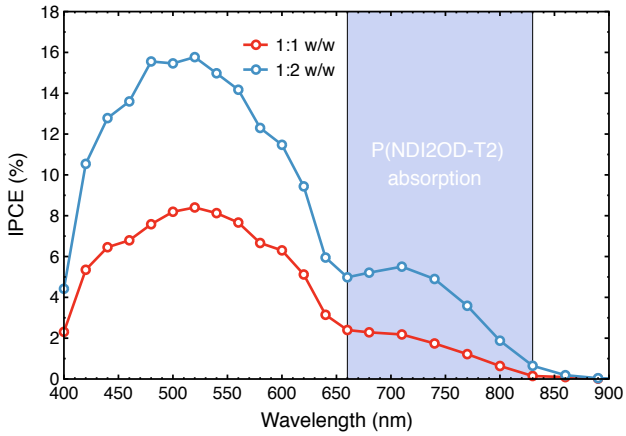

Figure 4.7 J-V characteristics for 1:1 and 1:2 w/w P3HT/P(NDI2OD-T2) solar cells from xylene.

4.3 Conclusions

We have studied the photovoltaic properties of the P(NDI2OD-T2) in blend with the P3HT. High fill factor all-polymer solar cells have been demonstrated for the first time with values of nearly 70%, suggesting highly balanced mobility into the polymer-blend thin films. Thus, using high mobility electron-transporting polymers such as P(NDI2OD-T2) enables *FF* values comparable with those reported for fullerene-based devices. However, the photoactive blend morphology hinders to reach high efficiencies, thus further optimizations are necessary to improve the photoactive layer charge transport. Although we cannot state that poor phase separation is the only cause for the low efficiencies, using for instance additive molecules may lead to a better morphology, as already demonstrated for polymer-fullerene systems. In addition, the electronic structure of the blend could play an important role on the ultimate efficiency. Adjusting the D and A HOMO and LUMO levels by combining P(NDI2OD-T2) with new high-performing *p*-type polymers would allow to minimize the energy loss due to the LUMOs offset.

4.4 Experimental details

Materials and device fabrication

The poly{[N,N'-bis(2-octyldodecyl)-naphthalene-1,4,5,8-bis(dicarboximide)-2,6-diyl]-alt-5,5'-(2,2'-bithiophene)} (P(NDI2OD-T2), ActivInk N2200) was obtained

from Polyera Corporation, USA. A batch with a molecular weight of ~250 kDa and a PDI of ~5 was used. The P(NDI2OD-T2) was blended with regioregular poly(3-hexylthiophene-2,5-diyl) (P3HT) purchased from Rieke Metals with regioregularity > 98% and average molecular weight < 50 kDa.

The photovoltaic property of the blend was studied in the device structure composed by ITO/PEDOT:PSS/polymer blend/LiF/Al. Indium tin oxide (ITO)-coated glass substrates were cleaned stepwise in soap, demineralized water, acetone and isopropanol under ultrasonication for 5 min each and subsequently dried in the oven at 140 °C for 10 min. The substrates were then treated by ultraviolet ozone plasma for 20 min. A thin layer (~50 nm) of PEDOT:PSS (Clevios P VP AI 4083) was spin-coated onto the cleaned ITO substrates and annealed in oven at 140 °C for 10 min. The substrates were transferred in a nitrogen-filled glovebox (< 0.1 ppm O_2 and H_2O) for the active layer coating and electrode deposition. The polymer blends, having different donor-acceptor weight ratios, were spin-coated on the PEDOT:PSS-coated substrates with an active layer thickness of 80-110 nm from chlorobenzene (CB), *o*-dichlorobenzene (*o*-DCB) and xylene solutions after filtration with a 0.45 μm PTFE syringe filter. Variations of few tens of nanometers in the active layer thickness were not observed influencing significantly the devices performance. The films thickness was measured by using a DekTak II profilometer. Metal contacts were fabricated by thermal evaporation at a pressure < 10^{-6} mbar with a device area of 4 mm^2, as defined by a shadow mask.

Characterization methods

Current-voltage characteristics were carried out inside the glovebox by using a Keithley 2400 source/measure unit under AM 1.5G illumination at 100 mW/cm^2. The incident-photon-to-converted-current efficiency (*IPCE*) was measured using a lock-in amplifier (SR830, Stanford Research Systems) coupled with a monochromator and a xenon lamp under short-circuit condition.

Absorption measurements were performed on freshly prepared thin films by using a Perkin Elmer Lambda 900 spectrometer.

The morphology of the active layers has been inspected by scanning force microscopy (SFM) in air using a Multimode Nanoscope IV (Digital Instruments, Santa Barbara, CA) working in tapping mode. Etched-silicon probes with a pyramidal-shape tip having a nominal curvature of 10 nm and a nominal internal angle of 35° were used. The height and phase-lag images were collected by capturing 512 × 512 points with a scan rate below 1 line per second at a tip resonance frequency of 330 kHz.

Contact angle measurements were carried out at room temperature by using deionized water, tritoyl phosphate and glycerol as test liquids.[[38]] The surface energy was calculated by fitting the measured values of contact angles with the following equation:

$$\gamma_l(1+\cos\theta) = 2\left[\left(\gamma_s^{lw}\gamma_l^{lw}\right)^{1/2} + \left(\gamma_s^{+}\gamma_l^{-}\right)^{1/2} + \left(\gamma_s^{-}\gamma_l^{+}\right)^{1/2}\right]$$

where γ_l and γ_s are the liquid and solid tensions, γ^+ and γ^- are the acid and base components of the surface tension and γ^{lw} is attributed to the Lifshitz-van der Waals interactions.

References

[1] N. S. Lewis, *Science* **2007**, *315*, 798-801; A. C. Mayer, S. R. Scully, B. E. Hardin, M. W. Rowell, M. D. McGehee, *Mater. Today* **2007**, *10*, 28-33.
[2] F. C. Krebs, *Sol. Energy Mater. Sol. Cells* **2009**, *93*, 394-412.
[3] J. J. M. Halls, C. A. Walsh, N. C. Greenham, E. A. Marseglia, R. H. Friend, S. C. Moratti, A. B. Holmes, *Nature* **1995**, *376*, 498-500; G. Yu, J. Gao, J. C. Hummelen, F. Wudl, A. J. Heeger, *Science* **1995**, *270*, 1789-1791.
[4] B. C. Thompson, J. M. J. Fréchet, *Angew. Chem. Int. Ed.* **2008**, *47*, 58-77.
[5] H.-Y. Chen, J. Hou, S. Zhang, Y. Liang, G. Yang, Y. Yang, L. Yu, Y. Wu, G. Li, *Nat. Photonics* **2009**, *3*, 649-653.
[6] T. J. Savenije, J. E. Kroeze, X. Yang, J. Loos, *Adv. Funct. Mater.* **2005**, *15*, 1260-1266.
[7] G. Sang, E. Zhou, Y. Huang, Y. Zou, G. Zhao, Y. Li, *J. Phys. Chem. C* **2009**, *113*, 5879-5885; G. Sang, Y. Zou, Y. Huang, G. Zhao, Y. Yang, Y. Li, *App. Phys. Lett.* **2009**, *94*, 193302.
[8] C. R. McNeill, S. Westenhoff, C. Groves, R. H. Friend, N. C. Greenham, *J. Phys. Chem. C* **2007**, *111*, 19153-19160; S. Fabiano, B. Pignataro, *Phys. Chem. Chem. Phys.* **2010**, *12*, 14848-14860.
[9] S. Cataldo, S. Fabiano, F. Ferrante, F. Previti, S. Patanè, B. Pignataro, *Macromol. Rapid Commun.* **2010**, *31*, 1281-1286.
[10] C. R. McNeill, A. Abrusci, J. Zaumseil, R. Wilson, M. J. McKiernan, J. H. Burroughes, J. J. M. Halls, N. C. Greenham, R. H. Friend, *App. Phys. Lett.* **2007**, *90*, 193506; T. W. Holcombe, C. H. Woo, D. F. J. Kavulak, B. C. Thompson, J. M. J. Frèchet, *J. Am. Chem. Soc.* **2009**, *131*, 14160-14161.
[11] T. Kietzke, H.-H. Hörhold, D. Neher, *Chem. Mater.* **2005**, *17*, 6532-6537.
[12] V. D. Mihailetchi, J. Wildeman, P. W. M. Blom, *Phys. Rev. Lett.* **2005**, *94*, 126602.
[13] Y. Kim, S. Cook, S. A. Choulis, J. Nelson, J. R. Durrant, D. D. C. Bradley, *Chem. Mater.* **2004**, *16*, 4812-4818.
[14] H. Yan, Z. Chen, Y. Zheng, C. Newman, J. R. Quinn, F. Dötz, M. Kastler, A. Facchetti, *Nature* **2009**, *457*, 679-686.
[15] K. Szendrei, D. Jarzab, Z. Chen, A. Facchetti, M. A. Loi, *J. Mater. Chem.* **2010**, *20*, 1317-1321.
[16] C. J. Brabec, A. Cravino, D. Meissner, N. S. Sariciftci, T. Fromherz, M. T. Rispens, L. Sanchez, J. C. Hummelen, *Adv. Funct. Mater.* **2001**, *11*, 374-380; D. Veldman, S. C. J. Meskers, R. A. J. Janssen, *Adv. Funct. Mater.* **2009**, *19*, 1939-1948.
[17] A. Cravino, *App. Phys. Lett.* **2007**, *91*, 243502.

[18] M. Rao, R. P. Ortiz, A. Facchetti, T. J. Marks, K. S. Narayan, *J. Phys. Chem. C* **2010**, *114*, 20609.
[19] R. Steyrleuthner, M. Schubert, F. Jaiser, J. C. Blakesley, Z. Chen, A. Facchetti, D. Neher, *Adv. Mater.* **2010**, *22*, 2799-2803.
[20] L. J. A. Koster, V. D. Mihailetchi, H. Xie, P. W. M. Blom, *Appl. Phys. Lett.* **2005**, *87*, 203502.
[21] J. Nelson, *Phys. Rev. B* **2003**, *67*, 155209.
[22] L. J. A. Koster, V. D. Mihailetchi, R. Ramaker, P. W. M. Blom, *Appl. Phys. Lett.* **2005**, *86*.
[23] M. M. Mandoc, W. Veurman, L. J. A. Koster, B. d. Boer, P. W. M. Blom, *Adv. Funct. Mater.* **2007**, *17*, 2167-2173.
[24] R. A. L. Jones, *Phys. World* **1995**, *8*, 47.
[25] J. Rivnay, M. F. Toney, Y. Zheng, I. V. Kauvar, Z. Chen, V. Wagner, A. Facchetti, A. Salleo, *Adv. Mater.* **2010**, *22*, 4359-4363.
[26] M. Campoy-Quiles, T. Ferenczi, T. Agostinelli, P. G. Etchegoin, Y. Kim, T. D. Anthopoulos, P. N. Stavrinou, D. D. C. Bradley, J. Nelson, *Nat. Mater.* **2008**, *7*, 158.
[27] S. Y. Heriot, R. A. L. Jones, *Nat. Mater.* **2005**, *4*, 782-786.
[28] O. V. Mikhnenko, F. Cordella, A. B. Sieval, J. C. Hummelen, P. W. M. Blom, M. A. Loi, *J. Phys. Chem. B* **2008**, *112*, 11601-11604.
[29] C. J. Brabec, N. S. Sariciftci, J. C. Hummelen, *Adv. Funct. Mater.* **2001**, *11*, 15-26.
[30] J. B. Kim, S. Lee, M. F. Toney, Z. Chen, A. Facchetti, Y. S. Kimand, Y.-L. Loo, *Chem. Mater.* **2010**, *22*, 4931-4938.
[31] F. Dinelli, R. Capelli, M. A. Loi, M. Murgia, M. Muccini, A. Facchetti, T. J. Marks, *Adv. Mater.* **2006**, *18*, 1416-1420.
[32] M. Mas-Torrent, D. d. Boer, M. Durkut, P. Hadley, A. P. H. J. Schenning, *Nanotechnology* **2004**, *15*, S265-S269.
[33] T. Salim, S. Sun, L. H. Wong, L. Xi, Y. L. Foo, Y. M. Lam, *J. Phys. Chem. C* **2010**, *114*, 9459-9468.
[34] S. Bertho, W. D. Oosterbaan, V. Vrindts, J. D'Haen, T. J. Cleij, L. Lutsen, J. Manca, D. Vanderzande, *Org. Electron.* **2009**, *10*, 1248-1251.
[35] J. D. Servaites, S. Yeganeh, T. J. Marks, M. A. Ratner, *Adv. Funct. Mater.* **2010**, *20*, 97-104.
[36] M. M. Erwin, J. McBride, A. V. Kadavanich, S. J. Rosenthal, *Thin Solid Films* **2002**, *409*, 198-205.
[37] A. C. Mayer, M. F. Toney, S. R. Scully, J. Rivnay, C. J. Brabec, M. Scharber, M. Koppe, M. Heeney, I. McCulloch, M. D. McGehee, *Adv. Funct. Mater.* **2009**, *19*, 1173–1179.
[38] B. Pignataro, G. Grasso, L. Renna, G. Marletta, *Surf. Interface Anal.* **2002**, *33*, 54–58.

Chapter 5

Engineering 3D ordered polymeric films by composition optimization

In this chapter we report on the engineering of 3D ordered polymeric thin films by composition ratio optimization of an all-polymer blend. The morphology is modulated to give a high percentage of domains (5-20 nm in size) allowing for exciton separation.

Published as:
S. Cataldo, S. Fabiano, F. Ferrante, F. Previti, S. Patanè and B. Pignataro, *Macromol. Rapid Commun.*, 2010, **31**, 1281

5.1 Introduction

As argued in the previous chapter, a promising approach to produce cheap, commercially affordable solar cells is to use organic materials, like conjugated polymers. The ease of processing, their flexibility and light weight, and the possibility of chemically tailoring the materials, are excellent premises for producing large area photovoltaic devices. In this respect, the use of conjugated polymers as electron acceptors gives an alternative strategy to polymer-fullerene solar cells because this would increase the exciton generation through an increased light absorption in the all-polymeric blend.[1] On the other hand, the morphology of these systems may be easily modulated to minimize the isolated donor and/or acceptor microdomains leading to a further improvement in energy conversion efficiencies.[2] Indeed, spinning a solution of a single polymer generally produces unstructured thin films, but if a mixture of polymers is used the two polymers will usually phase separate. This phase separation is a complex non-equilibrium process and the resulting film morphologies are very sensitive to a wide range of factors including features of the individual polymers, used solvent and precise spin-coating conditions.[3] Phase separation can take place in the direction perpendicular to the plane of the film, or alternatively in the plane of the film, resulting in self-stratified or laterally patterned structures with characteristic length scales, respectively.[4] The evaporation rate and viscosity of the solution can be used for instance to vary the direction of such a phase separation.

New polymers and polymers combinations are also needed to adjust the donor and acceptor HOMO and LUMO levels as well as to minimize the energy loss during the excitons dissociation. On this respect, boranes are inherently electron poor systems due to the boron vacant p_z orbitals and thus they can be used as strong electron acceptors.[5] Molecules with three-coordinate boron groups have already shown PV effect.[6] Actually these may have a significant electronic delocalization when conjugated with adjacent organic systems within a polymer scaffold,[7-9] but in spite of this only few papers have been devoted to the application of such class of polymers to organic light emitting devices.[10, 11]

In this chapter, we report on the engineering of 3D ordered polymeric thin films and application of three-coordinate organoboron polymers as *n*-type material in a flexible bulk heterojunction solar cells (SCs). Poly[(1,4-divinylenephenylene) (2,4,6-triisopropylphenylborane)] (PDB) has been blended with P3HT to form a thin film bulk heterojunction (BHJ) on PET/ITO substrates. Morphology may be modulated by composition optimization, to give a high percentage of domains (5-

20 nm in size) allowing exciton separation. The photoelectric properties of the BHJs in devices with aluminium back electrodes were imaged by light beam induced current (LBIC) and light beam induced voltage (LBIV) techniques. Open circuit voltages, short circuit currents and overall external quantum efficiencies obtained are among the highest reported for all-polymer SC cells.

5.2 Results and discussion

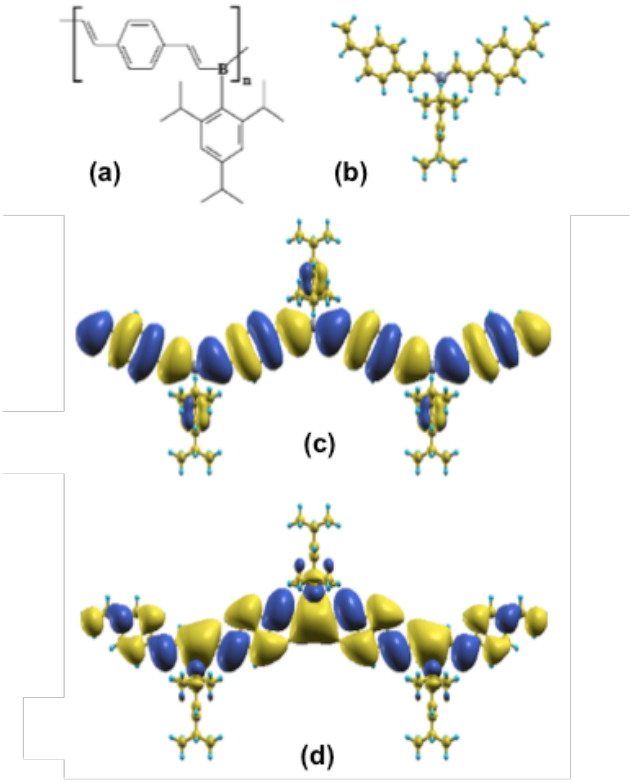

Figure 5.1. Structural unit of the PDB (a), augmented structural unit of the most stable isomer (b), the calculated HOMO (c) and LUMO (d) of the augmented trimer.‡

TDDFT calculations were performed at first on the polymer structural unit augmented by a 1,4-vinylenephenylene moiety (see Figure 5.1b). The first singlet–singlet excitation is predicted to have a transition energy of 2.88 eV (430 nm). It

would give rise to a very weak absorption (oscillator strength, f = 0.0002) which can be described as an electron redistribution from a π molecular orbital (MO) (actually Kohn–Sham orbital) localized on the tripyl benzene to a π MO of the main chain. This involves an extended conjugation through the $2p_z$ vacant orbital of the boron atom.[11] At higher energies (3.03 eV, 408 nm, f = 0.77 and 3.10 eV, 400 nm, f = 0.51), two singlet-singlet excitations are observed; they can be attributed to the combined transitions HOMO-2 → LUMO and HOMO → LUMO. In order to investigate the effect of incipient polymerization, a molecule composed by three monomers plus a 1,4-divinylenephenylene unit (see Figure 5.1c-d) has been studied. In this case singlet–singlet excitations are very different: a unique strong absorption (f = 2.843) arising from the HOMO → LUMO transition is predicted at 472 nm (2.62 eV). Thus because of the polymerization the π MOs polymer chain delocalized transitions would become dominant. The red-shift following polymerization is in agreement with the results reported by Nagai *et al.*[8] who also pointed out that the convergence of the π-conjugation length is achieved already by the trimeric structure. Experimentally, UV-vis and fluorescence data of PDB show ΔE_{0-0} = 2.79 eV (see Figure 5.2).

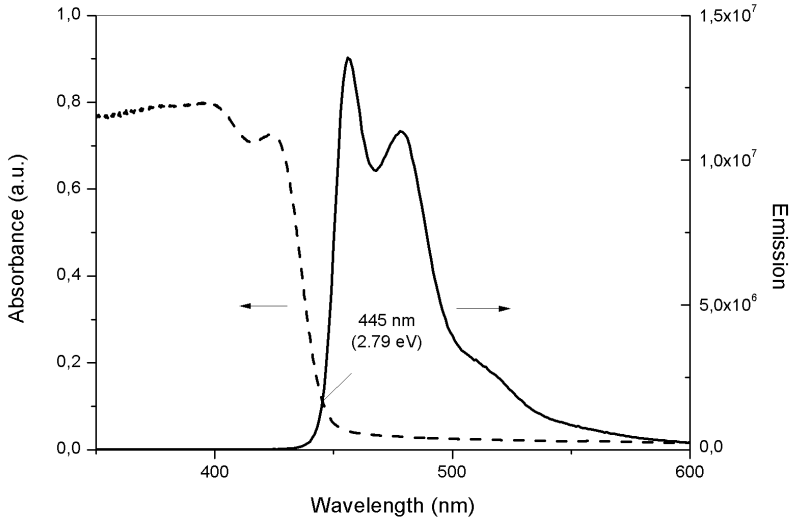

Figure 5.2. Absorption (---) and emission (—) spectra of the PDB in $CHCl_3$.

‡ Molecular orbital's representations have been realized by using the XcrysDen package.

By considering the above TDDFT and UV-vis results together with the already reported literature data,[12, 13] we depicted the energy level diagram shown below in Figure 5.3. Accordingly, the chosen combination foresees the following advantages: (1) high theoretical open circuit voltage (V_{oc}) of 1.35 V as expressed by the energy gap between $LUMO_A$-$HOMO_D$;[14] (2) optimal energy gap between $LUMO_D$-$LUMO_A$ for an efficient charge separation (ca. 0.35 eV) with a minimal energy loss[15] and (3) high extinction coefficient of PDB in the lowest wavelength region of the visible spectrum [UV (PDB): $\lambda_{max}(\varepsilon)$ = 400 nm (ca. 9000 L mol^{-1} cm^{-1})], thus extending the solar harvesting of P3HT.

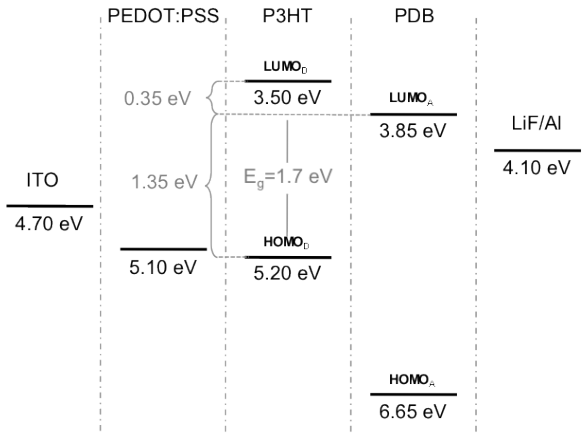

Figure 5.3. Band offset diagram for the complete PV device; the continuous lines indicate the interfaces between layers while the dashed line indicates the inner interfaces of the BHJ film.

Similarly, this polymer combination gives good mixing properties leading to optimal D/A phase separation. Figure 5.4a-c relate to SFM analysis of a 1:1 weight ratio (w/w) P3HT:PDB thin film BHJs. In Figure 5.4a the height image shows a morphology characterized by circular domains with diameters ranging from 10 to 150 nm. The fine mixing between the two polymers may be observed by the bright/dark contrast in the phase-lag image of Figure 5.4b. In particular, domains with a size of the order of a few tens of nanometres (10-30 nm) are shown in Figure 5.4c. Phase separation might be ascribed to the typically low entropy mixing of a polymeric blend.[16] By changing the P3HT:PDB composition ratio, it can be observed that phase-lag images are sensitive towards phase segregation. The dark domains would correspond to PDB rich phases while bright regions would be related to P3HT rich phases. Phase separation of the blend remained stable in time as confirmed by measurements performed after several weeks from prepa-

ration. Figure 5.4d reports the film domains diameters distribution and shows that only about 30% of the domains dimensions are in size within the exciton diffusion length (10-25 nm). Such a percentage plays a key role in the overall blend performances, and it may be increased by composition ratio optimization. In particular, an increase of domains percentage relevant to excitonic separation (5-20 nm) can be obtained by reducing the amount of PDB in the blend, as shown by phase-lag analysis reported in Figure 5.5, which allows to discriminate area of thin film with distinct chemical properties by different tip-surface interaction forces.

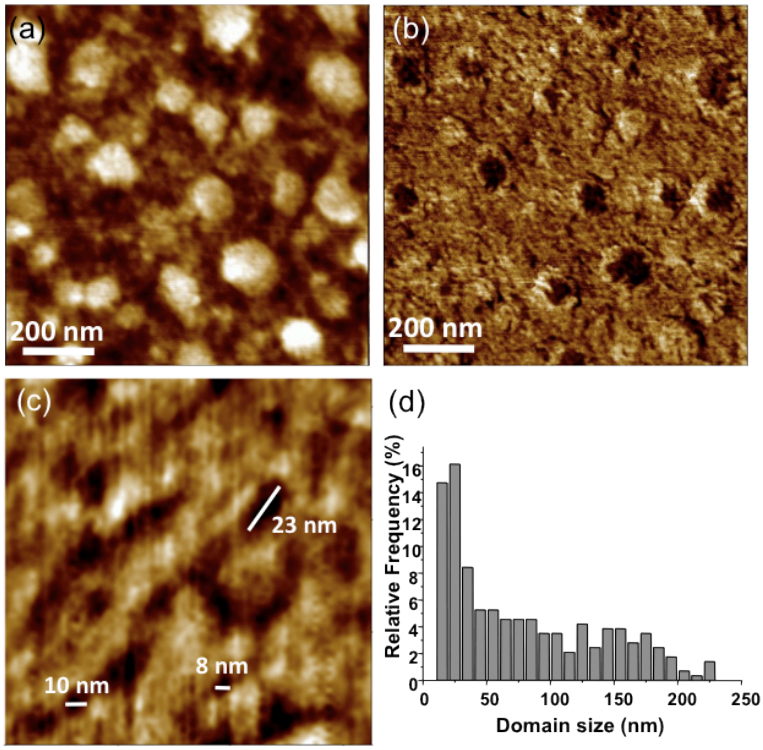

Figure 5.4. SFM topography (a) and phase-lag (b and c) images of 1:1 w/w P3HT:PDB thin film with relative domains size distribution (d).

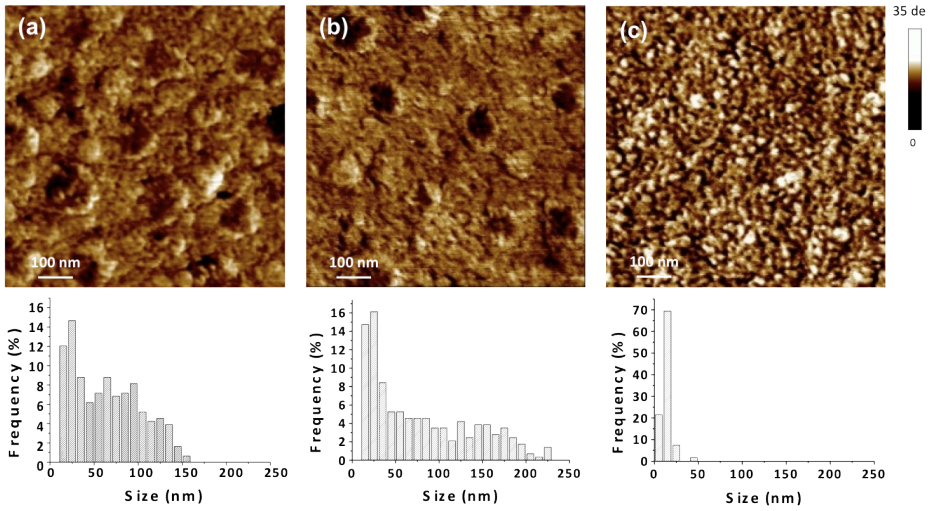

Figure 5.5. SFM phase-lag images of 1:4 (a), 1:1 (b) and 4:1 w/w (c) P3HT:PDB thin film with relative domains size distributions.

Figure 5.6 reports UV-vis spectrum of pure P3HT thin film compared with those obtained from 4:1, 1:1 and 1:4 w/w P3HT:PDB BHJ polymeric blends. UV-vis spectra demonstrated that the absorption of the P3HT:PDB blend is simply the overlap of the polymers absorption spectra indicating that no charge transfer occurs in the ground state, i.e. the difference in electro-negativity of the materials does not allow for charge transfer.[17]

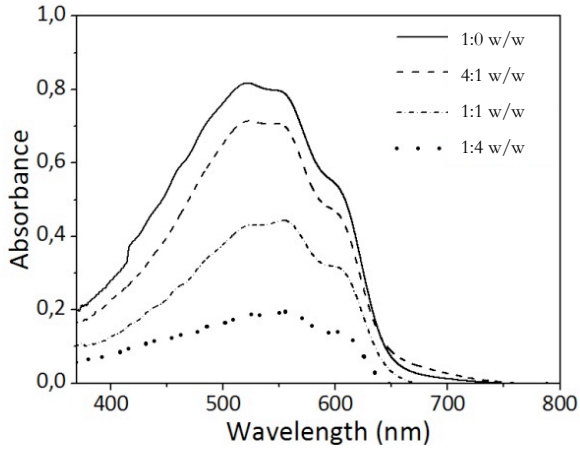

Figure 5.6. Absorption spectra of P3HT (—) and P3HT:PDB (---) blend thin films.

The photoelectric properties of the blend thin films were measured on a PV cell with standard architecture PET/ITO/PEDOT:PSS/P3HT:PDB/LiF/Al. Figure 5.7a reports current versus wavelength spectrum obtained by irradiating the device at 2.7 mW cm^{-2}. As expected this curve mainly resembles the convolution of the irradiating source and the P3HT absorption spectra. The image in Figure 5.7b shows the voltage distribution of the back electrode and interestingly it appears quite homogeneous. A similar behaviour has been found by detecting current images of the back electrode. Such findings demonstrate the quality of the polymer blend whose composition is well suited for electrons and holes percolation along the film thickness.

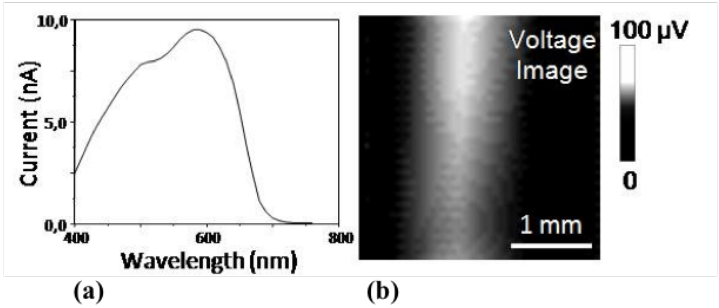

Figure 5.7. LBIC current versus wavelength spectrum (a) and LBIV voltage image (b) of PET/ITO/PEDOT:PSS/P3HT:PDB/LiF/Al devices irradiated at 2.7mW cm^{-2}.

Photocurrent and photovoltage measurements have been performed by using an incident radiance in the wide range of 2.7-320 mW cm^{-2}. The short circuit current density (J_{sc}), ranging from 0.04 to 18 mA cm^{-2}, gives a value of about 6 mA cm^{-2} at about 100 mW cm^{-2}. A 1:1 relationship between the increasing of J_{sc} and the incident power has been already demonstrated for other all-polymer PV cells.[18]

In the best case the cell (P3HT:PDB, 1:1 w/w) irradiated at 320 mW cm^{-2}, gave an open circuit voltages (V_{oc}) of about 1 V and J_{sc} of about 18 mA cm^{-2}. The average external quantum efficiency (*EQE*) was of about 12%. Usually fill factor larger than 30% has been obtained. By considering the correlation between the above parameters and the incident power in organic PV cells,[19] these values are very promising. Indeed, in a recent paper dealing with PV cells of tris(thienylenevinylene) substituted polythiophene and poly[perylenediimide-alt-bis(dithienothiophene)], it was reported the best J_{sc} for all-polymer PV cells of 5.02 mA cm^{-2} along with V_{oc} of 0.69 V and an average *EQE* of about 20% when irradiated at

100 mW cm^{-2} by an AM 1.5G solar simulator.[20] By inspecting such devices, direct correlations with film thickness and components concentration have been found. Our experiments showed that, in spite of the more suitable domain sizes for exciton separation (5-20 nm)[21] revealed by AFM for the P3HT:PDB 4:1, 1:1 w/w BHJs works quite better. This can be explained by considering that a compromise is needed between the lateral size of D and A domains and their vertical morphological continuity along the thin film. Accordingly, 1:1 w/w BHJs would offer a larger number of pathways which help electrons and holes percolations towards the electrodes. The presence of laterally large domains, with respect to the exciton diffusion length, would aid electron-hole recombination, thus reducing the yield of exciton separation. Similarly, film thickness was a crucial factor in determining the charge transport. BHJs thicker than 100 nm showed lower J_{sc} values, although V_{oc} was usually higher than 0.4 V. This agrees with a picture in which series resistance is enlarged by film thickness. This can be due to a reduced dimension of the continuous pathways for charge transport and the increasing of the probability of free charge carriers recombination. As to the PDB stability, it has to be noted that after ageing for several months in air polymer degradation may occur. The degradation is outlined by the disappearance of the 397 and 423 nm peaks in the UV–Vis spectra and the simultaneous increase of the peak at 251 nm. Accordingly to literature, this effect might be ascribed to the formation of monomeric units.[7] The realization of BHJ cells by using the degraded polymer results in lower J_{sc} values (up to 1 order of magnitude), V_{oc} values of 0.4 V and fill factor of 26%. By envisioning possible applications, the device performance loss is of course to be avoided. Studies on suitable polymer storing and device packaging procedures are needed.

5.3 Conclusions

Three-coordinate organoboron polymers are very promising electron acceptors for the realization of high efficiency all-polymer PV cells. The use of long chain systems including vacant p_z orbitals along with p-conjugated units could be an excellent strategy to harvest and to convert the solar spectrum in combination with low band gap donor polymers. In this communication we showed the development of flexible organoboron polymers based PV cells and important technological issues concerning the device optimization as well as the device packaging will be the object of future work.

5.4 Experimental details

Materials and sample preparation

We applied n-type organoboron polymers to PV by using poly[(1,4-divinylenephenylene)(2,4,6-triisopropylphenylborane)] (PDB, Mn = 1379, Mw = 2646, Aldrich; Figure 5.1a)[12] blended with P3HT (regioregular, electronic grade, 99.995%; Aldrich), that works as a D polymer. Considering that the repetitive unit of PDB has a molecular weight of 342.33 Da, a polymerization degree of 4 has been evaluated. Note that in a recent paper, Chujo and coworkers[8] showed that the polymer band gap does not significantly change if the polymerization degree is larger than 3. The BHJ films were deposited by spin-coating at 1000 rpm for 5 s, from 10 mg mL^{-1} chloroform P3HT:PDB solutions with ratios of 80:20, 50:50 and 20:80 wt.-% leading to film thickness ranging from 70 to 200nm. In order to investigate the polymer materials properties, we developed flexible PV cells following a conventional architecture. Indium tin oxide coated poly(ethyleneterephthalate) square substrates of about 1 cm^2 (PET/ITO; Aldrich, 45 Ω sq^{-1}, 100-120 nm sputtered ITO) have been used. PET/ITO was cleaned by ethanol and then treated by oxygen plasma (10 W, 1 min). Afterwards, PET/ITO was covered by a 40 nm film of poly(3,4-ethylenedioxythiophene):poly(styrenesulfonate) (PEDOT:PSS conductive grade; Aldrich) by spin-coating at 1000 rpm for 1 min, using a 0.65 wt.-% solution. PEDOT:PSS film was annealed at 100 °C for 1 h in dry nitrogen atmosphere. The back electrode consists in 5 nm LiF followed by 30 nm Al thin film masked to obtain an active area of approximately 0.4 cm^2. The PV data reported in this paper concerns measurements on at least three different devices.

Characterization methods

The nature of the electronic transitions on PDB has been investigated by means of time-dependent density functional theory (TDDFT) calculations using the B3LYP[22] functional and the cc-pvdz basis set with the Gaussian 03 package.[23] The morphology of the active layer has been inspected by dynamic scanning force microscopy (SFM) in air using a commercial instrument (Multimode Nanoscope IIIa, Digital Instruments, Santa Barbara, CA) equipped with a phase extender apparatus and a Q-box module.[24] Etched-silicon probes with a pyramidal-shape tip having a nominal curvature of 10 nm and a nominal internal angle of 358 were

used. During the scanning, the 125-mm-long cantilever, with a nominal spring constant in the range of 20-100 Nm,was oscillating at its resonance frequency (330 kHz). Height and phase images were collected by capturing 512 × 512 points with a scan rate below 1 line per second. During the imaging, temperature and humidity were about 293 K and 40%, respectively. UV-vis spectrum was performed directly on freshly prepared thin film BHJs with a thickness of about 100 nm, using a Beckman DU-640 spectrophotometer (Beckman Instruments, Fullerton, CA). Light beam induced current (LBIC) and light beam induced voltage (LBIV) measures were performed using an home-made experimental setup. The device was irradiated using a Halogen lamp (12 V, 100 W, ZEISS) with variable output power. A monochromatic beam at the wavelength of 590 nm (Jobin-Yvon monochromator, mod. H10 UV) was modulated by a chopper (Light Chopper Princeton Applied Research, mod. 197) at 1 KHz and focussed on the sample by a lens system (Nikon CF Plan Objective 100×/0.95 ∞/0 EPI). The signal produced by the device was detected using a lock-in amplifier (Stanford SR830). The complete device was electrically connected to ITO and aluminium electrodes, using conductive silver paste. The contacts were made on different areas of the device, isolated from each other by milling the ITO layer. This allows to prevent possible short circuits. The sample was moved respect to the optical beam by an *xy* micrometer equipped mechanical stage driven by two motors. A computer collected the data coming out from the lock-in amplifier, synchronized the *xy* movements and gave the spatially resolved voltage/current maps.

References

[1] G. Sang, Y. Zou, Y. Huang, G. Zhao, Y. Yang, Y. Li, *App. Phys. Lett.* **2009**, *94*, 193302; G. Sang, E. Zhou, Y. Huang, Y. Zou, G. Zhao, Y. Li, *J. Phys. Chem. C* **2009**, *113*, 5879-5885.
[2] C. R. McNeill, S. Westenhoff, C. Groves, R. H. Friend, N. C. Greenham, *J. Phys. Chem. C* **2007**, *111*, 19153-19160; S. Fabiano, B. Pignataro, *Phys. Chem. Chem. Phys.* **2010**, *12*, 14848-14860.
[3] R. A. L. Jones, L. J. Norton, E. J. Kramer, F. S. Bates, P. Wiltzius, *Phys. Rev. Lett.* **1991**, *66*, 1326.
[4] S. Y. Heriot, R. A. L. Jones, *Nat. Mater.* **2005**, *4*, 782-786.
[5] H. Kobayashi, N. Sato, Y. Ichikawa, M. Miyata, Y. Chujo, T. Matsuyama, *Synth. Met.* **2003**, *135-136*, 393-394; N. Sato, H. Ogawa, F. Matsumoto, Y. Chujo, T. Matsuyama, *Synth. Met.* **2005**, *154*, 113-116.
[6] M. Kinoshita, N. Fujii, T. Tsuzuki, Y. Shirota, *Synth. Met.* **2001**, *121*, 1571-1572.
[7] N. Matsumi, K. Naka, Y. Chujo, *J. Am. Chem. Soc.* **1998**, *120*, 5112-5113.
[8] A. Nagai, T. Murakami, Y. Nagata, K. Kokado, Y. Chujo, *Macromolecules* **2009**, *42*, 7217–7220.
[9] N. Matsumi, M. Miyata, Y. Chujo, *Macromolecules* **1999**, *32*, 4467-4469; A. Lorbach, M. Bolte, H. Li, H.-W. Lerner, M. C. Holthausen, F. Jakle, M. Wagner, *Angew. Chem. Int. Ed.* **2009**, *48*, 4584 –4588; C.-H. Zhao, A. Wakamiya, S. Yamaguchi, *Macromolecules* **2007**, *40*, 3898-3900; H. Li, A. Sundararaman, K. Venkatasubbaiah, F. Jäkle, *J. Am. Chem. Soc.* **2007**, *129*, 5792-5793.
[10] C. D. Entwistle, T. B. Marder, *Chem. Mater.* **2004**, *16*, 4574-4585.
[11] N. Matsumi, Y. Chujo, *Polymer Journal* **2008**, *40*, 77–89.
[12] S. Luebben, S. Sapp, *Material Matters* **2007**, *3*, 11.
[13] Y. Park, V. Choong, Y. Gao, B. R. Hsieh, C. W. Tang, *Appl. Phys. Lett.* **1996**, *68*, 2699-2701; N. Koch, J. Ghijsen, A. Elschner, R. L. Johnson, J. J. Pireaux, J. Schwartz, A. Kahn, *Appl. Phys. Lett.* **2003**, *82*, 70; M. Al-Ibrahim, H. Roth, U. Zhokhavets, G. Gobsch, S. Sensfuss, *Sol. Energy Mater. & Sol. Cells* **2005**, *85*, 13–20.
[14] C. J. Brabec, A. Cravino, D. Meissner, N. S. Sariciftci, T. Fromherz, M. T. Rispens, L. Sanchez, J. C. Hummelen, *Adv. Funct. Mater.* **2001**, *11*, 374-380.
[15] L. J. A. Koster, V. D. Mihailetchi, P. W. M. Blom, *Appl. Phys. Lett.* **2006**, *88*, 093511; C. J. Brabec, C. Winder, N. S. Sariciftci, J. C. Hummelen, A. Dhanabalan, P. A. v. Hal, R. A. J. Janssen, *Adv. Funct. Mater.* **2002**, *12*, 709-712.
[16] R. A. L. Jones, *Phys. World* **1995**, *8*, 47.

[17] G. D. Sharma, P. Suresh, P. Balaraju, S. K. Sharma, M. S. Roy, *Synth. Met.* **2008**, *158*, 400–410.
[18] J. A. Mikroyannidis, M. M. S. D. Sharma, P. Balraju, M. S. Roy, *J. Phys. Chem. C* **2009**, *113*, 7904–7912.
[19] L. J. A. Koster, V. D. Mihailetchi, H. Xie, P. W. M. Blom, *Appl. Phys. Lett.* **2005**, *87*, 203502; L. J. A. Koster, V. D. Mihailetchi, R. Ramaker, P. W. M. Blom, *Appl. Phys. Lett.* **2005**, *86*.
[20] Z. Tan, E. Zhou, X. Zhan, X. Wang, Y. Li, S. Barlow, S. R. Marder, *Appl. Phys. Lett.* **2008**, *93*, 073309.
[21] D. E. Markov, E. Amsterdam, P. W. M. Blom, A. B. Sieval, J. C. Hummelen, *Journal of Physical Chemistry A* **2005**, *109*, 5266-5274; O. V. Mikhnenko, F. Cordella, A. B. Sieval, J. C. Hummelen, P. W. M. Blom, M. A. Loi, *J. Phys. Chem. B* **2008**, *112*, 11601-11604.
[22] P. J. Stephens, F. J. Devlin, C. F. Chabalowski, M. J. Frisch, *J. Phys. Chem.* **1994**, *98*, 11623-11627.
[23] M. J. Frisch, G. W. Trucks, H. B. Schlegel, G. E. Scuseria, M. A. Robb, J. R. Cheeseman, J. J. A. Montgomery, T. Vreven, K. N. Kudin, J. C. Burant, J. M. Millam, S. S. Iyengar, J. Tomasi, V. Barone, B. Mennucci, M. Cossi, G. Scalmani, N. Rega, G. A. Petersson, H. Nakatsuji, M. Hada, M. Ehara, K. Toyota, R. Fukuda, J. Hasegawa, M. Ishida, T. Nakajima, Y. Honda, O. Kitao, H. Nakai, M. Klene, X. Li, J. E. Knox, H. P. Hratchian, J. B. Cross, V. Bakken, C. Adamo, J. Jaramillo, R. Gomperts, R. E. Stratmann, O. Yazyev, A. J. Austin, R. Cammi, C. Pomelli, J. W. Ochterski, P. Y. Ayala, K. Morokuma, G. A. Voth, P. Salvador, J. J. Dannenberg, V. G. Zakrzewski, S. Dapprich, A. D. Daniels, M. C. Strain, O. Farkas, D. K. Malick, A. D. Rabuck, K. Raghavachari, J. B. Foresman, J. V. Ortiz, Q. Cui, A. G. Baboul, S. Clifford, J. Cioslowski, B. B. Stefanov, G. Liu, A. Liashenko, P. Piskorz, I. Komaromi, R. L. Martin, D. J. Fox, T. Keith, M. A. AlLaham, C. Y. Peng, A. Nanayakkara, M. Challacombe, P. M. W. Gill, B. Johnson, W. Chen, M. W. Wong, C. Gonzalez, J. A. Pople, *Gaussian 03, Revision D.02*, Gaussian Inc., Wallingford, CT, **2004**.
[24] B. Pignataro, L. F. Chi, S. Gao, B. Anczykowski, C. M. Niemeyer, M. Adler, D. Blohm, H. Fuchs, *Appl. Phys. A* **2002**, *74*, 447-452; B. Pignataro, *J. Mater. Chem.* **2009**, *19*, 3338.

Appendix A

2.1 SFM measurements

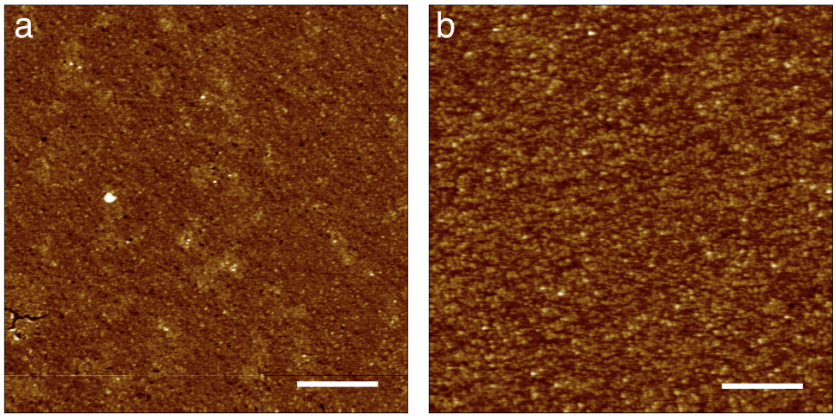

Figure S1. Typical topography images measured by SFM of a Langmuir-Schäfer P(NDI2OD-T2) monolayer on HMDS-modified silicon oxide before (a) and after (b) annealing at 150 °C in vacuum overnight. The thermal treatment removes the residual water and reduces the nanohole defects. The scale bars are 1 μm.

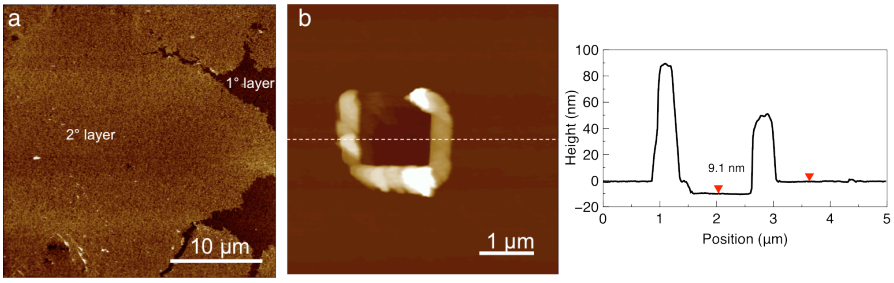

Figure S2. Typical topography images measured by SFM of a Langmuir-Schäfer P(NDI2OD-T2) bilayer on HMDS-modified silicon oxide after thermal annealing at 150 °C overnight (a). A long-range order is still visible in the second layer. (b) SFM square scratch in a trilayer film and, on the right, the section analysis along the dotted line showing a total thickness of 9.1 nm. Since SFM measures about 3 nm for the monolayer, this finding shows that the edge-on conformation is maintained in the successive LS layers.

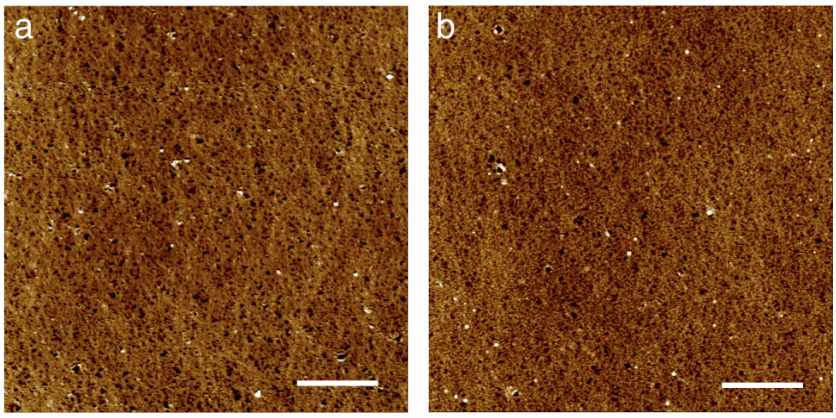

Figure S3. Typical topography images measured by SFM of a Langmuir-Schäfer P(NDI2OD-T2) monolayer on HMDS-modified glass substrate before (a) and after (b) annealing at 150 °C in vacuum overnight. The scale bars are 1 μm.

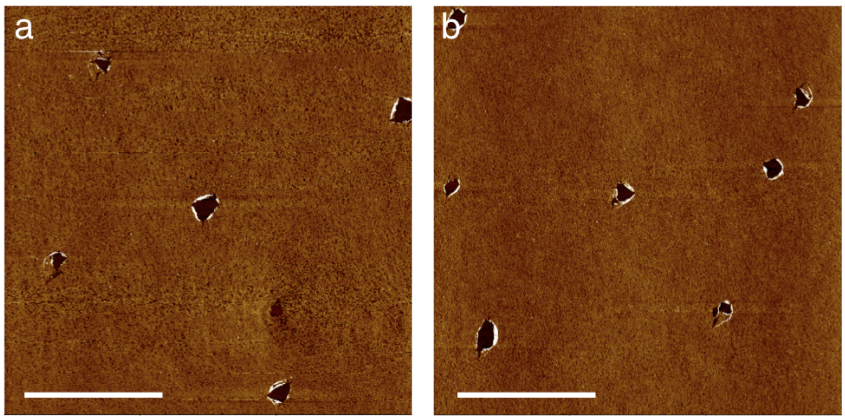

Figure S4. Typical topography images measured by SFM of a Langmuir-Schäfer P(NDI2OD-T2) monolayer on HMDS-modified glass substrate before (a) and after (b) annealing at 150 °C in vacuum overnight showing several void defects. Interestingly, such defects 1-2 μm in diameter are squared and persist after the thermal annealing as an indication of a crystalline character of the monolayer. The scale bars are 10 μm.

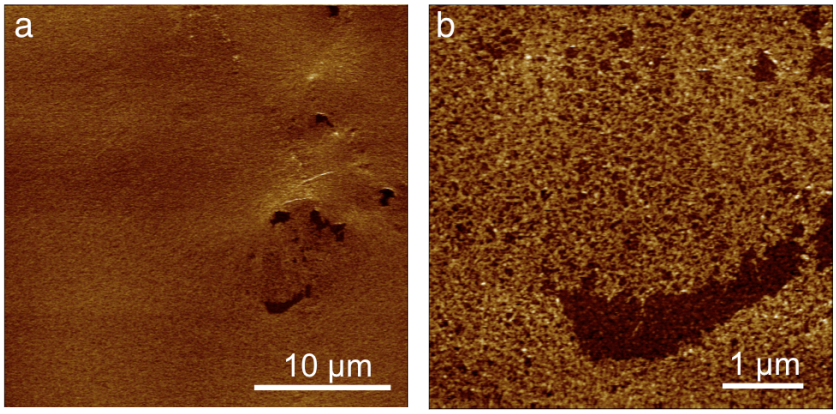

Figure S5. Typical topography image (30 × 30 µm²) measured by SFM for Langmuir-Schäfer P(NDI2OD-T2) monolayer on Au surface (a). A magnification of the defective region is reported in (b). The step height is still consistent with an edge-on orientation of the polymer backbone chains.

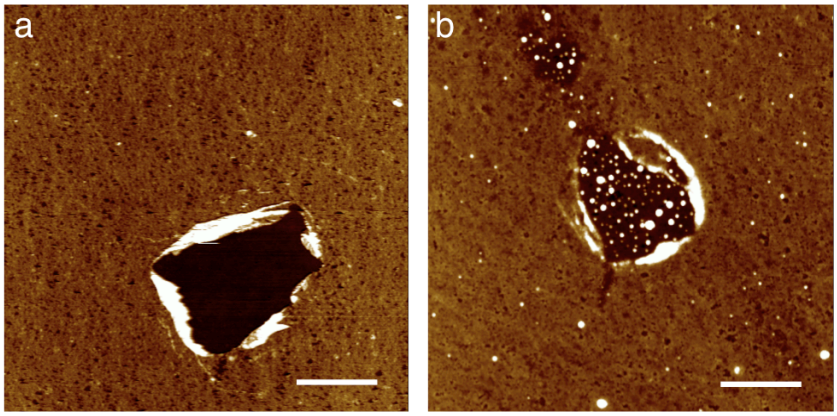

Figure S6. SFM topography images of Langmuir-Schäfer P(NDI2OD-T2) monolayers on HMDS-modified glass before (a) and after (b) selectively removing the PMMA dielectric layer by immersing the sample in ethyl acetate for 10 min. Since ethyl acetate is an orthogonal solvent for P(NDI2OD-T2), the semiconducting monolayer is not affected by the PMMA spin-coating on top of it. Indeed, such a treatment maintains the void defects quite unaltered in size and shape. The globular agglomerates in (b) are likely due to residual PMMA. The scale bars are 1 µm.

2.2 NEXAFS measurements

Near-edge X-ray absorption fine structure spectroscopy (NEXAFS) experiments were carried out at the NIST/DOW soft X-ray materials characterization facility at beamline U7A at the National Synchrotron Light Source at Brookhaven National Laboratories. Partial electron yield (PEY) NEXAFS spectra were acquired at the carbon K-edge at three different X-ray incident angles of 75° (near normal), 55° (magic) and 35° (grazing) on LS monolayers deposited and thermally annealed on HMDS-modified glass, shown in Figure 2.4a of Chapter 2. The PEY detector is sensitive to the top 2 nm of the film. By subtracting the spectrum at 35° from that at 75°, we can identify the peak positions and quantify the peak widths associated with the individual resonances. Peak positions associated with the 1s to π^* transitions are identified at 284.2 eV, 284.9 eV, 285.8 eV, 287.3 eV, 288.1 eV and 290.8 eV; peak positions associated with the 1s to σ^* transitions are identified at 296.0 eV, 298.2 eV and 302.0 eV. The peaks associated with the 1s to π^* transitions grow while the peaks associated with the 1s to σ^* transitions decrease in intensity with increasing X-ray incident angles. This observation indicates that the molecules in the LS monolayer are preferentially oriented edge on. The extent of preferential orientation can be further quantified by extracting the integrated intensities of the first 1s to π^* transition at 284.2 eV. The inset to Figure 2.4a displays the extracted integrated intensities of this transition as a function of X-ray incident angle. The positive slope is consistent with the growth of this peak with incident angle and indicates that the molecules are preferentially oriented edge on. To quantify, we have identified the dichroic ratio (DR),

$$DR = \frac{I(90°) - I(0°)}{I(90°) + I(0°)}$$

where I is the integrated intensity of the 1s to π^* transition at normal and glancing incidence (90^o and 0^o, respectively). These intensities are extrapolated from the experimentally obtained integrated intensities, represented as dots in the inset to Figure 2.4a. From this analysis, the LS monolayer that is deposited and thermally annealed on HMDS-modified glass exhibits a DR = 0.23. By definition, when DR > 0, the molecules are preferentially oriented upright. When DR < 0, on the other hand, the molecules are preferentially oriented face on. When DR = 0, the molecules are randomly oriented. Here, a DR of 0.23 indicates that the molecules in the LS monolayer are preferentially oriented edge on. This value of DR is comparable to what had previously been observed in P3HT thin films.

2.3 XPS measurements

XPS survey spectra (not shown) of both spin coated and LS films show the C, O and Au signals. The sulphur and nitrogen signals are not clearly visible in the survey spectra, but high statistics acquisition in the N1s and S2p binding energy regions reveal the presence of the corresponding signals. Figure S7 reports, in comparison, the XPS C1s core level spectra of spin coated and LS films that are very similar to each other, with the exception of the spin-coated film that is slightly shifted towards higher binding energy (see also Table S1). The observed features in both spectra are compatible with the polymer chemical structure. In particular the main component is assigned to side chains and to C-S of the thiophene rings and the bump at higher binding energy side is assigned to (C*=0)-N groups.

Table S1. XPS Binding energies (eV) of S2$p_{1/2}$, S2$p_{3/2}$, C1s, O1s and N1s peaks of spin coated and LS deposited films.

	S2p		**C1s (main component)**	**O1s**	**N1s**
	1/2	3/2			
Spin coated	165.67	164.30	285.16	531.94	400.73
LS	165.22	164.09	284.81	531.63	400.33

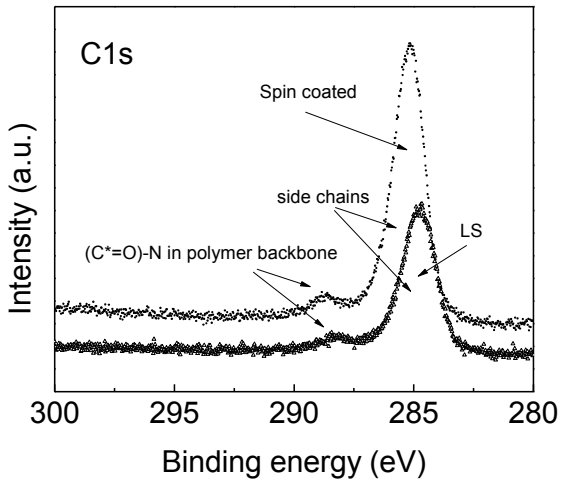

Figure S7. XPS C1s spectra of spin coated and LS films.

2.4 FETs characterization

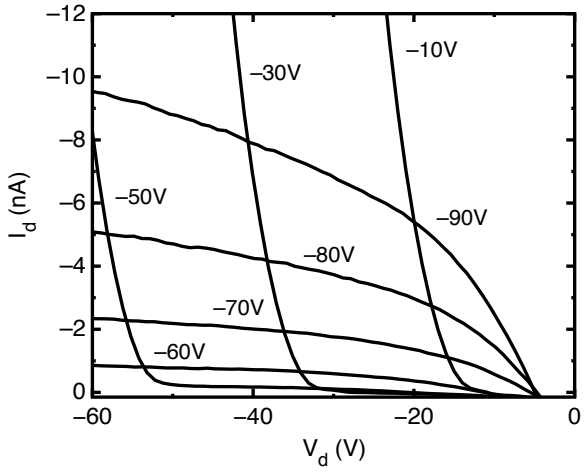

Figure S8. The output characteristics of the spin-coated P(NDI2OD-T2) transistor demonstrate ambipolar operation. The current shows a pronounced increase at V_g lower than –50V, due to the accumulation of both holes and electrons in the transistor channel forming a p-n junction.

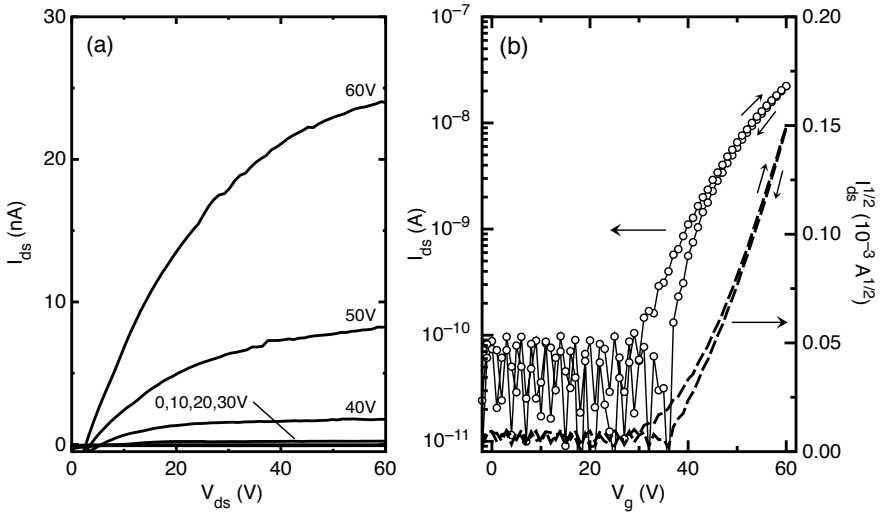

Figure S9. (a) Output characteristics for a monolayer P(NDI2OD-T2) FET with channel length of 50 μm and channel width of 500 μm after 5-weeks storage in air. (b) Saturated transfer characteristics for the corresponding FET, using a drain bias of 60 V.

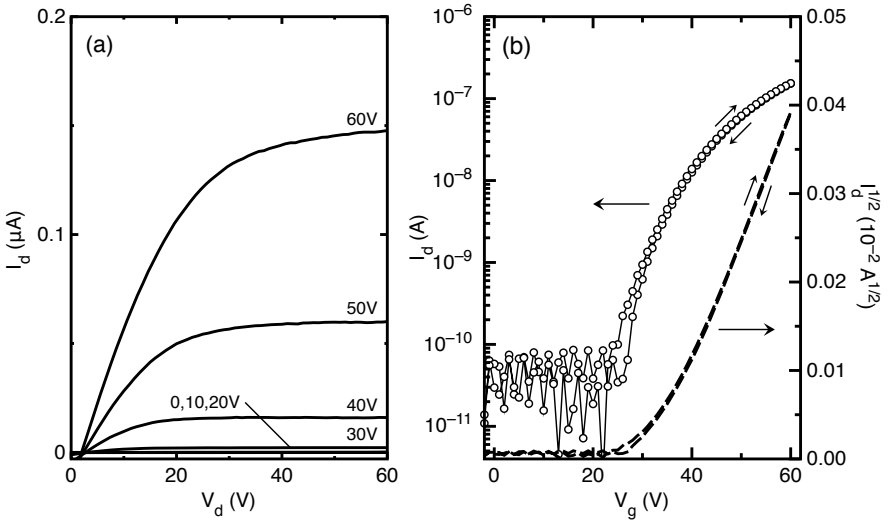

Figure S10. (a) Output characteristics for a 2-layer P(NDI2OD-T2) FET with channel length of 50 μm and channel width of 500 μm. (b) Saturated transfer characteristics for the corresponding FET, using a drain bias of 60 V.

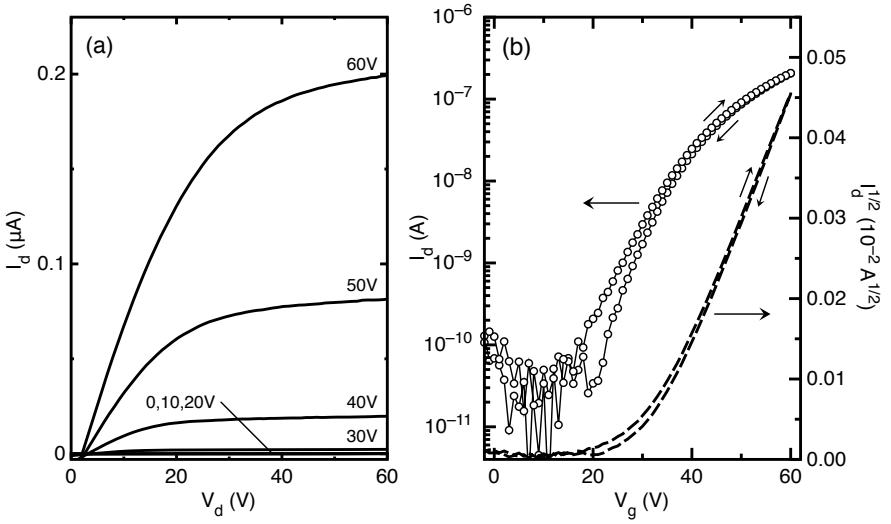

Figure S11. (a) Output characteristics for a 3-layer P(NDI2OD-T2) FET with channel length of 50 μm and channel width of 500 μm. (b) Saturated transfer characteristics for the corresponding FET, using a drain bias of 60 V.

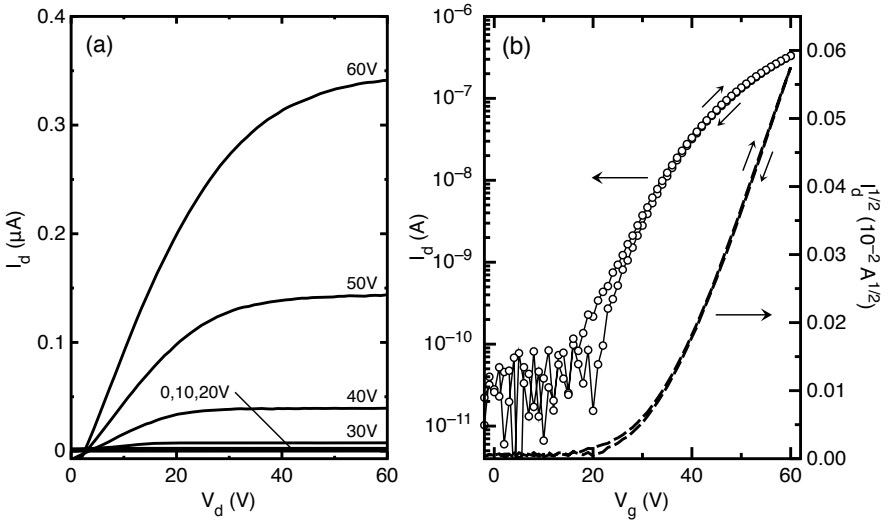

Figure S12. (a) Output characteristics for a 6-layer P(NDI2OD-T2) FET with channel length of 50 μm and channel width of 500 μm. (b) Saturated transfer characteristics for the corresponding FET, using a drain bias of 60 V.

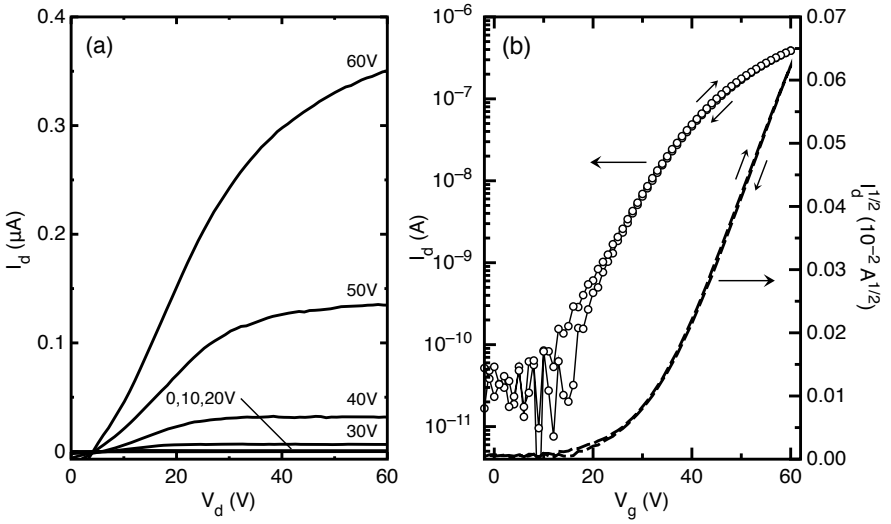

Figure S13. (a) Output characteristics for a 15-layer P(NDI2OD-T2) FET with channel length of 50 μm and channel width of 500 μm. (b) Saturated transfer characteristics for the corresponding FET, using a drain bias of 60 V.

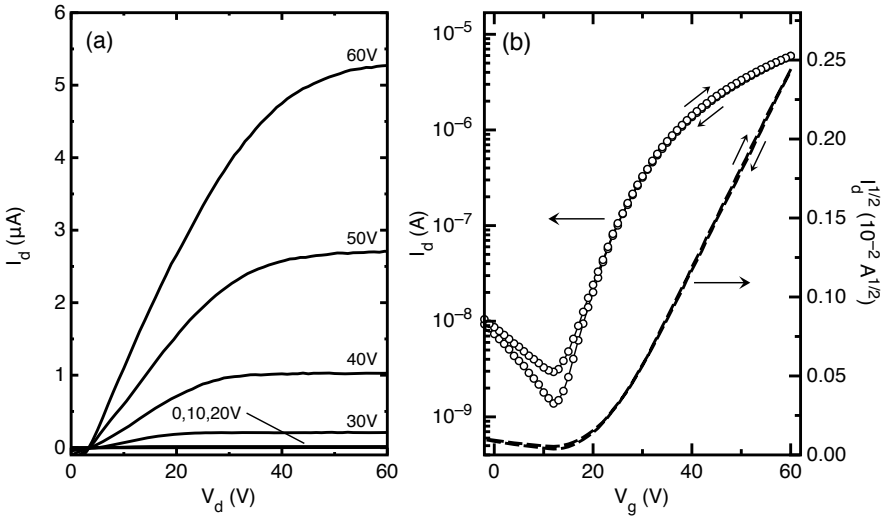

Figure S14. (a) Output characteristics for a spin-coated P(NDI2OD-T2) FET with channel length of 50 μm and channel width of 500 μm. (b) Saturated transfer characteristics for the corresponding FET, using a drain bias of 60 V.

Appendix B

2.1 SFM measurements

The SFM height (h) profiles were analyzed from the power spectral density (PSD) as a function of the spatial frequency, f. The PSD is calculated by using eq. 1 on images with scan length (L) fixed at 5 μm, long the fast scan direction x.

$$\mathrm{PSD}(f) = \frac{1}{L}\left|\int_0^L dx h(x) e^{i2\pi fx}\right|^2 \qquad (1)$$

The self-affine structure exhibits power-law decay $\mathrm{PSD}(f) = K_0 f^{-\gamma}$ in a finite range of f. The roughness-scaling exponent α is related to γ by $\alpha = (\gamma - d)/2$, where the scan dimension d is equal to 1.[1] The calculated PSD for as-cast and annealed thin films on HMDS-modified substrates is presented in Figure 3.2 of Chapter 3.

2.2 NEXAFS measurements

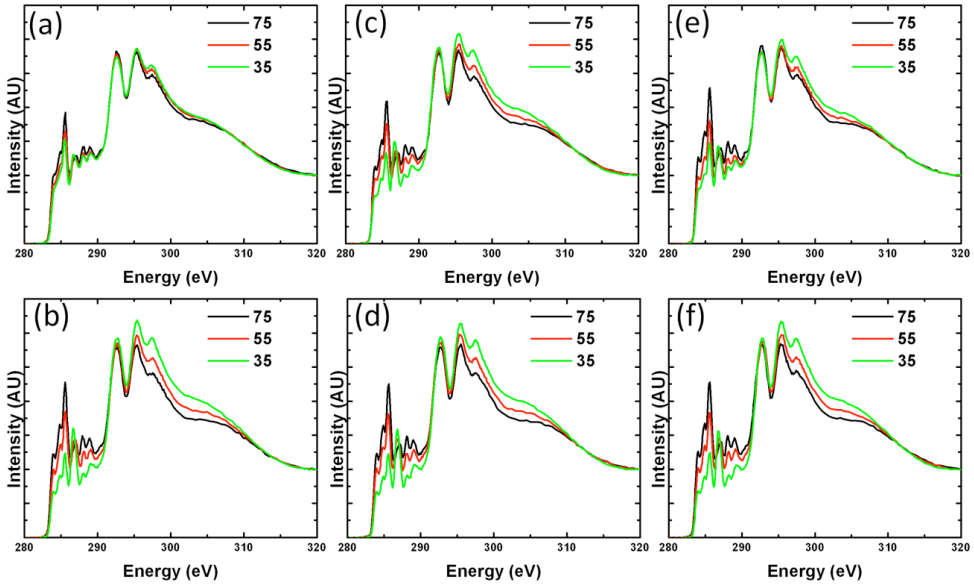

Figure S1. Pre- and post-edge normalized NEXAFS spectra acquired at the carbon edge at three different X-ray incident angles, 75°, 55° and 35° for as-cast (a) and thermally annealed (b) PDIF-CN2 on bare gold; as-cast (c) and thermally annealed (d) PDIF-CN2 on HMDS modified-silicon oxide; as-cast (e) and thermally annealed (f) PDIF-CN2 on thiol-modified gold.

2.3 Surface energy measurements

The measured contact angle values θ for water and diiodomethane (DI) were fitted to calculate the polar (γ^p) and dispersive (γ^d) components of the total surface energy γ^{tot}, according to the Young-Dupre equation:

$$1+\cos\theta = \frac{2\left(\gamma_s^d\right)^{1/2}\left(\gamma_{lv}^d\right)^{1/2}}{\gamma_{lv}} + \frac{2\left(\gamma_s^p\right)^{1/2}\left(\gamma_{lv}^p\right)^{1/2}}{\gamma_{lv}}$$

Table S1. Contact angles and surface energy values for PDIF-CN_2 films on different surfaces.

	θ_{water} (°)	θ_{DI} (°)	γ^p (mJ cm^{-2})	γ^d (mJ cm^{-2})	γ^{tot} (mJ cm^{-2})
On HMDS-SiO_2; as-cast	102.7(±0.6)	82.1(±0.9)	1.8	16.5	18.3
On HMDS-SiO_2; annealed	109.3(±0.5)	88.9(±0.8)	1.1	13.2	14.3
On Au; as-cast	103.6(±0.5)	80.6(±1.4)	1.4	17.2	18.6
On Au; annealed	109.3(±0.6)	88.1(±1.2)	1.0	13.6	14.6
On thiol-Au; as-cast	103.6(±0.3)	80.8(±0.8)	1.4	17.1	18.5
On thiol-Au; annealed	109.7(±0.6)	88.1(±0.5)	0.9	13.6	14.5

Table S2. Contact angles and surface energy values for the different surface treatments.

	θ_{water} (°)	θ_{DI} (°)	γ^p (mJ m^{-2})	γ^d (mJ m^{-2})	γ^{tot} (mJ m^{-2})
HMDS-SiO_2	79.3(±0.8)	42.9(±1.1)	4.0	38.1	42.1
Au	85.8(±0.7)	23.4(±1.3)	1.0	46.7	47.7
Thiol-Au	90.4(±0.8)	41.2(±0.8)	0.9	39.0	39.9

References

[1] Biscarini, F.; Samorì, P.; Greco, O.; Zamboni, R. *Phys. Rev. Lett.* **1997**, *78*, 2389.

Summary

Organic semiconductors have been presented as very promising materials for (opto) electronic devices due to their low-cost, mechanical flexibility and lower power consumption. However, the applications of these novel materials as active components in commercially available all-plastic electronics are not immediate yet, due to the relatively low performances. In order to improve such device outputs, efforts have to be spent to optimize the organic thin film morphology and device structure. Therefore, a full understanding of the self-assembly/self-organization phenomena behind the morphology of such materials as well as of the devices physics is needed to improve their charge transport properties, and hence to have practical applications.

Developing semiconducting materials that are air-stable, soluble and with excellent transport properties is the key requisite for a next generation of electronic devices. This is because organic semiconductors exhibit large chemical versatility allowing the incorporation of both self-assembly and electronic active functions. Thus, one of the greatest challenges in designing new materials is the dependence of the charge transport properties on the molecular packing. In this context, engineering solid supported 2D and 3D molecular and supramolecular superstructures is of particular interest. Indeed, for instance, processing conjugated organic semiconductors into layers of well-defined thickness is stimulating for studying the correlation between electrical and morphological properties of promising organic materials at nanoscale. On this respect, the self-assembly approaches as well as the use of high-resolution patterning methods like for example Langmuir-Blodgett/Langmuir-Schaefer techniques are smart ways for shrinking the dimension of the active layer. In spite of the very low carrier mobility generally observed for conjugated polymers in the first few layers, in *Chapter 2* we stated that the minimum thickness of a polymeric semiconductor to act as channel of a field effect transistor is just one layer. This result opens exciting perspectives for the realization of bottom-up electronic devices as well as for new fundamental studies.

A general correlation between molecular orientation and device performances has been highlighted in *Chapter 3*, showing the exceptional supramolecular order of solution-processed semiconducting molecules. The presence in fact of self-assembling moieties in the semiconductor represents a driving force for the spontaneous association of the molecules under energy minimization conditions (e.g. thermal stimuli) into stable, structurally well-defined supramolecular architectures.

Studying the charge transport and injection properties reveals the self-assembly dynamics behind the peculiar morphology that is responsible for the relatively high charge carrier mobility, and underlines some fundamental characteristics that a solution processable small molecule should have in order to perform well in a field-effect transistor. Indeed, the engineering processes of nanostructures at the surfaces can not prescind from a chemical engineering at the molecular level and it should take into account critical parameters like the lateral interactions of molecules and their coupling to the surface in order to guide the assembly towards desired structures.

On the other hand, exploiting out-of-equilibrium dynamic conditions to get 3D ordered super-structures on nanoscale is of fundamental interest for devices where the charge transport is perpendicular to the plane. In this respect, in *Chapter 4* we described the effect of layer morphology on the photoelectric properties of a polymeric blend, varying the self-organization phenomena from a vertical phase segregation to a lateral phase separation. The results suggest high dissociation efficiency for the bounded electron-hole pairs and balanced electron and hole mobility along the thin films, revealing new insights into the main factors limiting the efficiency of all-polymer solar cells. Suppressing the strong tendency of polymers to preaggregate in specific organic solvents would represent an important step forward to improve the intermixing of the donor and acceptor component, thereby allowing efficient harvesting of photogenerated excitons at the donor–acceptor heterojunction. In addition, the final polymeric blend morphology may be modulated by polymer composition ratio optimization to give a higher percentage of domains comparable with the exciton diffusion length, as discussed in *Chapter 5*.

Sommario

I semiconduttori organici sono stati proposti come materiali assai promettenti per la realizzazone di dispositivi (opto)elettronici, grazie al loro basso costo, l'elevata flessibilità meccanica e il limitato consumo energetico. Tuttavia, la commercializzazione di dispositivi elettronici su plastica che utilizzino tali nuovi materiali come componenti attivi disponibili non è ancora immediata, per via delle efficienze relativamente basse. Al fine di migliorare le prestazioni di tali dispositivi, ulteriori sforzi devono essere rivolti all'ottimizzazione della morfologia dei film sottili organici e della struttura stessa dei dispositivi. Dunque, una piena conoscenza dei fenomeni di auto-assemblamento/auto-organizzazione alla base della morfologia di tali materiali, così come della fisica dei dispositivi, è necessaria per migliorare le proprietà di trasporto di carica e consentirne una pratica applicazione.

Lo sviluppo di semiconduttori organici che siano stabli in aria, solubili e con eccellenti proprietà di trasporto è un requisito chiave per una futura generazione di dispositivi elettronici. Ciò perché i semiconduttori organici mostrano una ampia versatilità chimica che consente di incorporare, all'interno di uno stesso sistema, funzioni di auto-assemblamento e di attività elettrica. Dunque, la principale sfida nel disegnare nuovi materiali è la dipendenza delle proprietà di trasporto di carica dall'impaccamento molecolare. In questo contesto, ingegnerizzare superstrutture molecolari e supramolecolari su supporto solido in 2D e 3D è di particolare interesse. Infatti ad esempio, processare semiconduttori organici coniugati in strati di spessore ben definito è di stimolo per studiare le correlazioni tra proprietà elettriche e morfologiche di tali sistemi su nanoscala. A questo proposito, approcci di auto-assemblamento così come l'uso di metodi di fabbricazione ad alta risoluzione quali ad esempio Langmuir-Blodgett/Langmuir-Schaefer techniques, sono una via intelligente per ridurre la dimensione dello strato attivo. Sebbene una bassa mobilità dei trasportatori di carica sia generalmente osservata per polimeri coniugati, nel *Capitolo 2* dimostriamo che lo spessore minimo di un polimero semiconduttore perché questo si comporti come canale attivo di un transistore ad effetto di campo è solo uno strato. Tale risultato apre interessanti prospettive per la realizzazione di dispositivi elettronici "*bottom-up*" così come per nuovi studi fondamentali.

Una correlazione generale tra orientazione molecolare e performance dei dispositivi è stata evidenziata nel *Capitolo 3*, dove si riporta l'eccezionale ordine supramolecolare di molecole semiconduttori processate da soluzione. La presenza nei

semiconduttori di unità auto-assemblanti rappresenta nei fatti una forza guida per la spontanea associazione delle molecole in condizioni di minimo di energia (ad esempio in seguito a stimoli termici), in architetture supramolecolari stabili e strutturalmente ben definite. Lo studio delle proprietà di iniezione e trasporto di carica rivela le dinamiche di auto-assemplamento alla base della morfologia peculiare responsabile dell'elevata mobilità dei trasportatori di carica, e sottolinea alcune delle caratteristiche fondamentali che una molecola processabile da soluzione deve avere al fine di funzionare bene in transistori ad effetto di campo. Infatti i processi di ingegnerizzazione di nanostrutture su superfici non può prescindere da una ingegnerizzazione chimica a livello molecolare e dovrebbe tenere conto di parametri critici come le interazioni laterali delle molecole e il loro accoppiamento su superficie, al fine di guidare l'assemblamento verso le strutture desiderate.

D'altro canto, sfruttare condizioni dinamiche fuori dall'equilibrio per ottenere superstrutture 3D ordinate su nanoscala è di fondamentale interesse per dispositivi dove il trasporto di carica è perpendicolare al piano. A questo proposito, nel *Capitolo 4* abbiamo descritto gli effetti della morfologia sulle proprietà fotoelettriche di una miscela polimerica, variando i fenomeni di auto-organizzazione da una segregazione di fase verticale ad una separazione di fase laterale. I risultati suggeriscono un'elevata efficienza di dissociazione delle coppie elettrone-lacuna e una bilanciata mobilità per gli elettroni e per le lacune all'interno del film sottile, rivelando nuovi particolari sui principali fattori che limitano le efficienze delle celle solari polimeriche. Sopprimendo la forte tendenza dei polimeri a preaggregarsi in specifici solventi organici rappresenterebbe un importante passo avanti al fine di migliorare il miscelamento della componente donatore e accettore, consentendo dunque una efficiente raccolta degli eccittoni fotogenerati all'eterogiunzione donatore-accettore. Per di più, la morfologia finale della miscela polimerica potrebbe essere modulata mediante un'ottimizzazione dei rapporti di composizione per dare una più alta percentuale di domini comparabili con la lunghezza di diffusione eccitonica, come discusso nel *Capitolo 5*.

List of publications

Organoboron Polymers for Photovoltaic Bulk Heterojunctions
S. Cataldo, **S. Fabiano**, F. Ferrante, F. Previti, S. Patanè, B. Pignataro
Macromolecular Rapid Communications 2010, 31, 1281-1286

Engineering 3D ordered molecular thin films by nanoscale control
S. Fabiano, B. Pignataro
Physical Chemistry Chemical Physics 2010, 12, 14848-14860

Role of Photoactive Layer Morphology in High Fill Factor All-Polymer Bulk Heterojunction Solar Cells
S. Fabiano, Z. Chen, S. Vahedi, A. Facchetti, B. Pignataro, M. A. Loi
Journal of Materials Chemistry 2011, 21, 5891-5896

Supramolecular Order of Solution-Processed Perylenediimide Thin Films: High-Performance Small-Channel n-Type Organic Transistors
S. Fabiano, H. Wang, C. Piliego, C. Jaye, D. A. Fischer, Z. Chen, B. Pignataro, A. Facchetti, Y-L. Loo, M. A. Loi
Advanced Functional Materials 2011, 21, 4479-4486

From Monolayer to Multilayer N-Channel Polymeric Field-Effect Transistors with Precise Conformational Order
S. Fabiano, C. Musumeci, Z. Chen, A. Scandurra, H. Wang, L.-Y- Loo, A. Facchetti, B. Pignataro
Advanced Materials 2012, 24, 951-956

Selecting speed-dependent pathways for a programmable nanoscale texture at wet interfaces
S. Fabiano, B. Pignataro
Chemical Society Reviews (Tutorial review invited by the editor), in preparation

Acknowledgments

The work described in this thesis could never be realized without the assistance and support of others to whom I am addressing my gratitude here.

First of all I am grateful to Prof. Bruno Pignataro for the outstanding supervision during these three years of work. Thank you for your full support, patience and for trusting in me and in my ideas. I would like to thank you for providing me with a great opportunity, to work on such a challenging and extremely interesting field. I have also to acknowledge all the members of the group at the University of Palermo, in particular Sebastiano Cataldo who has shown me several important experimental tricks of polymer science, Viviana Figà and Camillo Sartorio: sorry for the mugs!

I would like to thank Consorzio Catania Ricerche for giving me the possibility to work at SuperLab. Very special thanks go here to my colleagues with whom I shared the daily working life. I am very grateful to Chiara Musumeci, a great scientist and also an enjoyable person: thank you for introducing me to the use of SFM. Many thanks to Alessandro Luzio for the constructive inspiring discussions and suggestions: really impressive your ability to draw mythological animals. I cannot forget Giuseppe Arrabito, a great and passionate colleague. I am sure your passion for science will take you far. Sincere thanks are also extended to Dr Antonio Scandurra for kindly supplied photoelectron spectroscopy measurements and Giuseppe Indelli for providing an invaluable technical support. The Italian MiUR (PLAST_ICs and FIRB-Futuro in Ricerca 2008) is acknowledged for financial support.

I really have to thank Prof. Maria Antonietta Loi for giving me the possibility to join her wonderful group at the University of Groningen as visiting PhD and providing me with an outstanding supervision during my stay there. Thank you for your full support, for encouraging and pushing me. I have been glad for such an opportunity. I am also grateful to all the POE/MEPOS group members and the friends who have enriched my pleasant stay in Groningen: Prof. Paul Blom, Prof. Dago de Leeuw, Jan, Frans, Arjen, Renate, Herman, Alex, Paul, Auke, Date, Gert-Jan, Fatemeh, Kamal, Kriszti, Anne-Marije, Ilias, Irina, Johan, Martijn Kuike, Francesco, Milo, Widi, Davide, Claudia. My special thanks to Marianna, Dorota, Filippo and Jia, who have made this experience awesome. *Dank je wel!*

I want to thank Prof. Salvatore Patanè and his group at the University of Messina for their contribution in our research collaboration on organoboron polymers. ST-Microelectronics and in particular, Dr Antonio La Mantia, Dr Vincenzo Vinciguerra

and Dr Luigi Occhipinti are also acknowledged.

I owe much to Prof. Antonio Facchetti from Northwestern University for his everlasting provision of high quality synthetic materials, superb spirit of collaboration and for being always ready to discuss results. Acknowledgments go also to Prof. Lynn Loo and He Wang at Princeton University for NEXAFS measurements and for the useful discussion of the results.

Thanks go of course to all my friends in Italy and in the Netherlands for the great time together. A friend in need is a friend indeed.

I would like to specially thank my dearest *mamma*, *papà* and *Silvia*, for their patience and continuous support all the time. Without your efforts I would not have reached the conclusion of my PhD. *Grazie!*

Finally, I want to thank the most special person in my life: Chiara. You are my motivation when times are tough and you have always been there to help me during all the ups and downs. I feel confident for all the future things to come with you by my side. Thank you for being who you are.

Simone
February, 2012